NASA Contractor Report 2975

Balancing Techniques for High-Speed Flexible Rotors

A. J. Smalley, J. M. Tessarzik,
and R. A. Rio

CONTRACT NAS3-18520
APRIL 1978

NASA

NASA Contractor Report 2975

Balancing Techniques for High-Speed Flexible Rotors

A. J. Smalley, J. M. Tessarzik,
and R. A. Rio
Mechanical Technology, Inc.
Latham, New York

Prepared for
Lewis Research Center
under Contract NAS3-18520

National Aeronautics
and Space Administration

**Scientific and Technical
Information Office**

1978

TABLE OF CONTENTS

LIST OF ILLUSTRATIONS

LIST OF TABLES

LIST OF SYMBOLS

B	damping coefficient (NS/m)
D	diameter
E	Young's modulus (N/m^2)
F	distance across flats of asymmetric rotor section
F^+, F^-	point frequencies at which amplitude = $1/\sqrt{2}$ times peak amplitude
f_n	resonant frequency
I	section transverse second moment of area
K	stiffness (N/m)
L_1, L_2	lengths of flattened shaft sections
ℓ	shaft length
M	total mass of shaft
Max.	maximum
m	preload ratio; number of planes
N_n	modal norm
n	number of modes
R_n	probe configuration measure of "quality"
Q_n	magnification factor
S	complex root
$\bar{S}$	weighted sum of normalized correction weights
S_n	normalized sum of correction weights to correct unit unbalance
U_n, u_n	unit modal unbalance
W_{pn}	correction weight set values for mode n
Z_m	axial location of probes
Z_p	axial location of planes
z	axial location
δ	log decrement
δ_n	log decrement for n^{th} mode
ζ	normalized plane locations
λ	real part of eigenvalue
λ_n	growth exponent
μ	mass per unit length
ξ_n	adjoint function
Ω	spin frequency
ω	damped natural frequency

LIST OF SYMBOLS AND ABBREVIATIONS FOR APPENDIX B

NOMENCLATURE

A	cross-sectional area of shaft
$\underline{\underline{B}}$	bearing translational damping matrix
B_{xx}, B_{xy}	direct and cross-coupling translation damping coefficient
D_{xx}, D_{xy}	angular direct and cross-coupling damping coefficient
E	Young's modulus, psi
f^+, f^-	frequencies (Hz) of the "half-power points" for a critical speed
f_n	resonant frequency, Hz
$(I\xi)_n, (I\eta)_n$	transverse moments of inertia about ξ, η axes
J_{tn}, J_{pn}	transverse and polar moments of inertia at a station
$\underline{\underline{K}}$	bearing translational stiffness matrix
ℓ_n	distance between station n and station n+1
M_n	concentrated mass at station n
M_{xn}, M_{yn}	bending moment at lower numbered side of station
M'_{xn}, M'_{yn}	bending moment at higher number side of station
N	number of stations
S	complex eigenvalue
$\underline{\underline{T}}$	rotor matrix relating forces and moments at one end to displacement and slope at the other end
t	time
V_{xn}, V_{yn}	shear forces at lower numbered side of station
V'_{xn}, V'_{yn}	shear forces at higher numbered side of station
x_n	displacement in x-direction at station n
y_n	displacement in y direction at station n
α	angle of rotor deflection in ξ plane; also shape factor for shear deformation
β	angle of rotor deflection in η plane
Δ	determinant of rotor matrix

Δp	determinant of rotor matrix with elements of p^{th} column replaced by their derivatives with respect to S
δ	log decrement
Θ_M	angle of rotor deflection in fixed frame
λ	real part of eigenvalue
ξ^*	amplitude of displacement in ξ direction
ξ, η	rotating coordinate direction
ϕ_n	angle of rotor deflection in fixed frame
Ω	rotational angular velocity
ω	imaginary part of eigenvalue expressed in nonrotating frame
ω'	imaginary part of eigenvalue expressed relative to rotating coordinate frame

SUMMARY

Identification of ideal conditions for balancing and evaluations of non-ideal conditions are treated in this report. Work was performed in the areas of balancing a shaft with flexural asymmetry, balancing a shaft with resonant supports for the displacement sensors, and establishing guidelines and criteria for location of balance planes and sensors.

A three-mass test rotor with a flattened shaft was designed to evaluate the feasibility and problems of balancing a rotor with flexural asymmetry. Two problems encountered with the test shaft were: a gravity excited critical spee occurring at half the first bending critical speed; and an unnegotiable instability encountered above the lower of two bending critical speeds. These were overcome by increasing bearing damping and redistributing rotor mass in the first case and by redesigning the shaft to reduce asymmetry in the second case.

Flexible probe holders were designed. These were attached to the bearing housings and tuned so that, in the region of the first bending critical speed of the shaft, a probe support resonance occurred. Balancing, based directly on signals from the resonant probes, was successfully performed for this non-ideal condition. Various trial weight locations and tracking filter bandwidths were used during the final balancing experiments, and successful balancing was accomplished in all cases.

An analysis was developed and used to quantify the effectiveness of a particular balance plane configuration in terms of a penalty function. This penalty function is based on the amount of weight to be added or removed to correct for a unit unbalance distribution for each mode of vibration considered. Also, a function, which can be used to measure the sensitivity of a particular arrangement of displacement sensors, is suggested. These functions provide guidance to the designer who is faced with the problem of selecting locations for planes and sensors for multiplane balancing. The use of these functions to measure the quality of plane and probe locations is described and related to the overall process of designing for multiplane balancing.

INTRODUCTION

Flexible rotor balancing by the multiplane-multispeed method is now proven technology. Following the analytical formalization of the method, exacting and successful laboratory tests of the method have been performed (1,2,3), and a number of successful solutions to difficult machinery vibrations problems have been achieved by field application of the method (13,14). Furthermore, a number of engineering studies have shown, analytically, the potential value of the method for routine balancing in a wide range of high-speed machinery applications.

The desirability of using "optimum" or "near optimum" locations for balance planes and sensors has been shown by these demonstrations and studies. However, in most machines, constraints exist which inhibit the use of the optimum locations, and a means to evaluate "non-ideal" locations is clearly necessary. At the same time, other "non-ideal" aspects of "real" balancing requirements must be recognized.

This report addresses both the identification of ideal conditions for balancing and the evaluation of non-ideal conditions. Work in three areas is presented:

- Balancing of a shaft with flexural asymmetry.
- Balancing a shaft under non-ideal conditions which included resonant probe holders, extremes in bandwidth filters, and a reduced number of trial weight placements for determining influence coefficients.
- Guidelines and criteria for location of balance planes and sensors.

To evaluate the feasibility and problems of balancing a rotor with flexural asymmetry, a rotor with a flattened shaft was designed to exhibit approximately 20 percent difference between the two bending critical speeds associated with the stiff and soft axes. Two problems were encountered with the shaft: first, a gravity excited natural frequency occurred at half the first bending critical speed and was made negotiable by increasing damping at the bearings and redistributing the rotor mass; and second, an unnegotiable instability was encountered when running at speeds above the lower of the two bending critical speeds. Redesign of the shaft to reduce the asymmetry eliminated the instability, and

successful balancing was then readily achieved. In support of the redesign, a general-purpose stability analysis for asymmetric rotors was developed and applied.

To evaluate the significance of static structure resonances on the case mounted probes, flexible probe holders were designed and tuned so that, in the region of the first shaft bending critical speed, a probe support resonance occurred, excited by the motion transmitted to the bearing pedestals. Balancing based directly on signals from the resonant probes was successful and uninhibited by this non-ideal condition. In parallel with this investigation, sensitivity of balancing effectiveness to tracking filter bandwidth and the availability of data from either one or two trial weight placements in each balancing plane was investigated.

To provide criteria for establishing ideal balance plane locations and for evaluating non-ideal locations, a formal analysis, based on damped modes of the rotor, was performed. This resulted in a penalty function which represented the amount of weight to be added or removed to correct a "unit" modal balance. This analysis was performed by Dr. J. W. Lund, Consultant to MTI.

The optimum plane location minimizes this function. The increase of this function above the minimum measures the "non-idealness" of the different plane configurations.

The main body of the report addresses the design and the experimental balancing of the rotor with flexural asymmetry. It further presents guidelines and criteria for selection of balance plane and probe locations, and demonstrates the evaluation and application of the criteria. The formal analyses for optimum balance plane locations and for stability of an asymmetric rotor are presented in two appendices to this report. A third appendix documents the balancing system used for the experimental studies.

Test Apparatus and Instrumentation

The basic mechanical apparatus and instrumentation system used for the recent balancing tests had previously been used for an extensive evaluation of flexible rotor balancing by the influence coefficient method (References 1, 2, and 3). The test machine shown in Figure 1 consisted of a three-mass, axis-symmetric rotor [1]* (described in detail in the following section), two tilting-pad journal bearings with supports [2], a double-acting, externally pressurized air thrust bearing [3], and a variable speed motor [4], with a spline coupling [5]. The mechanical components included two instrumentation brackets [6] mounted on a base plate [7] which, in turn, were attached to a ground-isolated structural steel base.

The journal bearings [8] were equipped with noncontacting seal rings on both sides for operation in the flooded condition. The lubricating fluid for the journal bearings was Dow Corning 200 with viscosities ranging from 0.65 cS to 65 cS as selected for different tests. Bearing fluid temperature rise in the bearings was monitored and generally kept below 6 C by circulation through water-cooled heat exchangers.

Instrumentation of the rotor system consisted of five pairs of noncontacting displacement sensors arranged in the vertical and horizontal planes along the length of the rotor [9-13]. The displacement sensors were of the capacitance type with a linear range of 0.25 mm. An optical proximity sensor was used for phase angle measurements between a fixed angular location on the rotor (reference mark) and the maximum dynamic displacement as it occurred at each of the measurement stations. All displacement sensor signals were displayed on oscilloscopes for monitoring of system performance, but only a selected number of signals were used for balancing. Those signals that were used for balancing were passed through a tracking filter and subsequently fed into a phase meter for phase angle measurement against the reference signal originating

*Numbers in brackets designate details in Figure 1.

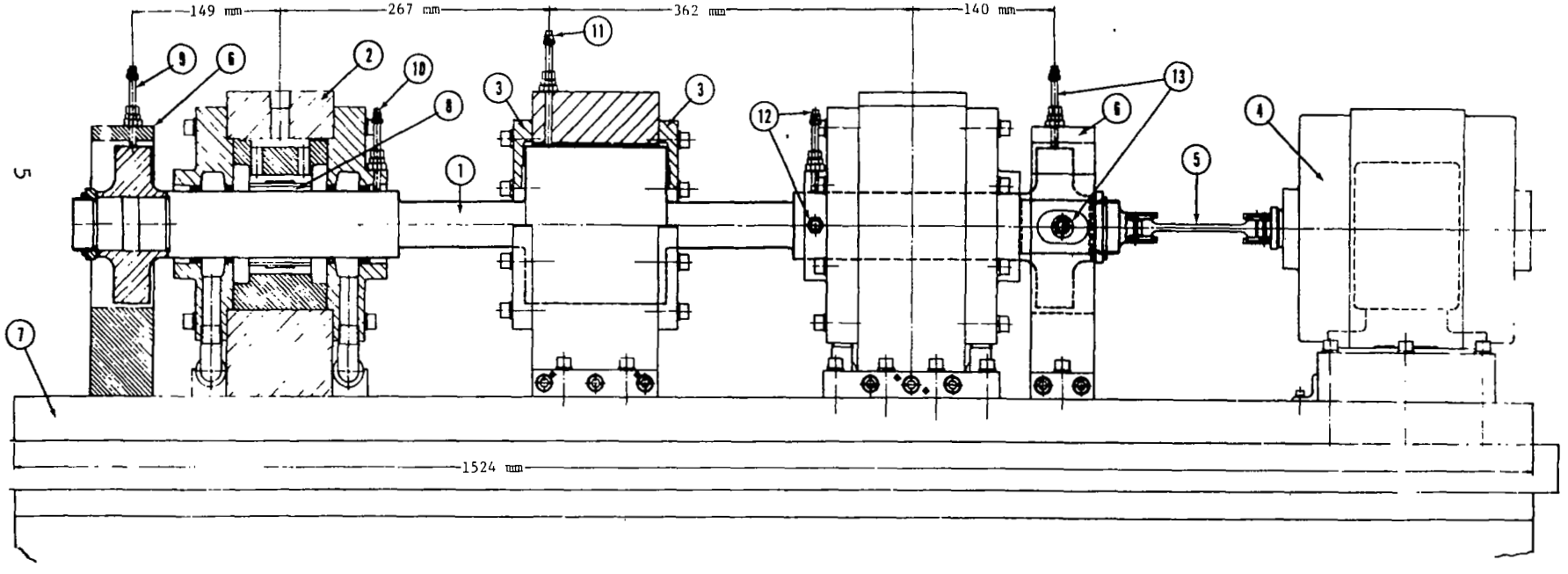

Fig. 1 Test Rig Assembly With Flat Shaft

from the optical proximity sensor. The sequential switching of the displacement signals through filter, phase meter, and readout instrumentation was accomplished automatically by the MTI Command™ Multiplane-Multispeed Balancing System, operated with an integral minicomputer. Calculation of balancing correction weights for selected sensors and speeds is fully automatic and operator-independent. (A detailed description of the MTI Command™ System is given in Appendix C.)

Design of Asymmetric Shaft

The three-mass test rotor shown in Figure 1 was 104.4 cm long and had a nominal bearing diameter of 63.5 mm. The center span between bearings was 60.4 cm. The center mass, 152.4 mm in diameter and 14.4 cm long, was integral with the shaft (see Figure 2a). Two end masses were overhung from the journal bearings (Figure 2b). End masses of 8.6, 4.94, and 1.13 kg were available for changes in rotor configuration as required during tests. Adjacent to the center mass, flat surfaces 12.7 cm long were machined on opposite sides of the rotor. Originally the flat sections had a diameter of 6.51 cm and were 4.48 cm across the flats.

In the course of the test program, the shaft diameter at the flat sections was progressively reduced, first to 5.72 cm and later to 4.80 cm.

The following table lists the combination of major diameters at the flat sections of the shaft and rotor end masses which were used for test purposes. Equivalent moments of inertia about the minimum and maximum stiffness axes of the flat sections of the rotor have been computed and used in the calculation of rotor-bearing system critical speeds.

A detailed design analysis was performed on the first combination listed in Table 1.

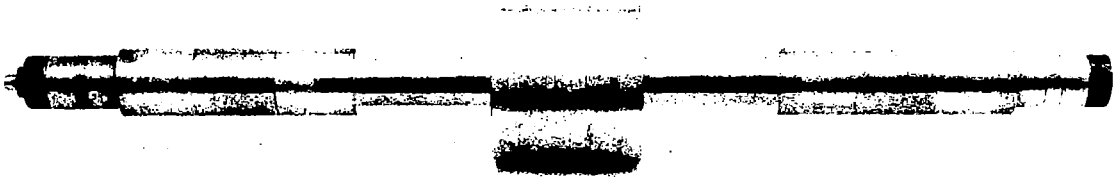

Fig. 2a Test Rotor with Integral Center Mass

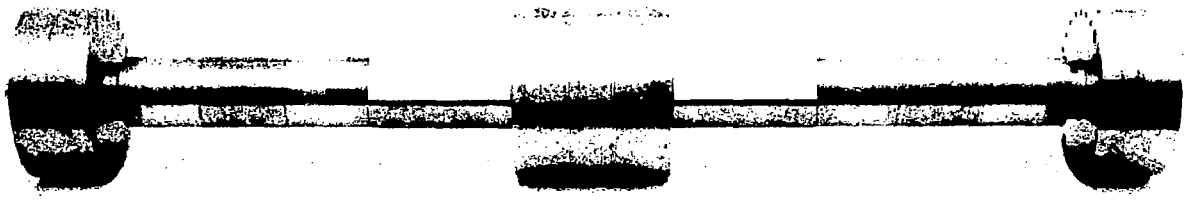

Fig. 2b Three-Mass Test Rotor with Detachable End Masses (8.6 kg each) and Flat Sections (12.7 cm long) Adjacent to Both Sides of the Center Mass

Fig. 2 Test Rotors

Table 1

TEST COMBINATIONS OF MAJOR SHAFT DIAMETER AND END MASSES

Major Diameter (cm)	End Masses (kg)
6.51	Both 8.6
6.51	Both 4.94
6.51	One 4.94 One 1.13
5.72	One 4.94 One 1.13
4.80	One 4.94 One 1.13

Figure 3 shows the expected trends for undamped third critical speeds calculated for the rotor-bearing system at a representative, but constant, bearing stiffness of 2.4×10^7 N/m for various ratios of the dimension across the flats (F) to the original rotor diameter (D). It should be noted that the third critical speed mentioned here is actually the first at which significant bending occurs and, therefore, the first at which flexural asymmetry effects can be expected to influence rotor dynamic behavior. The selected design point indicates a difference of approximately 2,000 rpm between the critical (bending) speeds that the rotor will exhibit about the major and minor stiffness axes. The difference in lateral natural frequencies of 15 to 20 percent was expected to result in pronounced and distinctively separate rotor-bearing resonances.

Figures 4 and 5 present critical speed maps for the modified rotor about its maximum and minimum stiffness axes, respectively. Since rotor weight is affected insignificantly through the material removal at the flat sections, the rotor bearing stiffness curves and the first and second (rigid body) critical speeds remain nearly unchanged.

The bearing stiffness curve for a preload factor of m = 0.3 is applicable to the test setup. The effect of increased bearing stiffness, as it might be obtained through preload increase to m = 0.5, has been included in the investigation as a limiting case.

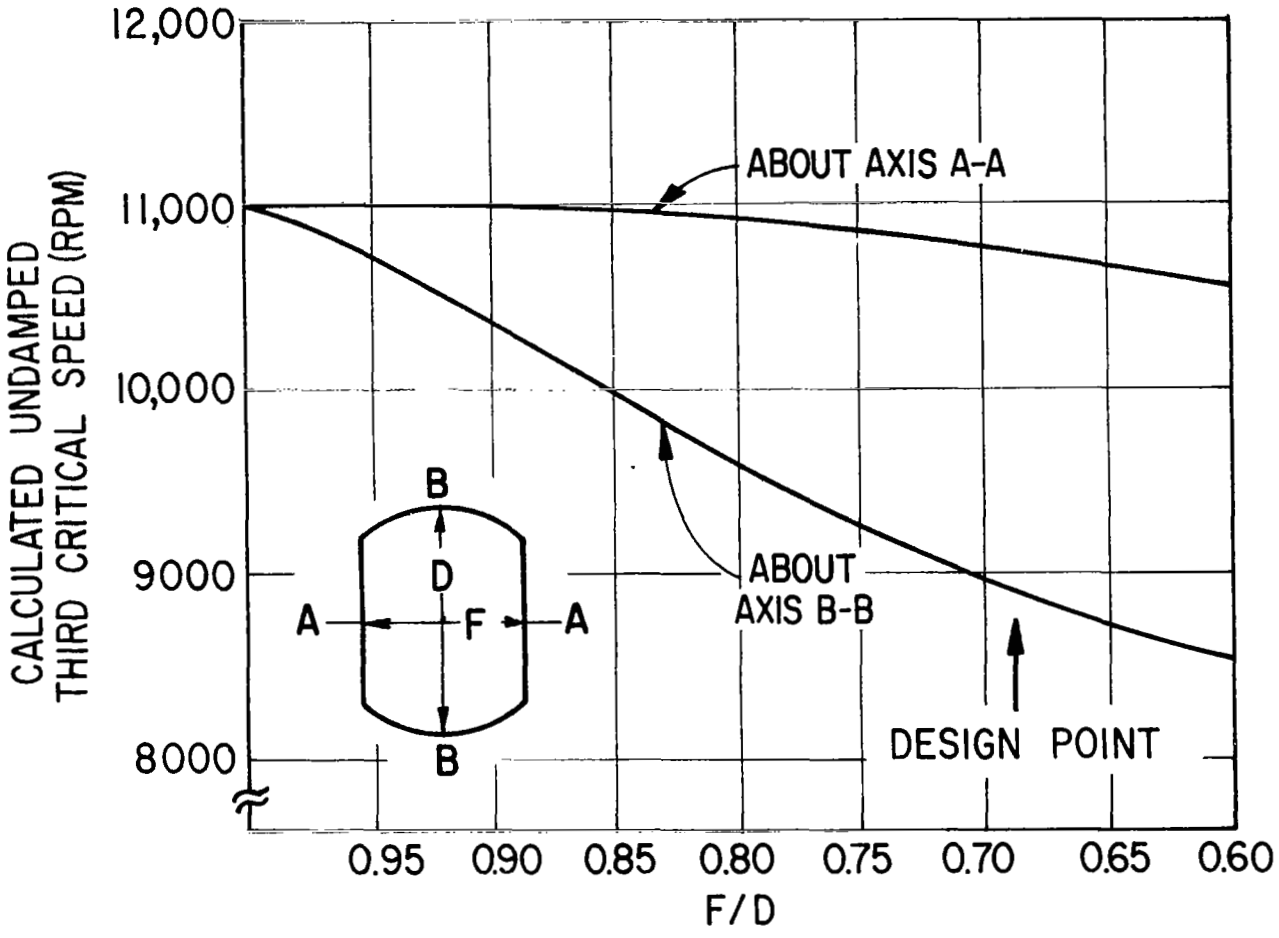

Fig. 3 Calculated Undamped Third Critical Speeds For The Modified Test Rotor With Flat Sections

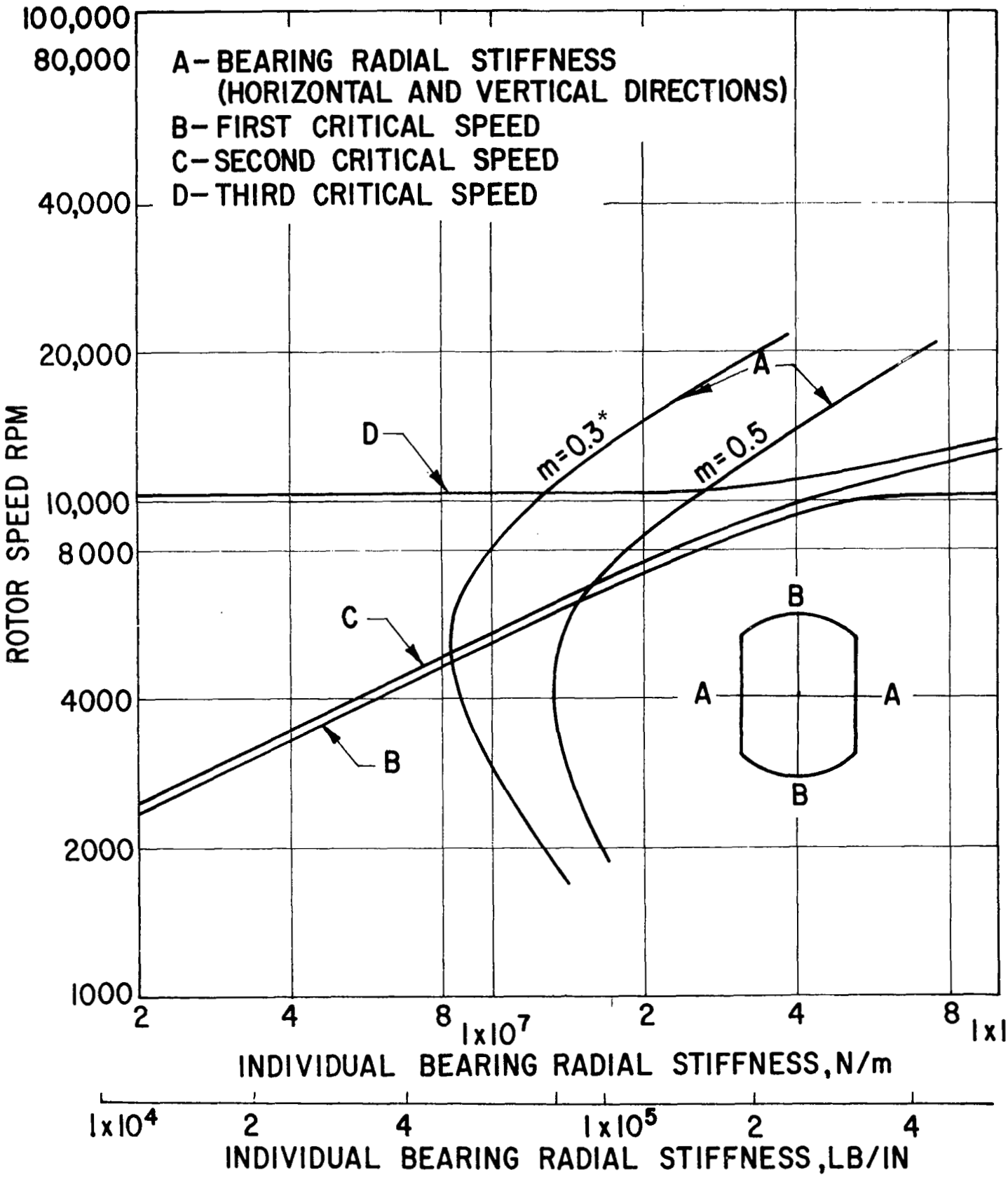

Fig. 4 Critical Speed Map For Flexible-Rotor Test Rig (Rotor With Flat Sections, Critical Speeds Associated With The Rotor Inertia Axis AA). *m is the preload ratio (1 - assembled clearance/machined clearance)

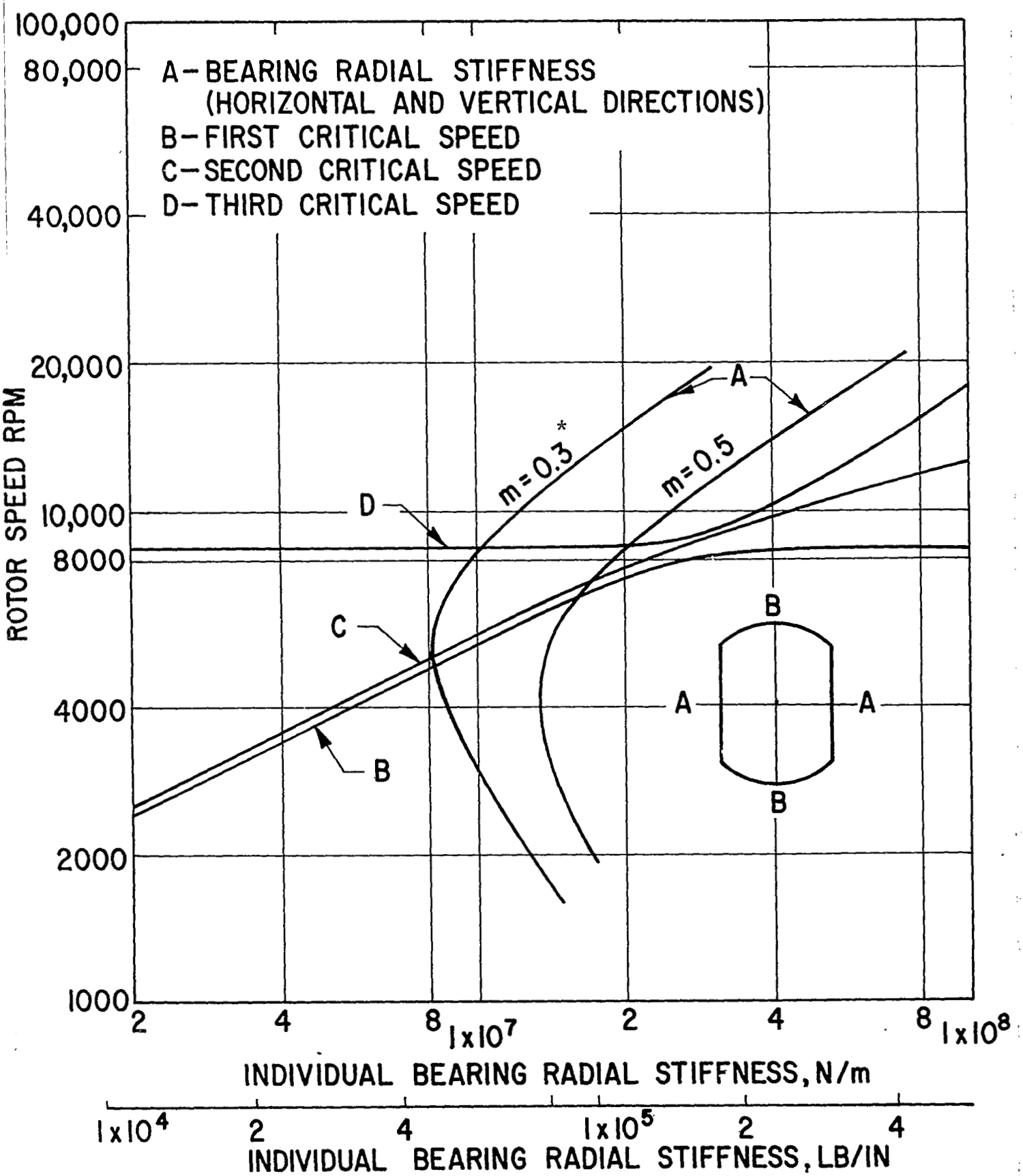

Fig. 5 Critical Speed Map For Flexible-Rotor Test Rig (Rotor With Flat Sections, Critical Speeds Associated With The Rotor Inertia Axis BB) *m is the preload ratio (1- assembled clearance/ machined clearance)

Figures 6 through 8 show the undamped rotor mode shapes at the first three critical speeds calculated with a bearing preload factor m = 0.3. The rotor mode shapes calculated about the major and minor inertia axes of the flat rotor are very similar at all three critical speeds. A slightly increased amount of bearing damping may, however, be expected at the critical speeds for the soft rotor axis from the small shift in nodal points at the third critical speed. Calculations of the damped rotor amplitudes at the third critical speed (Figure 9), occurring at 8434 rpm about the rotor inertia axis BB and at 10,763 rpm for axis AA, indicate lower amplitudes for the resonance occurring at the lower rotor speed. The amplitude ratio for the criticals about the two mutually perpendicular axes does not appear excessively distorted (considering the frequency difference between the two), indicating a moderate and thus acceptable effect of bearing damping at the lower third critical speed.

Figures 10 through 12 present calculated undamped rotor mode shapes at the first three critical speeds with a bearing preload factor m = 0.5. At the higher bearing stiffnesses which result from the increased bearing preload, the addition of flat sections on the rotor has a much stronger effect upon the difference in mode shapes. For the lower of the third critical speeds, considerable amplitudes now exist at the bearings, which might give rise to considerable bearing damping. Since it always has been our goal to create least favorable conditions for the balancing experiments, bearing setup clearances commensurate with a preload factor of m = 0.3 were selected.

Initial Test Results

The test results reported in this section refer to the test rotor with the initial major diameter of 6.51 cm and various end masses. A total of three rotor combinations were tested with the major diameter unchanged. These combinations are listed as the first three cases in Table 1.

The first rotordynamic phenomenon encountered at the initial test phase was caused by gravitational excitation and occurred when the rotor speed was one-half of the first bending critical speed calculated for the low stiffness axis of the rotor. The observed vibrations had a frequency of twice the rotor

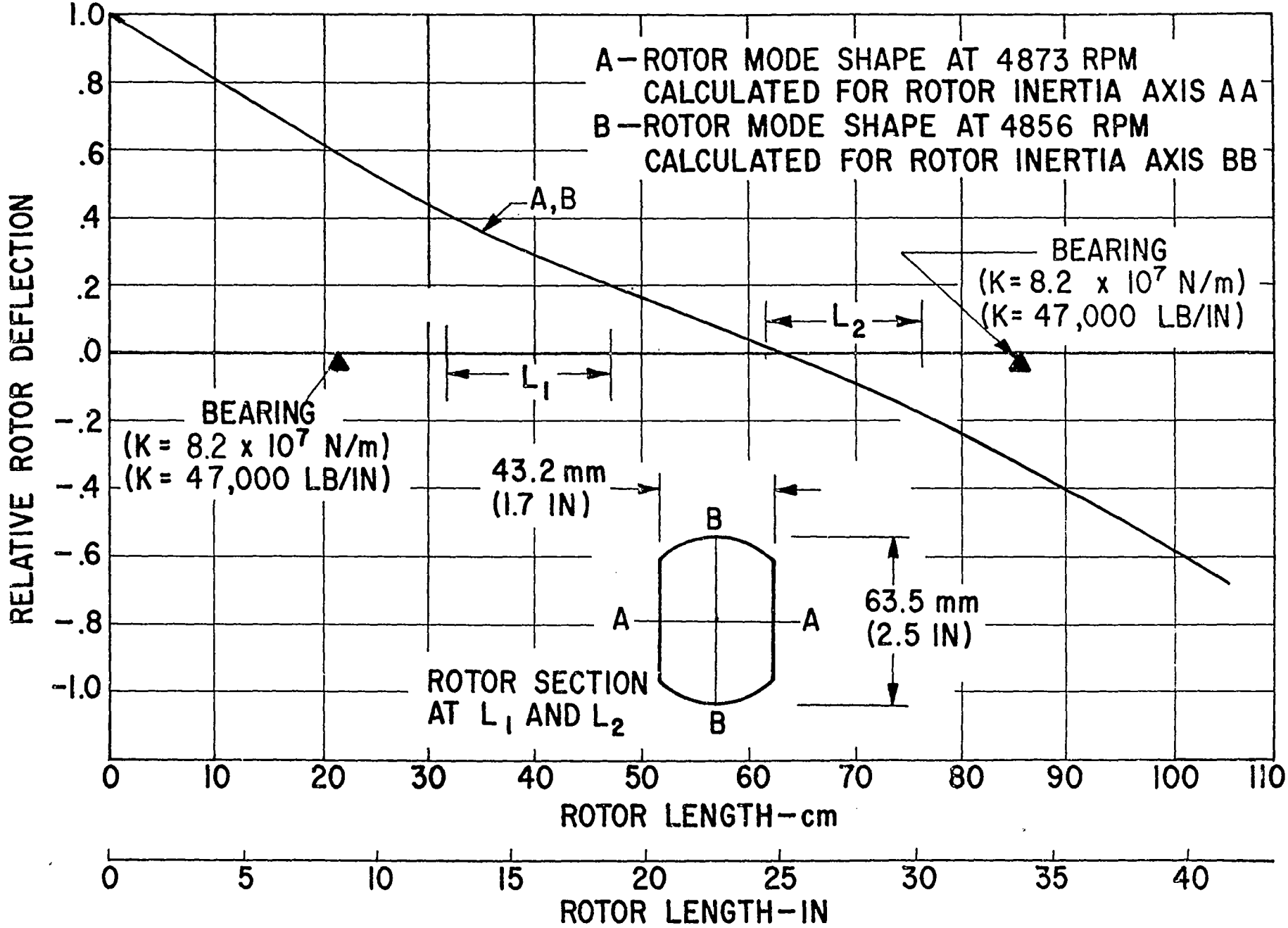

Fig. 6 Undamped Rotor Mode Shape At The First System Critical Speed For Test Rotor With Flat Sections (Bearing Preload m = 0.3)

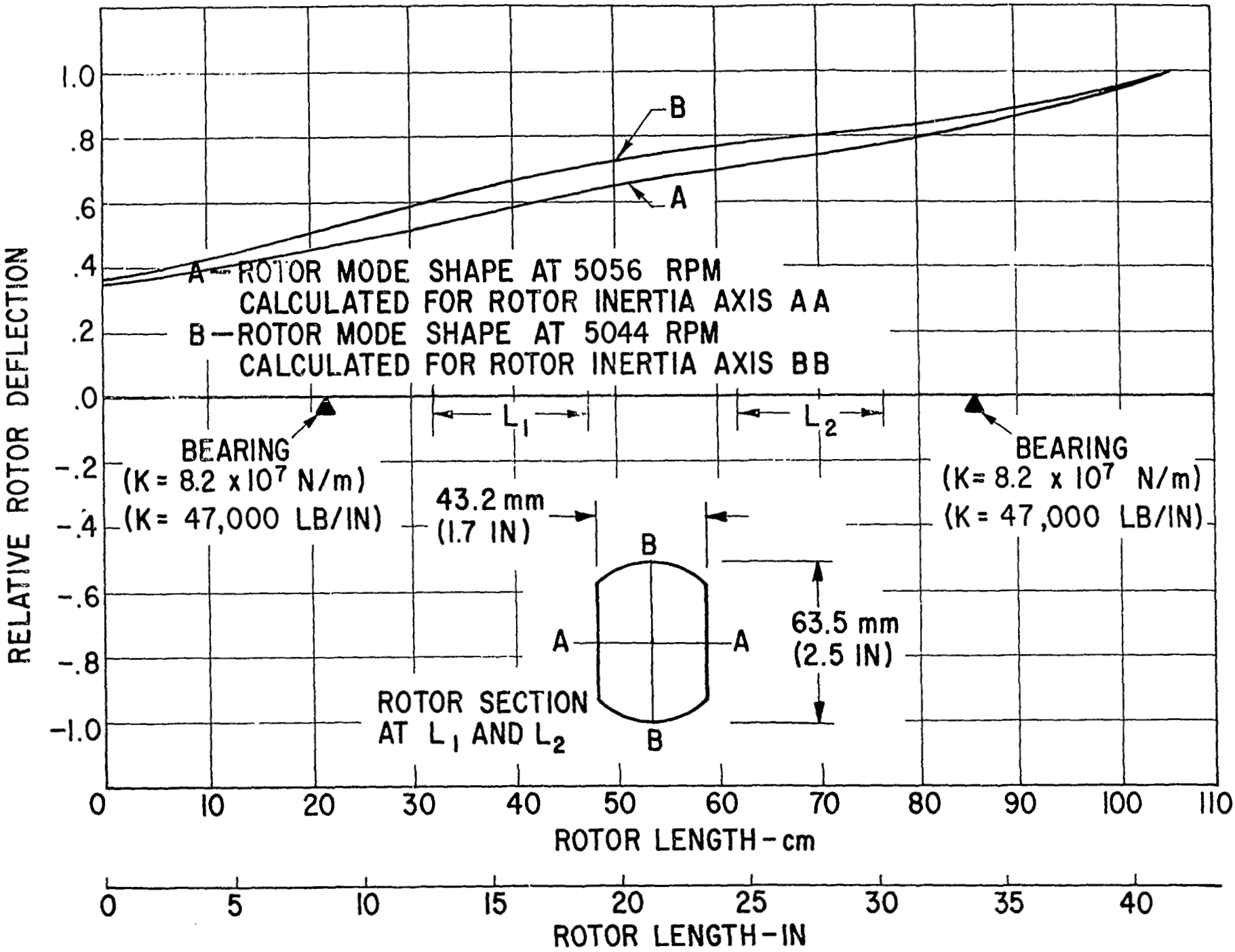

Fig. 7 Undamped Rotor Mode Shapes At The Second Critical Speed For Test Rotor With Flat Sections (Bearing Preload Factor m = 0.3)

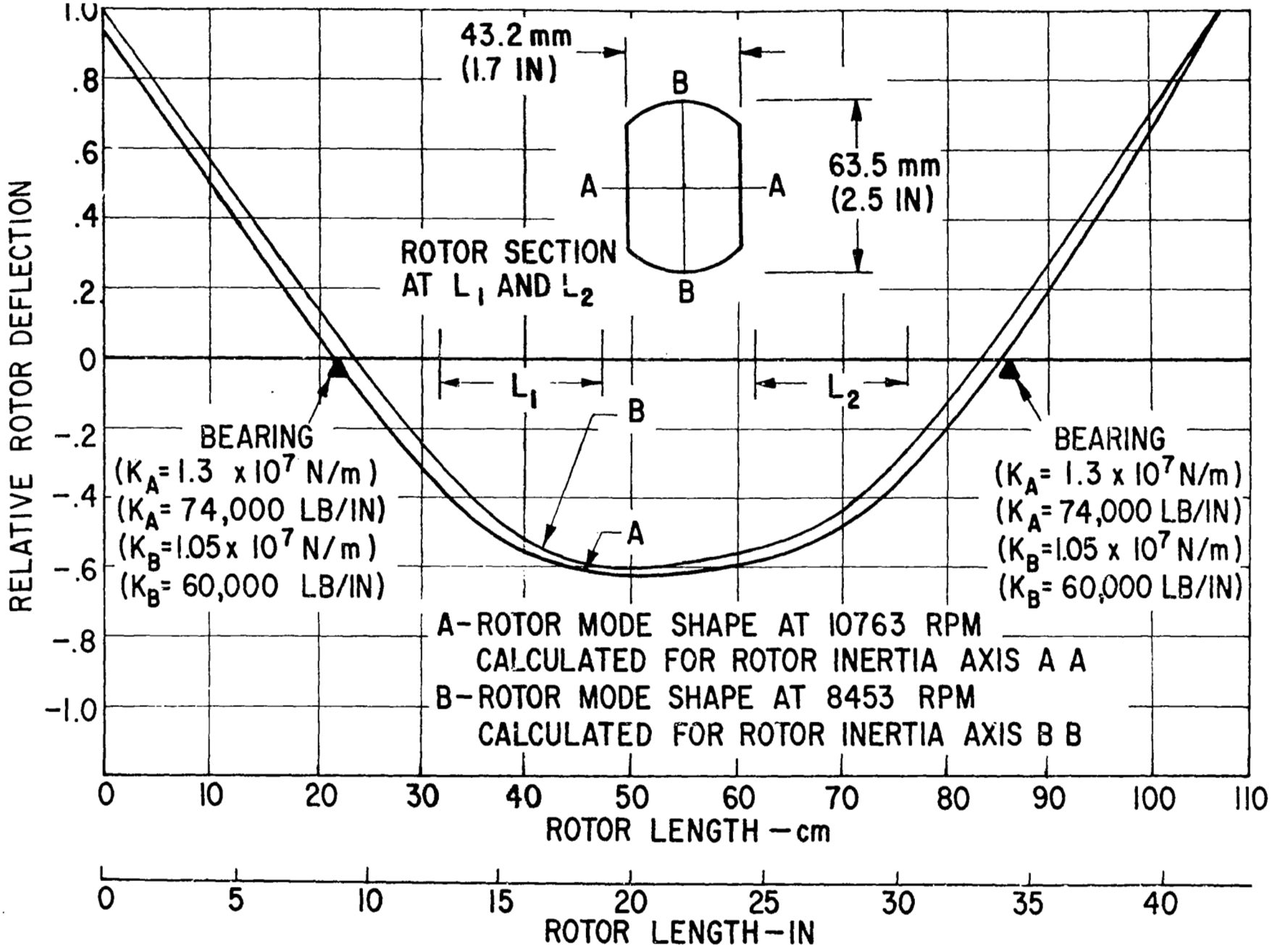

Fig. 8 Undamped Rotor Mode Shapes At The Third System Critical Speed For Test Rotor With Flat Sections (Bearing Preload Factor m = 0.3)

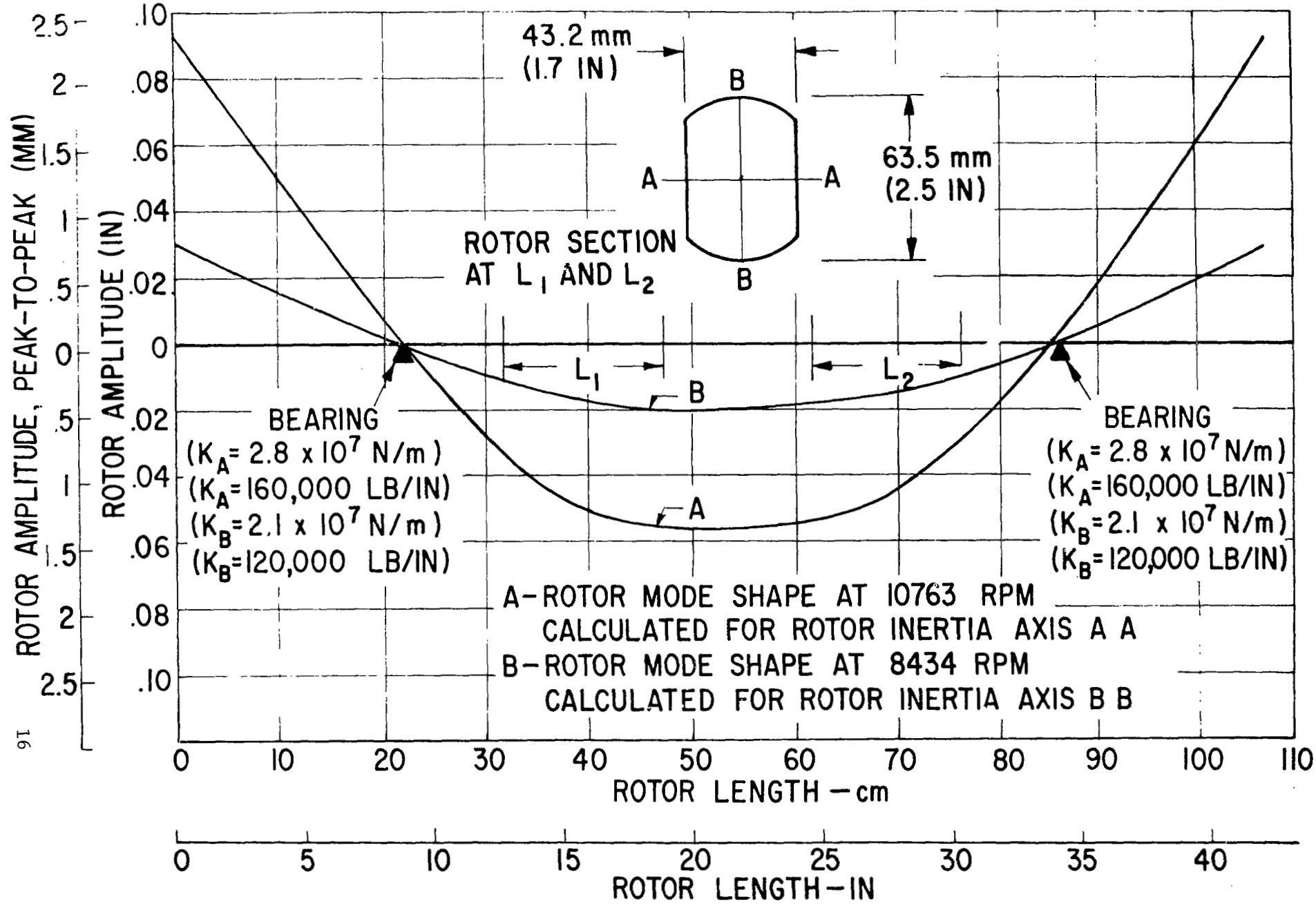

Fig. 9 Damped Rotor Amplitudes At The Third System Critical Speed For Test Rotor With Flat Sections (Bearing Preload Factor m = 0.3; In-Line, In-Phase Unbalance Configuration)

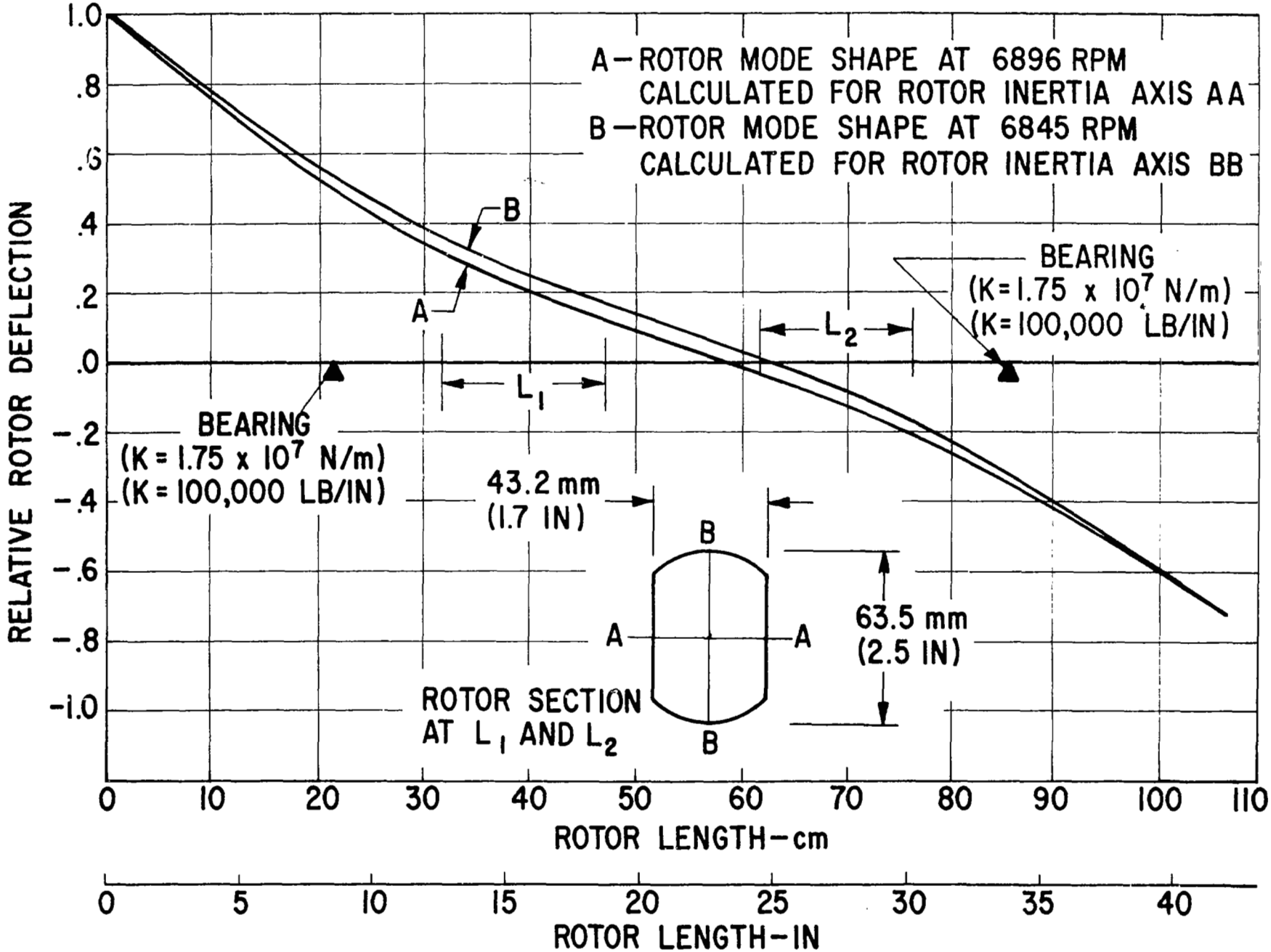

Fig. 10 Undamped Rotor Mode Shapes At The First System Critical Speed For Test Rotor With Flat Sections (Bearing Preload Factor m = 0.5)

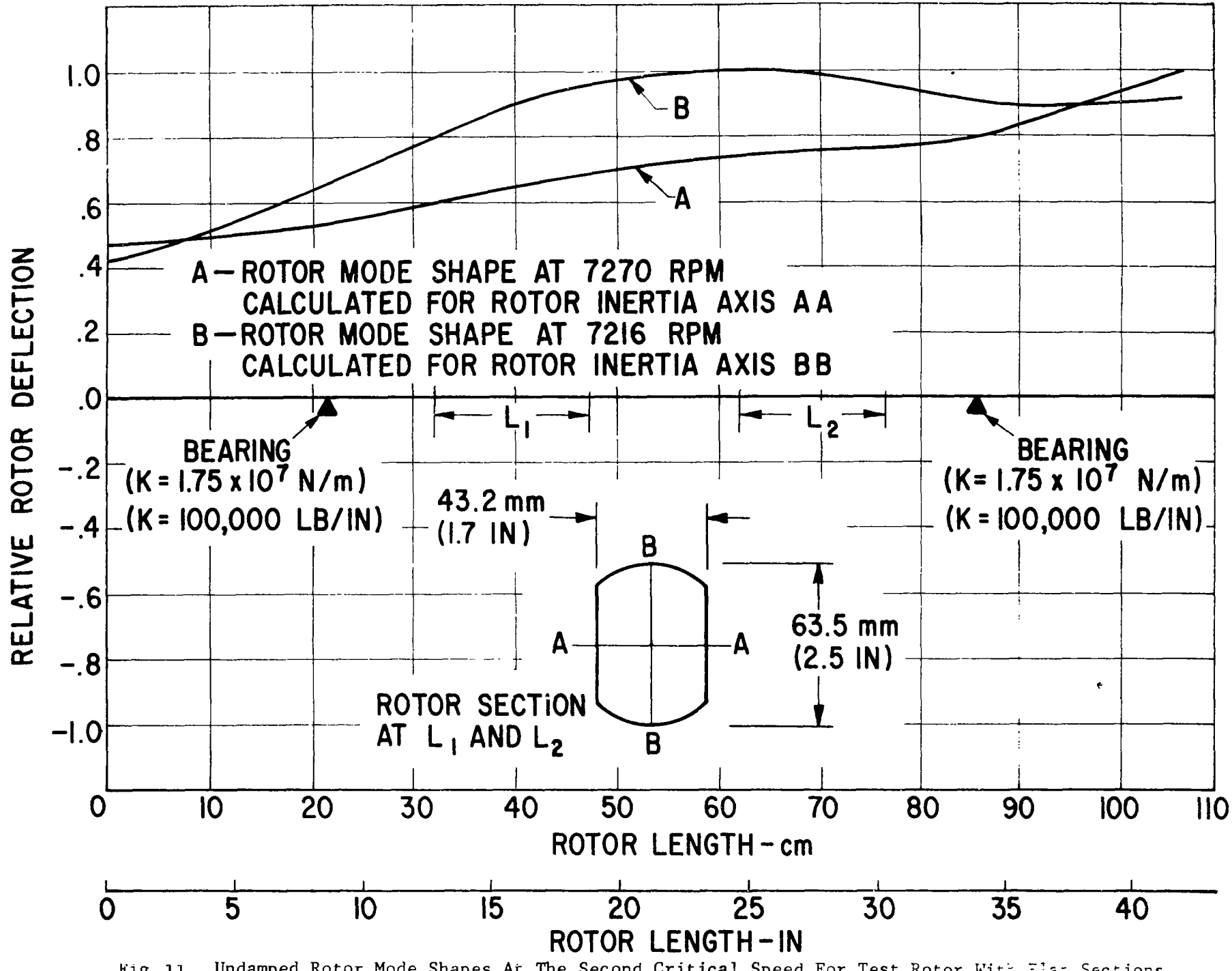

Fig. 11 Undamped Rotor Mode Shapes At The Second Critical Speed For Test Rotor With Flat Sections (Bearing Preload Factor m = 0.5)

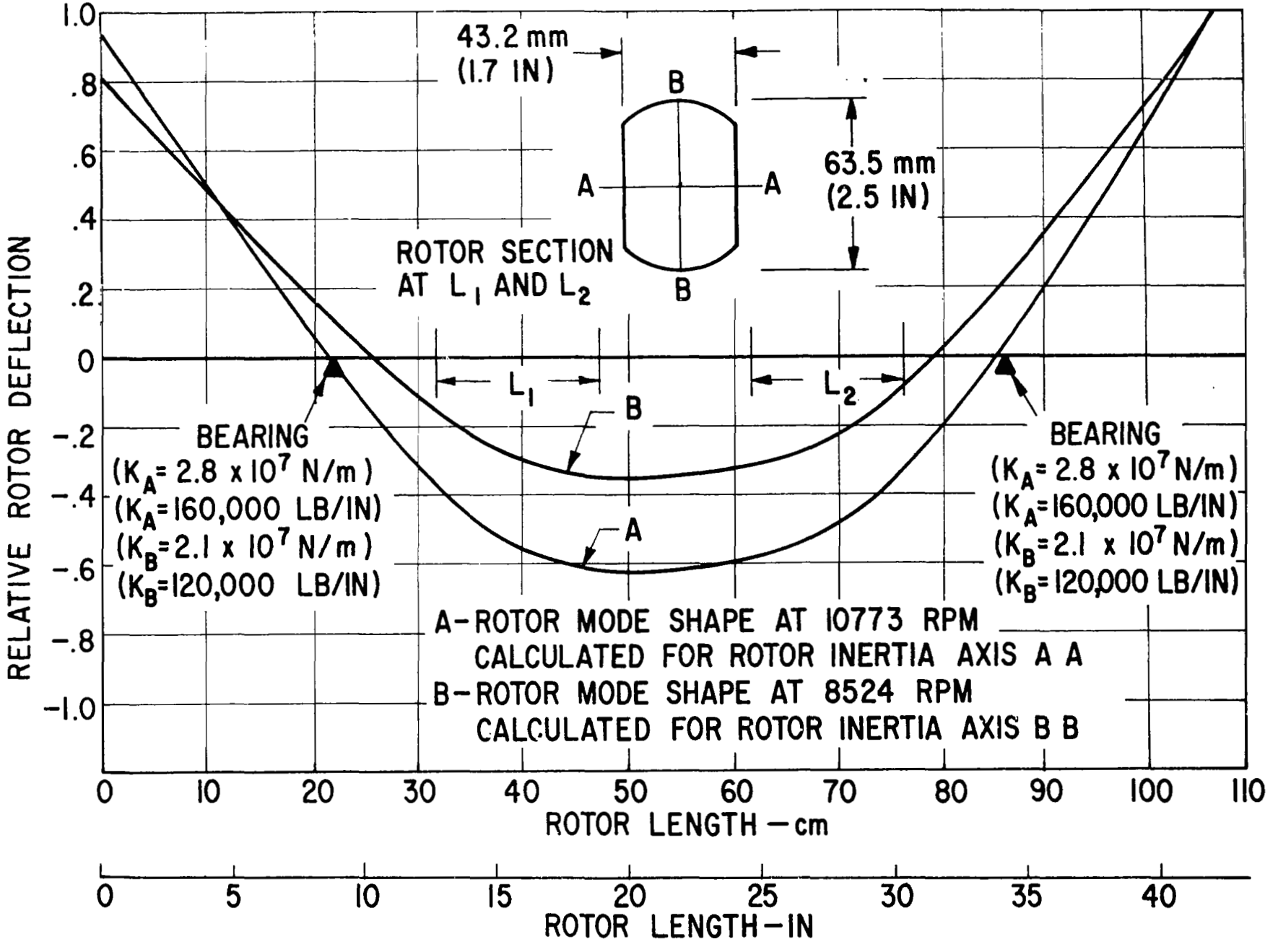

Fig. 12 Undamped Rotor Mode Shapes At The Third System Critical Speed For Test Rotor With Flat Sections (Bearing Preload Factor m = 0.5)

running speed. Typical observed rotor orbits are shown in Figure 13a for three measurement stations on the rotor. The orbits shown in Figure 13a were obtained at a rotor speed very close to half the first bending critical speed with the inner loop in each orbit picture nearly fully developed. When later it had become possible to negotiate the maximum amplitude peak caused by gravitational excitation, phase shifts of about 180 degrees on orbit displays were observed for all rotor stations. Considering the vibrational frequency of twice the shaft rotational frequency, the observed phase shifts occurred during a 90 degree interval of shaft rotation.

Rotor amplitudes caused by gravitational excitation were found to be quite independent of rotor unbalance, since an addition of significant amounts of unbalance did not increase noticeably the observed amplitudes.

For the original rotor configuration (Case 1 in Table 1), even significant increases in bearing fluid viscosity (from 0.65 cS to about 65 cS) did not produce enough bearing damping to reduce significantly the rotor amplitudes caused by gravitational excitation.

Reduction of rotor amplitudes caused by gravitational excitation to a level at which their peaks could safely be negotiated without endangerment of bearings and displacement sensors was achieved through a change in rotor configuration. When the rotor end masses (weighing 8.6 kg each) were replaced by lighter end masses of 4.94 kg each, the rotor could be operated through the speed range of the gravitation excitation to within 10 percent of the first bending critical speed. The rotor mass redistribution increased amplitudes at the bearings sufficiently to produce just enough damping to permit negotiation of the gravitational excitation region. The selected bearing fluid viscosity was 5 cS because increased bearing friction torque at 65 cS caused an undue load on the drive motor at speeds above 5000 rpm.

The second rotordynamic phenomenon associated with the flat shaft configuration was a violent, unstable vibration at the first bending critical speed. It made its first appearance, however, masked by amplitude growth due to unbalance excitation at the approach to the first bending critical speed (see Fig. 14, Curve A).

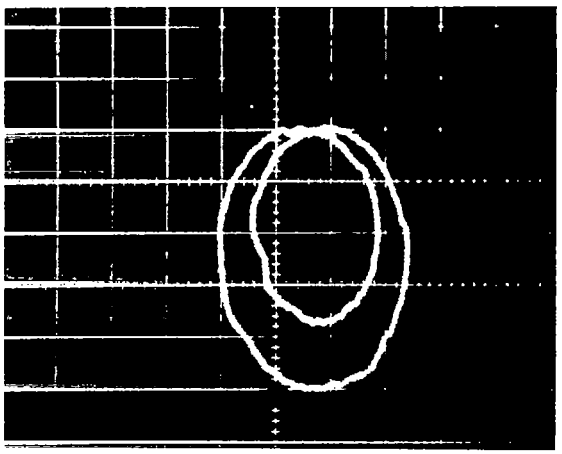

Station 1

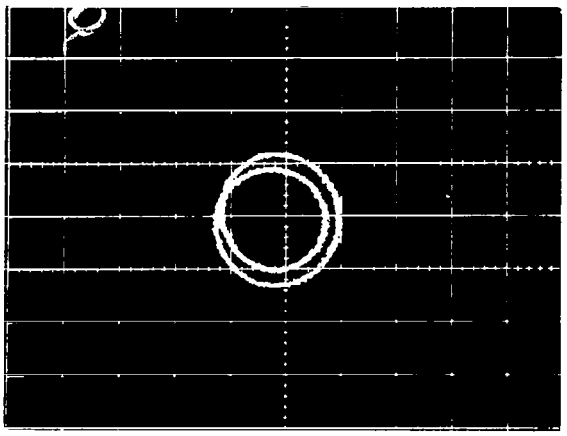

Station 4

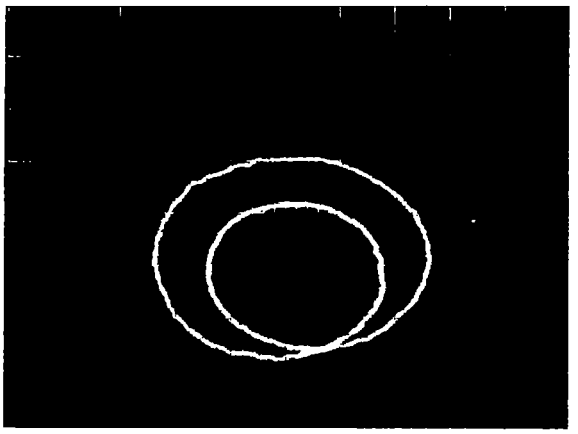

Station 5

One major division equals approximately
0.013 mm — Rotor speed = 4470 rpm

Fig. 13a Rotor Orbit Traces at Measurement Stations 1, 4, and 5

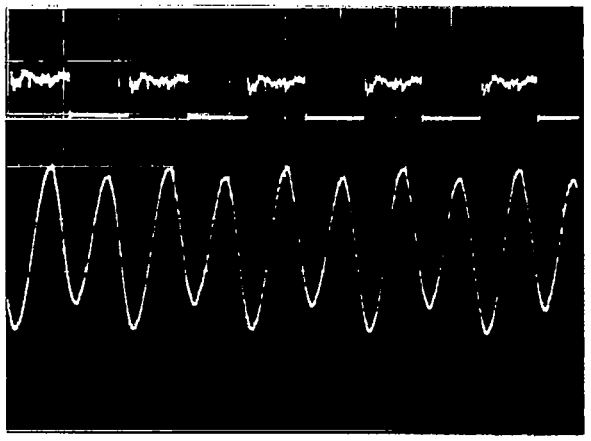

Fig. 13b Time Scan Signal at Station 1 with a Once-per-Revolution Reference Signal (above)

Fig. 13 Gravitational Excitation of Rotor with 6.50 cm Diameter at Flat Section

Approaching the first critical speed, the amplitude contribution from unbalance could be drastically reduced through multiplane balancing, so that the rotor would operate with only a minimal amplitude increase right up to a speed which appeared to be the first bending critical speed. At that point, however, the asymmetric rotor exhibited a step jump in amplitudes to what was considered a dangerous level. An amplitude plot of this occurrence is shown in Figure 14, Curve B.

There was no indication during any of these and the following tests that the rotor could be accelerated through this region of high amplitudes, despite some inadvertent forays into rather excessive rotor amplitudes. Consequently, it was deduced that the observed sudden amplitude increases were indeed the onset of instabilities predicted to occur between the two bending critical speeds associated with the different stiffnesses of a rotor with flat sections. The following effort was, therefore, directed, first, at further attempts to increase rotor-bearing system damping through rotor mass redistribution; and, failing that, an analytical and experimental investigation of the limits of rotor instability onset as a function of dissimilarity between rotor sections in the two mutually perpendicular axes.

Redesign of Test Rotor

The redesign of the test rotor for increased stability at and above the first bending critical speed proceeded in two phases. In the first phase, rotor mass distribution was further changed through substitution of one very light (1.13 kg) aluminum end mass for one of the steel end masses, and bearing fluid viscosity was again increased about tenfold. Neither action had the desired results of reducing the instability amplitude to a negotiable level. Consequently, rotor stabilization was now attempted through a reduction in the ratio of stiffnesses in the two rotor axes (fluid viscosity for all following tests was 5 cS). For machining simplicity, the major diameter was progressively reduced while the dimension across the flat sections remained unchanged. The

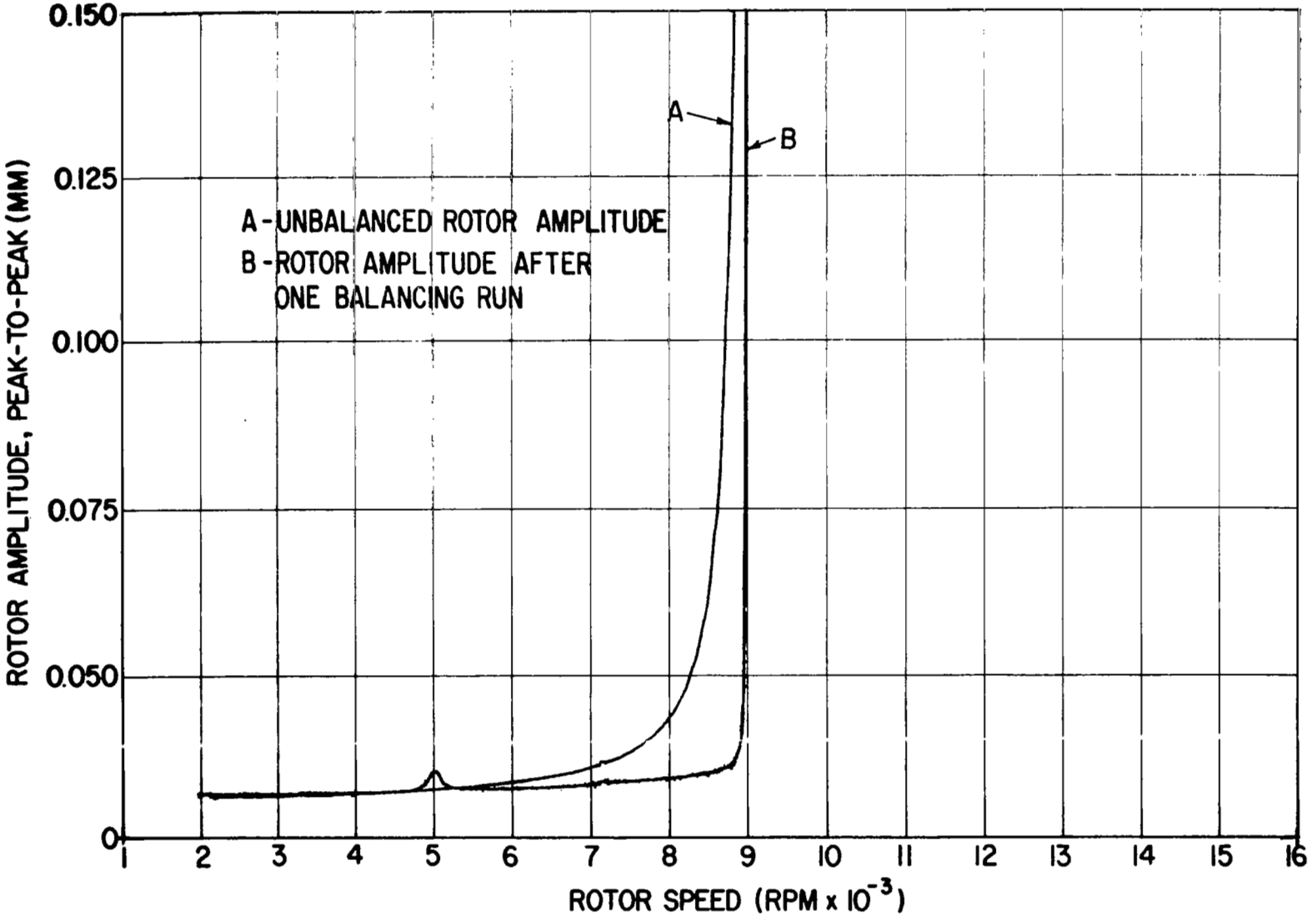

Fig. 14 Vertical Rotor Amplitudes at Shaft Center – Initial Condition and After One Balancing Run (Five vertical probes, rotor with flat sections and two unbalances 4.94 kg each)

reductions in shaft diameter also produced an increased flexibility of the rotor and a slight drop in the first bending critical speed with each reduction in shaft diameter.

To obtain guidance in finding what reduction in the major diameter, from 6.51 cm, would be necessary to stabilize the rotor, and what the influence of the intermediate values of diameter would be upon the state of stability of the rotor, an analysis was carried out. The analysis, entitled "Stability of a Shaft With Flexural Asymmetry" is given in Appendix B. The results of the analysis show that, when running speed was set close to or between the two first flexural critical speeds associated with the two principal axes, a pair of roots would be obtained from the equations of motion for free vibration of the rotor, both of which would be synchronous. For one root the real part would be negative, and for the other the real part would be positive. The latter is an unstable root since it will grow rather than decay with time.

The nature of the results is illustrated graphically in Figure 15, where the positive real part referred to above is plotted against rotor speed for different values of major diameters (with constant distance maintained across the flats). For values of major diameter between 5 and 6.35 cm, an unstable speed range is indicated where the width of the speed range and the peak value of the real part of the root (S) increase with increasing major diameter. The indication is that a sufficient decrease in major diameter would shrink the height and width of the unstable speed range to zero. Interestingly, this dimensional change also shifts the unstable speed range to lower speed values since the overall flexibility of the shaft is increased.

In Figure 16, the relationship between the maximum value of the real part of S and major diameter D is shown for two different mass distributions. In one case (the "original" rotor which could operate above the region of gravitational excitation), the masses at either end are 4.94 kg. In the second case, one of the masses has been reduced to 1.13 kg — a change which changes the mode shape of the flexural critical speed slightly, increasing amplitude at the bearings and increasing the potential for damping. Clearly, the lighter end mass allows a stable rotor to be achieved with a larger major diameter, 4.80 cm as opposed

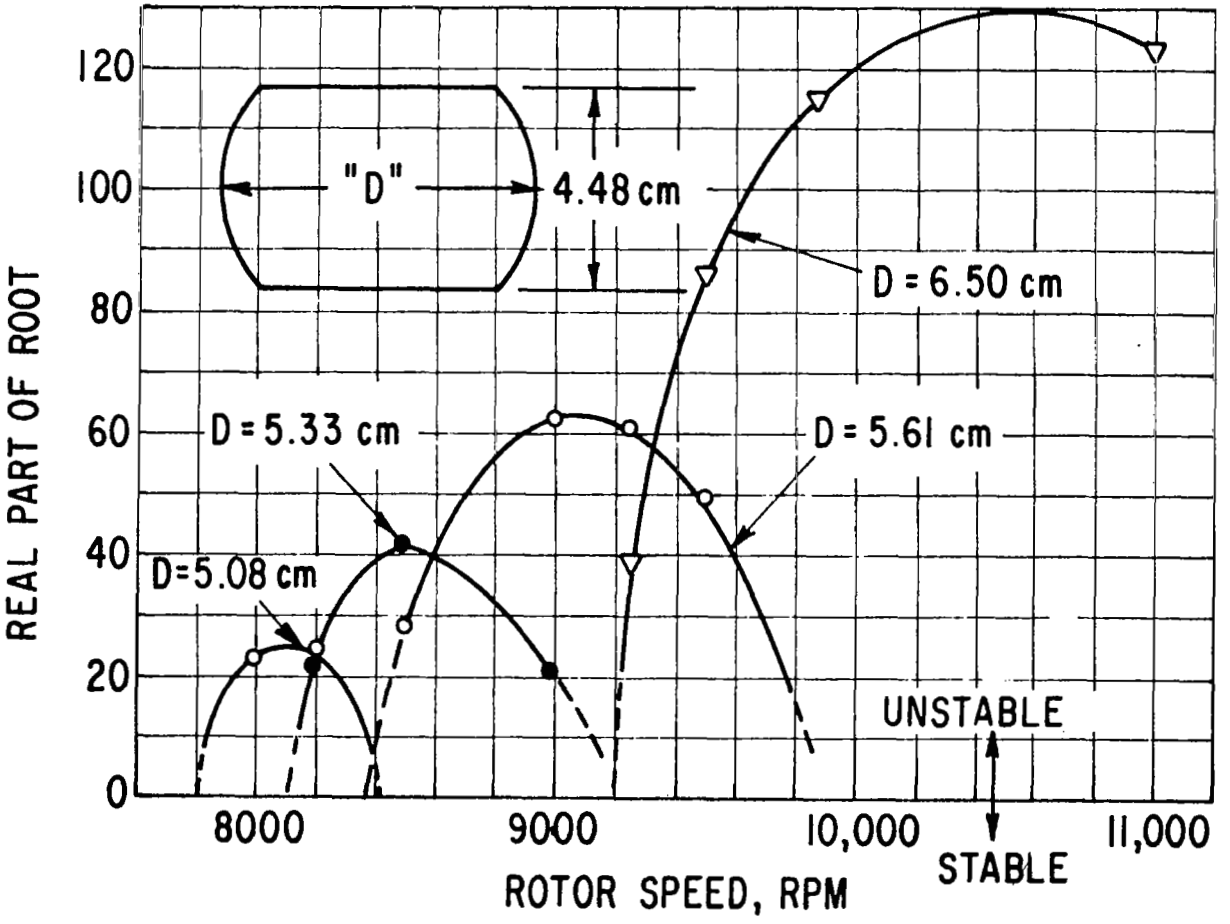

Fig. 15 Stability Analysis - Real Part of Root vs Speed for Different Major Diameters

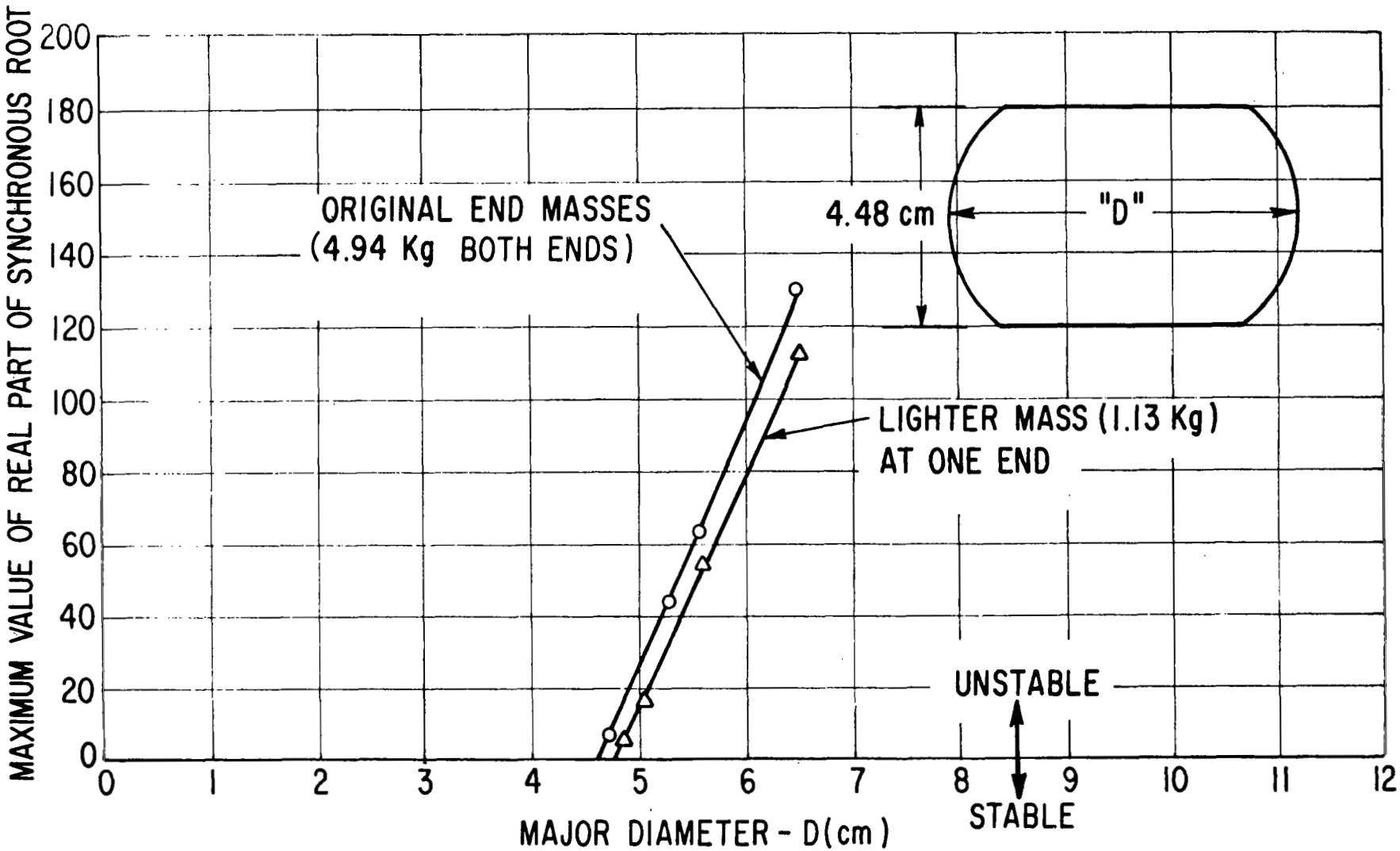

Fig. 16 Stability Analysis - Real Part of Synchronous Root versus Major Diameter (Distance Across Flats = 4.48 cm)

to 4.62 cm. However, even 4.80 cm represents only a seven percent difference between major diameter and the distance across the flats; surprisingly, such an apparently small asymmetry can destabilize the rotor.

Table 2 presents a summary of cases examined for stability of rotor operation above the first bending critical speed. Only those rotor configurations, which could be safely operated through the gravity-excited critical speed, were considered.

Verification of the stability analysis was obtained concurrently with balancing experiments, when each of the rotor configurations was balanced so that low rotor amplitudes were obtained either right up to the stability limit, or for operation through the first bending critical speed. Balancing results are described in the next section.

Table 2

ROTOR CONFIGURATIONS AND CONDITIONS

Rotor Configuration Number	Diameter Across Flats (cm)	Major Diameter (cm)	End Masses (kg)	Condition (Predicted and Observed)	Threshold of Stability Predicted	Threshold of Stability Observed
1	4.48	6.50	Both 4.94	Unstable	9200	9000
2	4.48	6.50	One 4.94 One 1.13	Unstable	9500	9300
3	4.48	5.72	One 4.94 One 1.13	Unstable	8800	8750
4	4.48	4.80	One 4.94 One 1.13	Stable (lightly damped)	--	--

BALANCING RESULTS

Balancing With Flexural Asymmetry

Without in-place, multiplane balancing it might not be possible to detect the onset of rotor instability when approaching the first bending critical speed. This is demonstrated in Figure 17 for the rotor with major diameter of 5.72 cm and unequal end masses where the well-balanced rotor (balanced in two planes on a commercial balancing machine) was run up close to its first bending critical speed (Curve A). When most of the remaining rotor unbalance had been removed by in-place balancing, utilizing the Multiplane-Multispeed Balancing Method, with data taken at approximately 8600 rpm, the rotor system critical speed could be approached much more closely with very low rotor amplitudes (Figure 17, Curve B). However, at 8750 rpm there was a pronounced and sudden jump in amplitude, with a slope discontinuity not characteristic of resonant response. Further attempts to reduce amplitudes by balancing were unsuccessful even though the frequency of vibration was synchronous with rotor speed. Similar characteristics were observed for all of the unstable configurations presented in Table 2.

Successful balancing of rotors with flat sections was found to be dependent upon trial weight placement in the "soft" axis of the rotor. This conclusion was obtained from experimental tests where a rotor with significantly different stiffnesses in the two axes was balanced for the first critical speed, which is associated with the "soft" rotor axis. Where trial weights would have to be placed in such rotors for balancing through both critical speeds (associated with the soft and stiff rotor axes) remains, at this time, academic, due to the encountered instability. When the rotor was made stable through reduction in the stiffness difference between the two axes, separate peaks were no longer observable, and the trial weight location became unimportant.

Unbalance was added in a "corkscrew" arrangement, with the first weight placed at the zero degree location at the back of the disk opposite the rotor drive end and the successive weights placed in the following disk at 90 degree intervals opposite to the direction of rotation of the rotor. For one of the unstable rotor configurations (rotor with 6.51 cm major diameter of the flat section), a rather severe case was designed to test the Multiplane-Multispeed

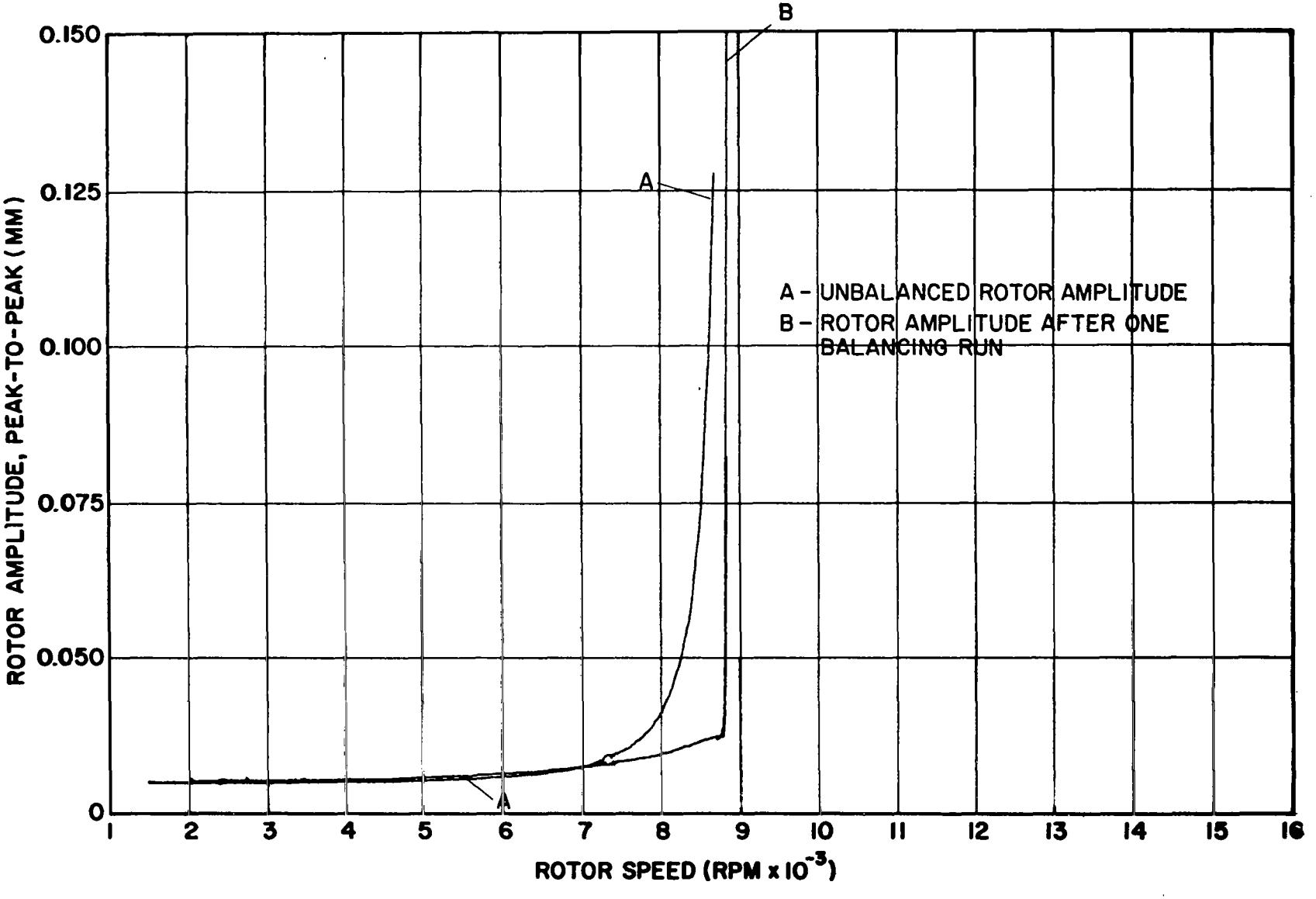

Fig. 17 Vertical Rotor Amplitudes at Shaft Center — Initial Condition and After One Balancing Run by the Least Squares Procedure (Four vertical probes, rotor with 5.72-cm diameter at flat sections and one aluminum end mass)

Balancing Method. The initial response and balancing results are partially documented in Figure 18. Shown are rotor amplitudes at the shaft midpoint section of the intentionally unbalanced test rotor. Even with a relatively large amount of unbalance added to the rotor, the first balancing run was still very effective (Curve B). This was surprising because, for at least one rotor plane, the "corkscrew" unbalance distribution placed significant unbalances in the stiff axis of the rotor; whereas influence coefficients were determined only for trial weights placed in the soft rotor axis; resultant corrections were expected to be insufficient. (The increased stiffness of the rotor in the "stiff" direction tends, of course, to reduce the rotor deflection effect due to unbalance located there, thus effectively compensating for the rotor stiffness variation for angular locations between the soft and stiff axes.)

Only when the diameters at the flat sections were further reduced to 4.80 cm, which is the largest predicted diameter at which the rotor would remain stable at the first critical speed with flat sections of 4.48 cm, could the rotor readily be balanced to operate at and above the first critical speed (Figure 19).

Curve A of Figure 19 is for the rotor in its initial state of unbalance, and Curves B and C show the results of successive balancing operations. Nowhere on the curves is there the pronounced and sudden increase in amplitudes of Figure 16, Curve B.

The rapid, but finite, amplitude buildup at the critical speed indicates a very lightly damped system, thus confirming the prediction from the stability analysis presented in Table 2. As a measure of the system damping, the log decrement can be determined, approximately, from the shape of the response curve as follows:

$$\delta \simeq \pi \left[\frac{f^{+} - f^{-}}{f_n} \right] \tag{1}$$

where f^{+}, f^{-} are the frequencies of the points at which the amplitude equals $1/\sqrt{2}$ times the peak amplitude and f_n is the resonant frequency (Hz).

The real part of the computed system eigenvalue (λ) can be calculated as $(-f_n)$ times the log decrement.

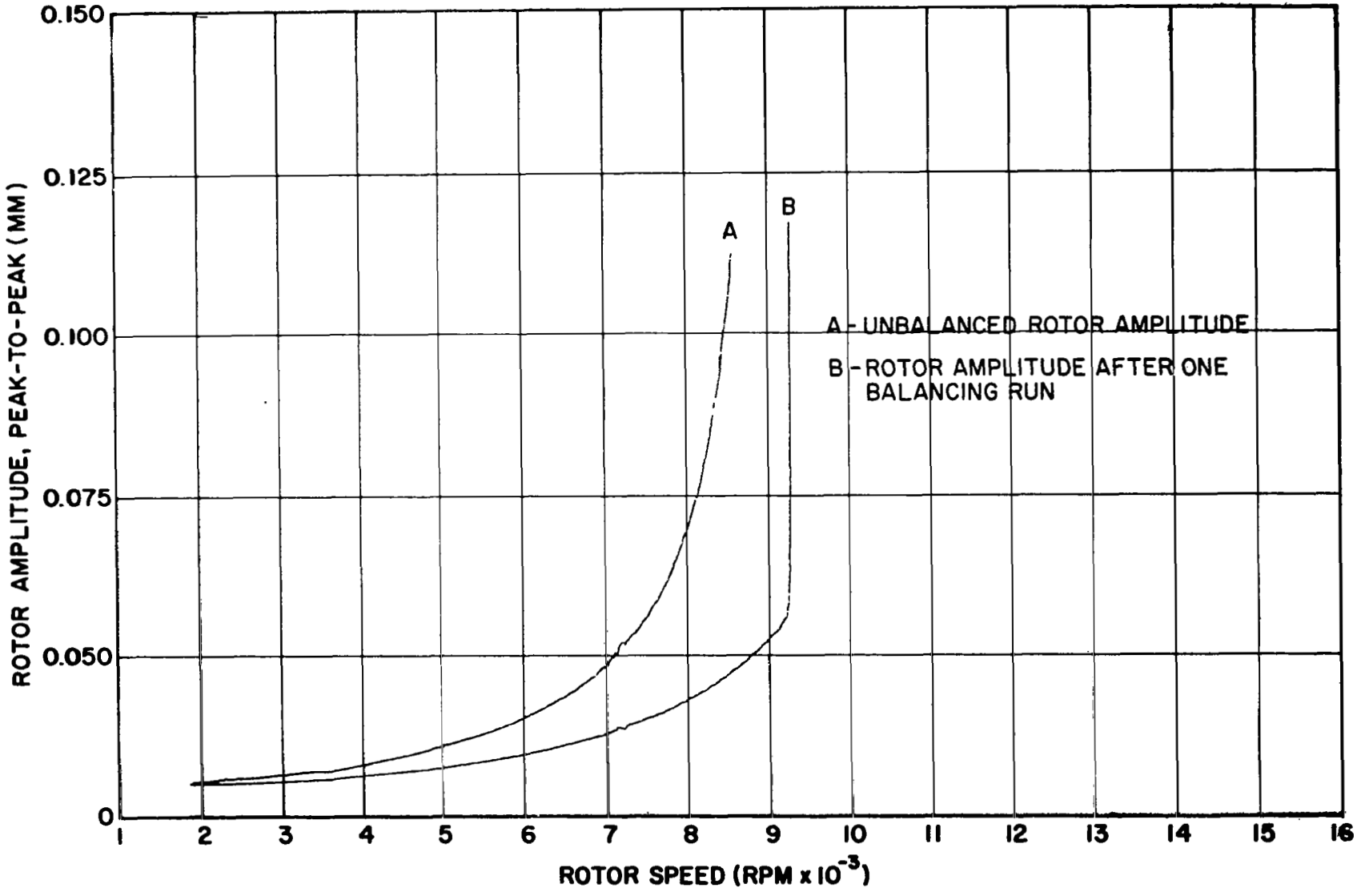

Fig. 18 Vertical Rotor Amplitudes at Shaft Center — Initial Rotor Condition (Corkscrew Unbalance Distribution) and After One Balancing Run by the Least Squares Procedure (Five vertical probes, rotor with 6.51 cm Diameter at Flat Sections and one aluminum end mass)

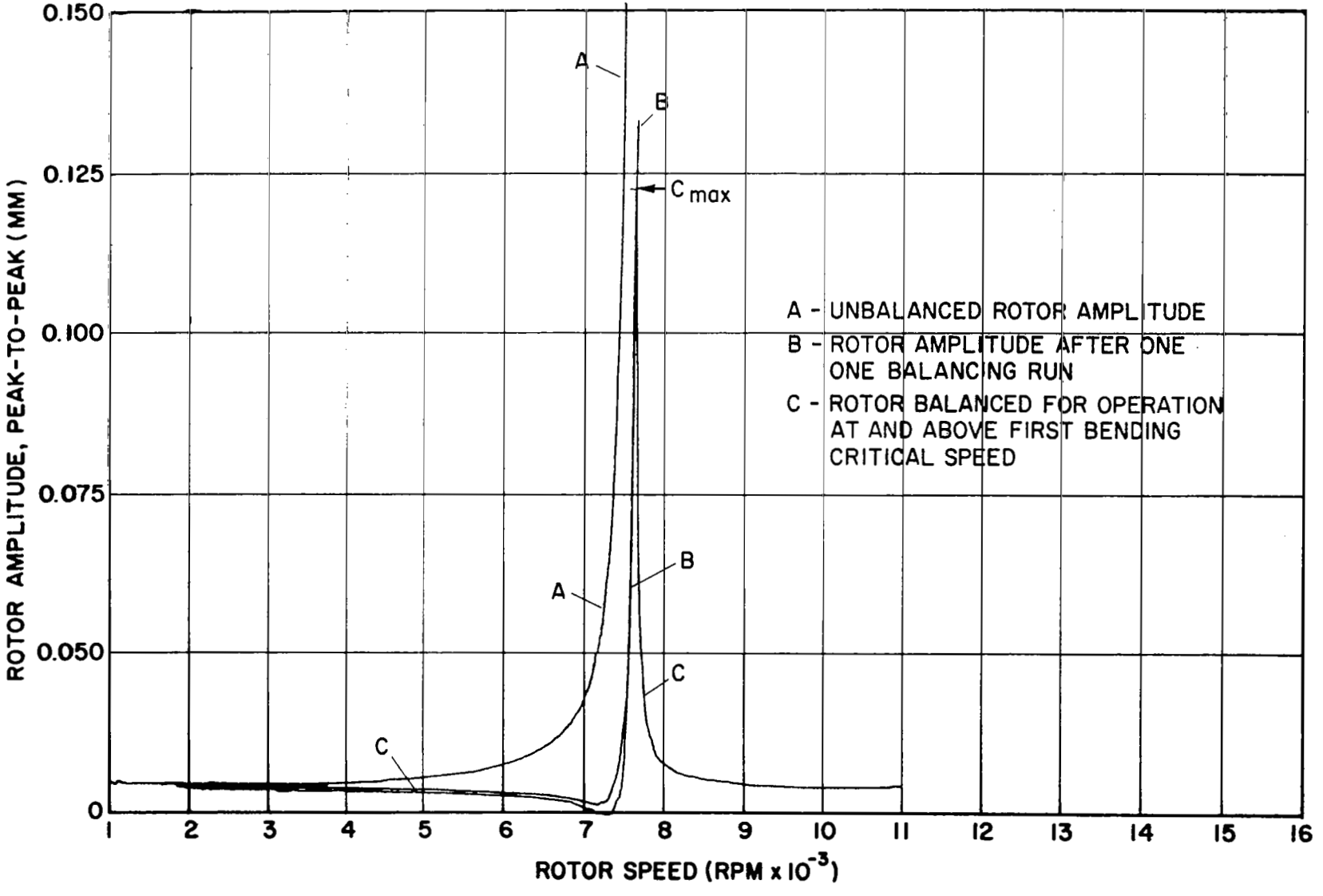

Fig. 19 Vertical Rotor Amplitudes at Shaft Center — Initial Condition and After One and Two Balancing Runs (Four vertical probes, rotor with 4.80-cm diameter at flat sections and one aluminum end mass)

From Figure 19, Curve C, these calculations yield a log decrement of 0.013 (equivalent to a damping ratio of 0.002) and the real part of the complex eigenvalue, $\lambda = -1.62$. When this value for λ is compared to the predicted worst value of +130 on Figure 16, a quantitative indication of the marginal nature of the stability of this configuration is obtained. The fact that the Multiplane Balancing Method can balance such a lightly damped rotor is confirmation of the effectiveness of the method under non-ideal conditions.

Balancing With Resonant Probe Holders

Part of the balancing experiments included the use of flexibly mounted probe holders as shown in Figure 20. The cantilevered construction, with the probe holders hard mounted to the bearing housings, was sensitive to changes in probe mass which allowed for adjustments in probe holder resonant frequency. The bearing housing vibration was used as the input excitation for the flexible probe holder. Masses were clamped to the cantilever probe supports until their individual resonant frequencies were close to the critical speed of the rotor. This condition was created to approximate the effects of structural resonances on the capability of the balancing system.

Three displacement sensors were mounted to the flexible probe holders. These three probes were directed at rotor surfaces on each of the three rotor disks. An accelerometer was placed as close to the displacement sensor as possible so that the vibration of the holder could be isolated from that of the shaft. Figure 21 shows the typical resonance characteristic of the probe holders during the initial test runs with an unbalanced rotor.

A large distributed unbalance in the rotor was selected to create high vibration which would excite the flexible probe holders. When the rotor was initially accelerated to 6000 rpm, the excursions of the displacement sensor, relative to the rotor center disk, exceeded the linear range of the instrumentation above 5800 rpm. The response of the rotor at three sensor locations relative to the flexibly mounted displacement probes is shown on Curve A of Figures 22 through 24. Since all three of these sensors were individually mounted, the resonances of the flexible probe holders are reflected in the amplitude curve. The resonance frequencies of the cantilevered probe holders are clearly observed

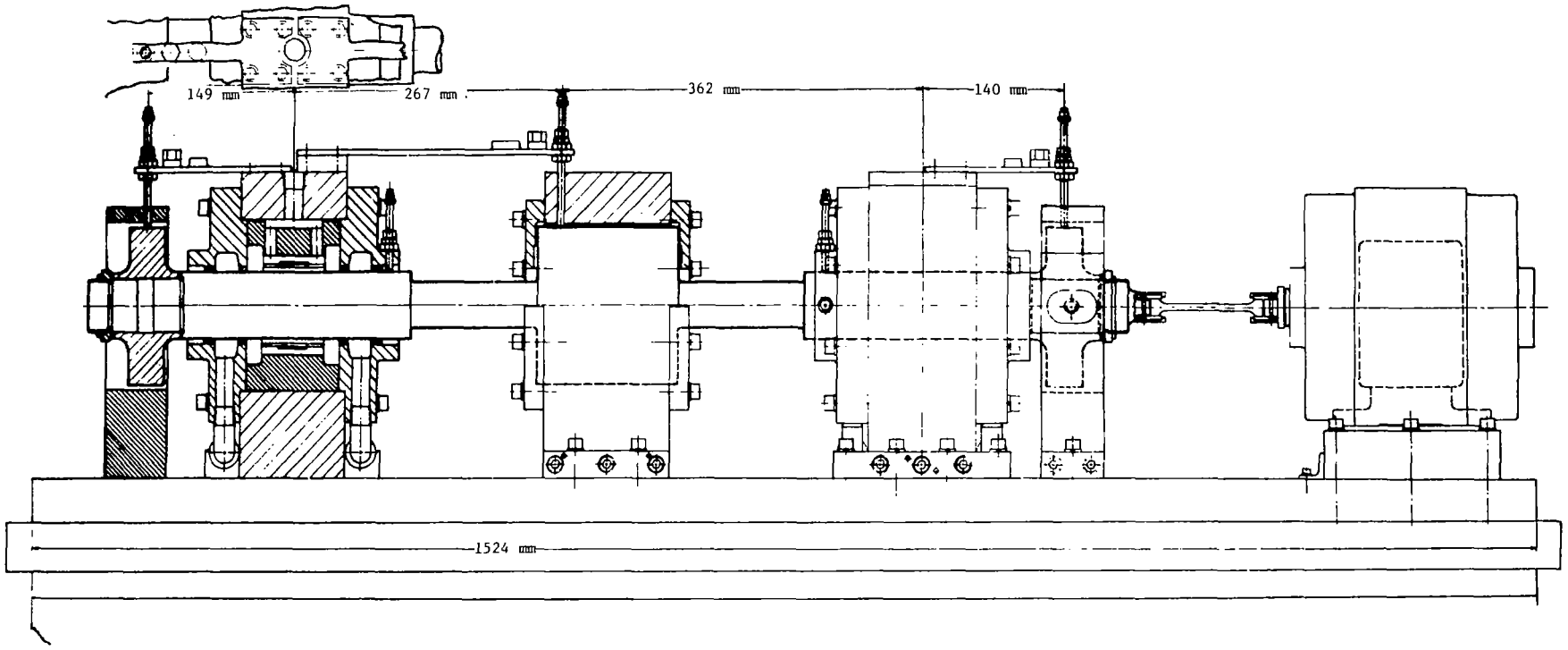

Fig. 20 Test Rig with Flat Shaft and Flexibly Mounted Probe Holders

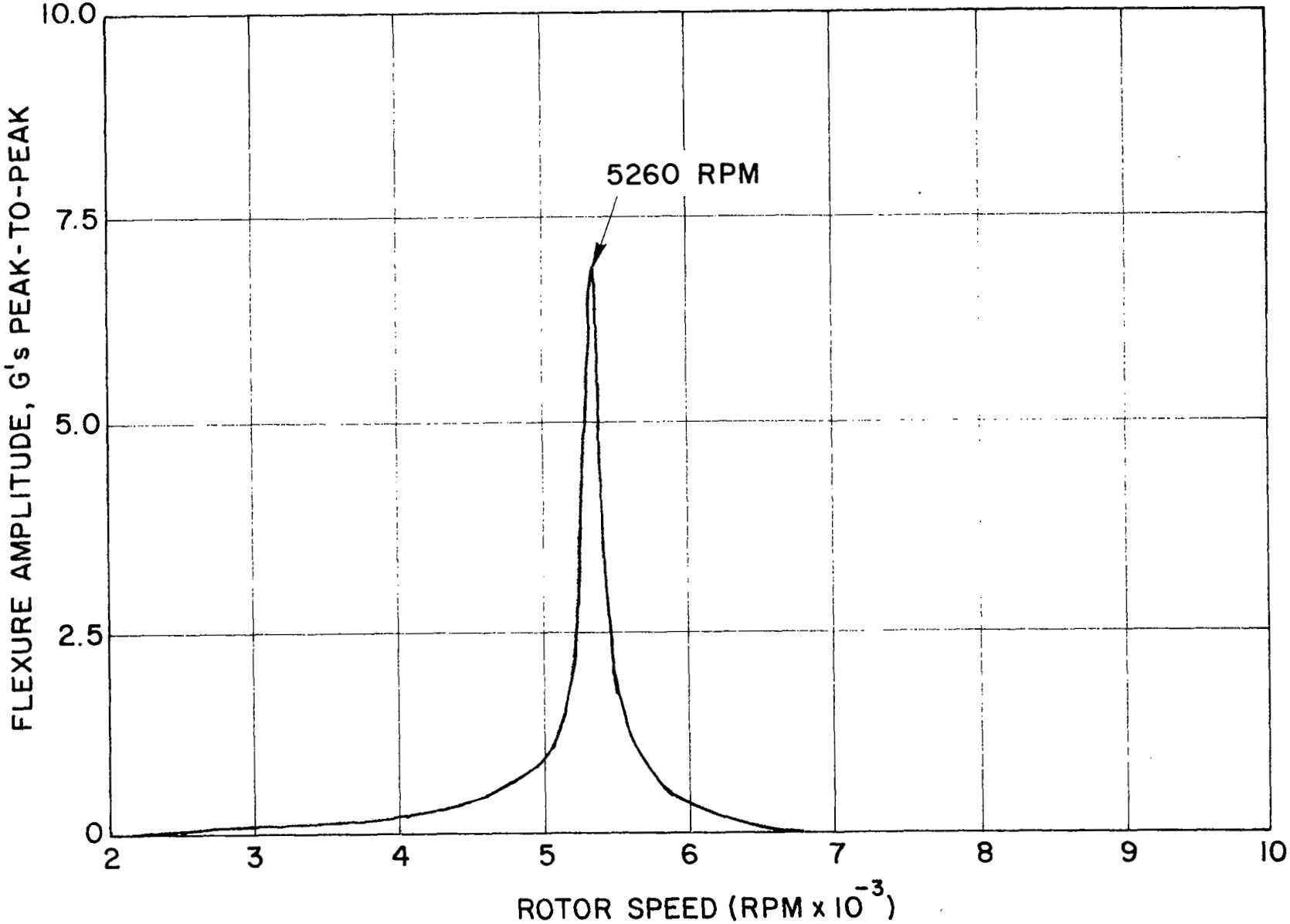

Fig. 21 Vibration Response of Mid-Plane Flexible Probe Holder During the Initial Running with a Distributed Unbalanced Rotor

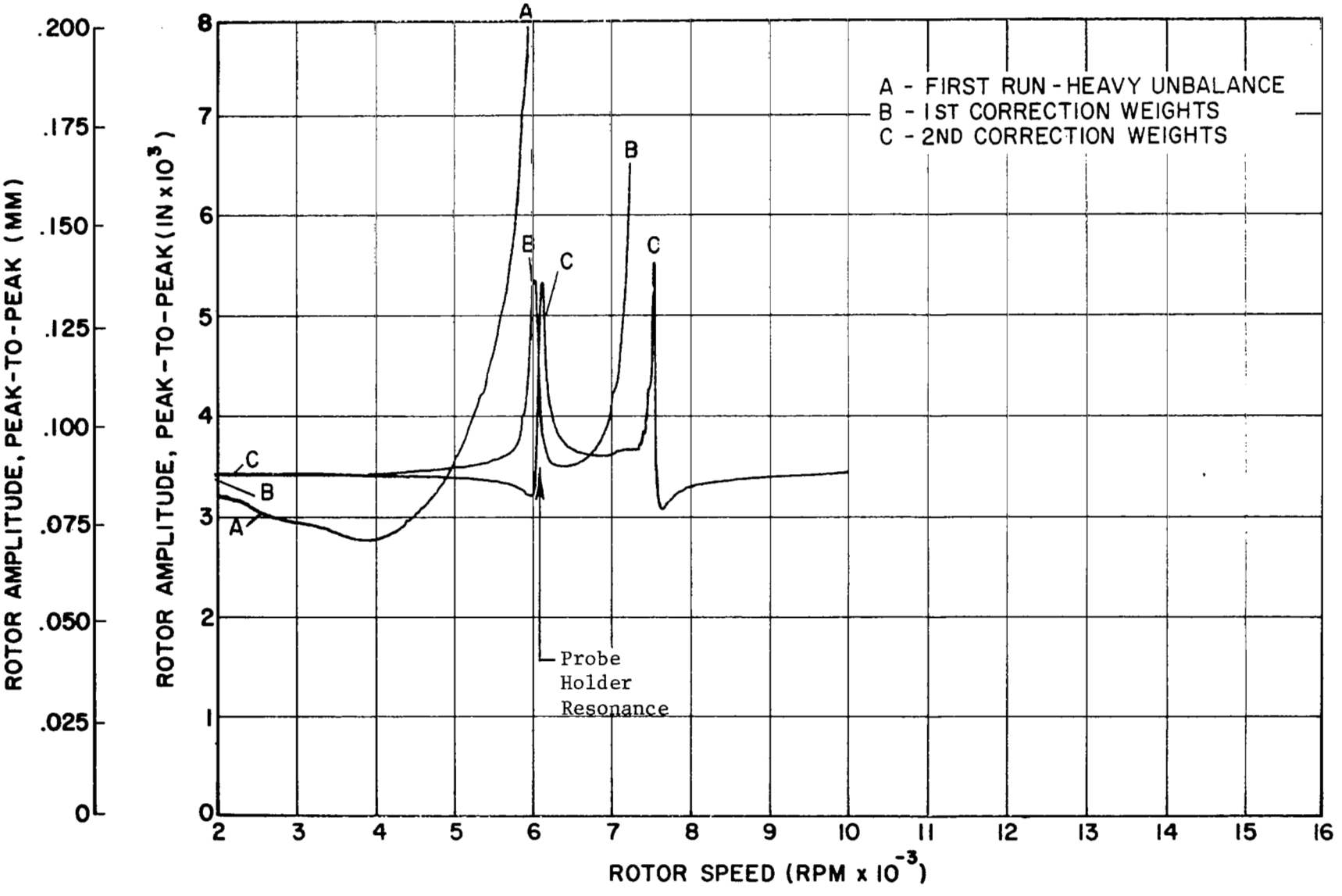

Fig. 22 Vertical Response at the Free End Disk with the Probe Mounted in a Flexible Bracket.

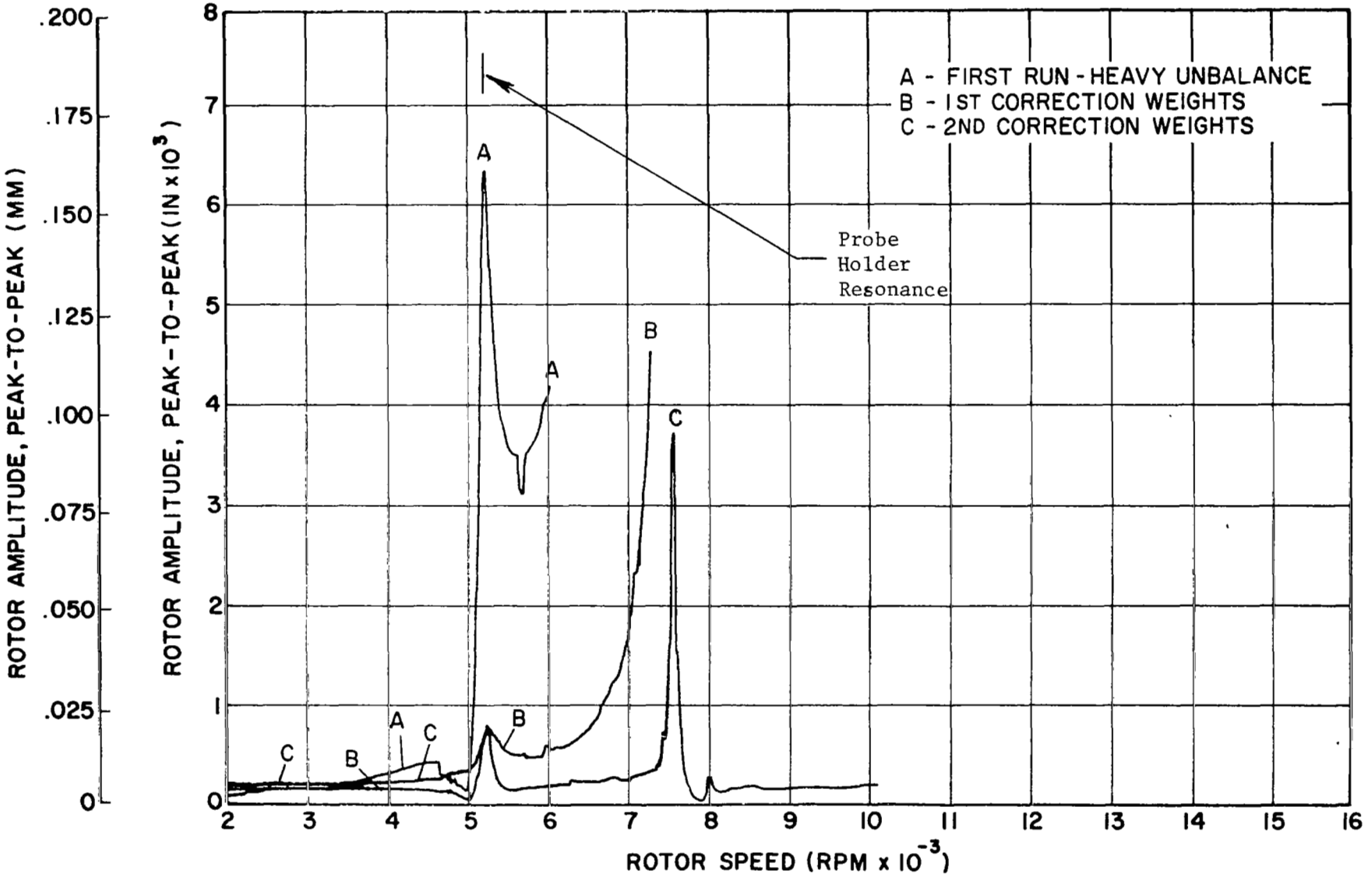

Fig. 23 Vertical Response at the Center Disk with the Probe Mounted in a Flexible Bracket.

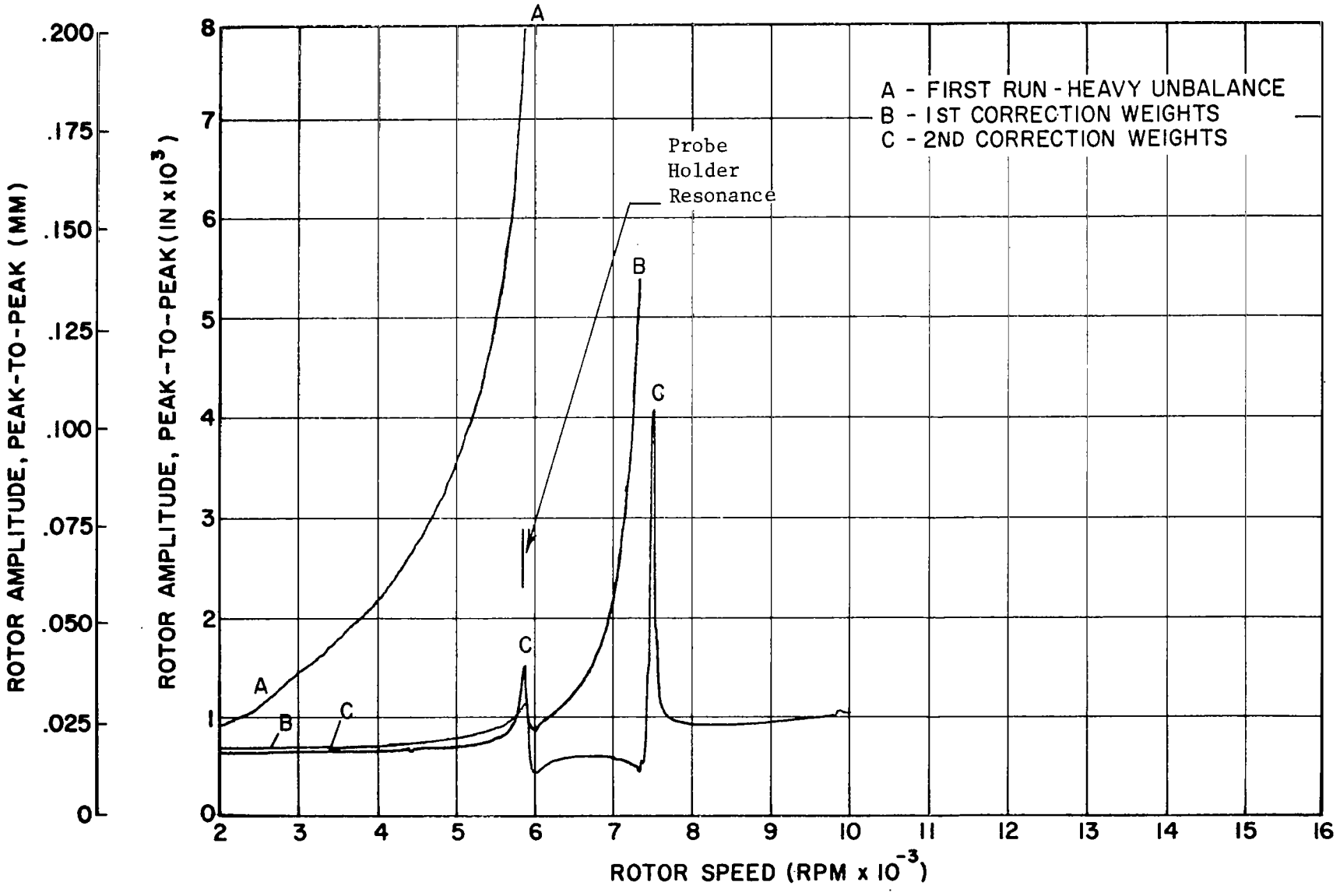

Fig. 24 Vertical Response at the Motor End Disk with the Probe Mounted in a Flexible Bracket.

during the initial acceleration and can still be identified from all successive amplitude curves obtained after balancing.

To stay within the linear range of the displacement instrumentation, a balancing speed of 5150 rpm, which is less than 70 percent of the rotor critical speed, was selected. It was anticipated that the rotor might be too far removed from its natural frequency to obtain meaningful influence coefficients for the first mode shape. A combination of data from the three flexibly mounted probes and one hard mounted probe were used for this experiment. These probes were all vertical. As a reference, vibration data was also taken on a second set of four probes which were hard mounted displacement sensors in the horizontal plane. Each set of probe data was used independently to provide an analytical comparison of hard mounted versus flexibly mounted probes.

With application of the first set of correction weights to the rotor, bearing housing vibrations were reduced, thereby reducing the excursion of the flexible probe holders. Curves B of Figures 22 through 24 show the relative rotor response through the flexible probe holder natural frequencies up to the first rotor critical speed. Curve B still represents composite values of flexure vibrations and rotor amplitudes, but it appears that Curve B predominantly reflects rotor vibrations except for the narrow speed regimes around the individual probe holder resonances. Since amplitudes above 7400 rpm were judged too large for either safe rotor operation or linear instrumentation range, the balancing process was repeated. The second set of correction weights, based on the 7400 rpm balancing speed, was installed, and the rotor was able to accelerate through the critical speed as shown in the response Curves C of Figures 22 through 24.

A visual comparison of the responses from flexibly mounted probes and hard mounted probes in the same plane showed that probe holder vibration contributes significantly to the observed overall vibration signal. As measured by accelerometers mounted next to the probe, the vibration signal was not limited to just the integral rotor frequency, but contained higher order frequencies as well. Figure 25 shows a comparison of the hard mounted horizontal probe and the resonant probe for the midplane disk. Note that the frequency content varies with speed. At 7150 rpm, (Figure 25a), the nonsynchronous components caused by the resonant probe holder were a major contributor to the overall

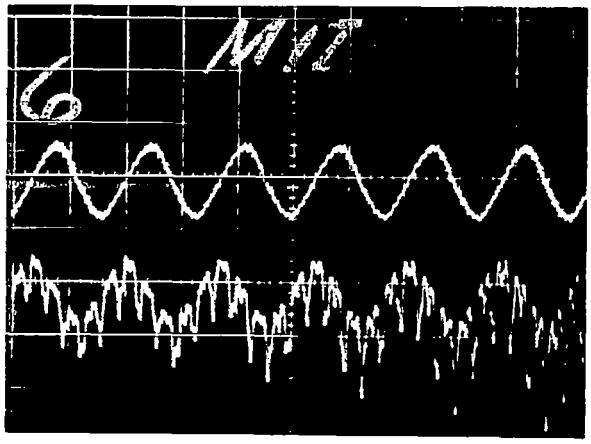

Horizontal Probe (Hard)

Vertical Probe (Resonant)

One Major Vertical Division Equals
Approximately 0.025 mm

One Major Horizontal Division Equals
Approximately 5 Milliseconds

Fig. 25a. Vibration Signal Recorded on the Mid-Plane Disk at 7150 RPM

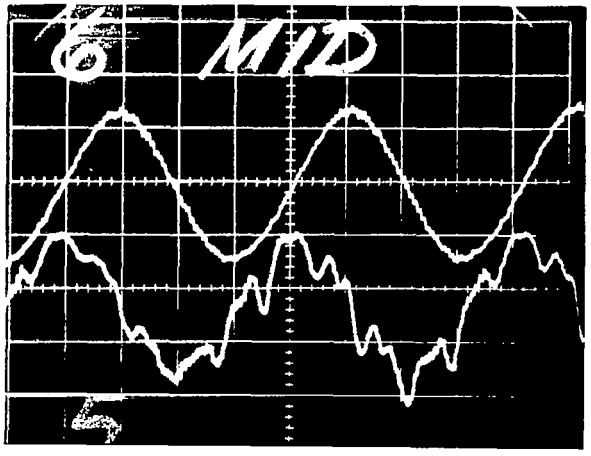

Horizontal Probe (Hard)

Vertical Probe (Resonant)

One Major Vertical Division Equals
Approximately 0.025 mm

One Major Horizontal Division Equals
Approximately 2 Milliseconds

Fig. 25b. Vibration Signal Recorded on the Mid-Plane Disk at 7400 RPM

signal; whereas, the speed trace at 7400 rpm shows very little participation of higher frequencies. In Figure 26, several successive orbits were superimposed to show the effect of this high frequency response on the vibration as measured from the free end disk's vertical resonant probe and hard mounted horizontal probe.

The instrumentation used for balancing successfully separates the nonsynchronous vibration from the synchronous vibration component which is needed for the balancing process. This had been well known in the past. The new and significant finding from these experiments is the ability of the multiplane-multispeed balancing method to reduce unbalance in the rotor even when large, extraneously generated, synchronous vibrations have been added to the signals used for balancing. However, it must be remembered that these extraneous signals, which originate from the probe holders, are caused by unbalance-induced shaft vibration and, thus, are a direct function of it.

Trial Weight Placement

After the resonant probe tests had been completed, the rigid vertical probes were reinstalled and all the unbalance and correction weights were removed from the rotor in preparation for the trial weight placement tests. The "as is" rotor was then accelerated to a maximum speed of 7500 rpm before exceeding the vibration limits and, therefore, was not able to traverse the critical speed. Influence coefficient data was taken at 7400 rpm using trial weights placed at 0 and 180 degree locations on the three balancing planes: the free end, center plane, and motor end disks. The calculated correction weights were applied to the rotor which then successfully passed through the critical speed. All weights were removed to return to the "as is" condition again. The identical trial weights were now placed at the zero degree location only and influence coefficient data was again taken at 7400 rpm. When the calculated correction weights from this set of influence coefficients were positioned on the balancing planes, the rotor was again able to go through the critical speed; however, this time, the vibration levels were somewhat higher. Figure 27 shows the typical vertical response of the rotor for the "as is" condition (Curve A); the 0 and 180 degree trial weight placements (Curve B); and the zero degree only trial weights (Curve C).

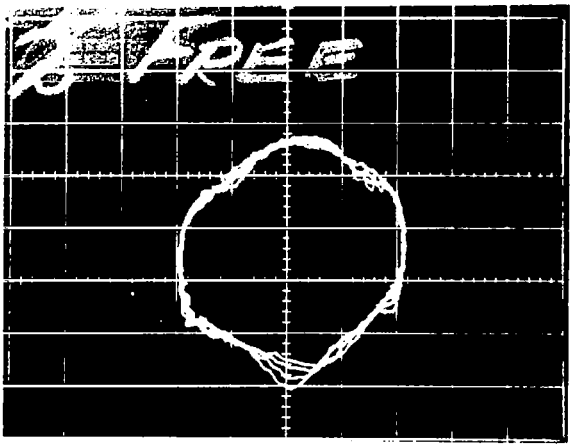

One Major Division Equals
Approximately 0.025 mm

Fig. 26 Vibration Orbit Signal as Recorded From a Resonant Vertical Probe and Hard Mounted Horizontal Probe on the Free End Disk at 7130 RPM

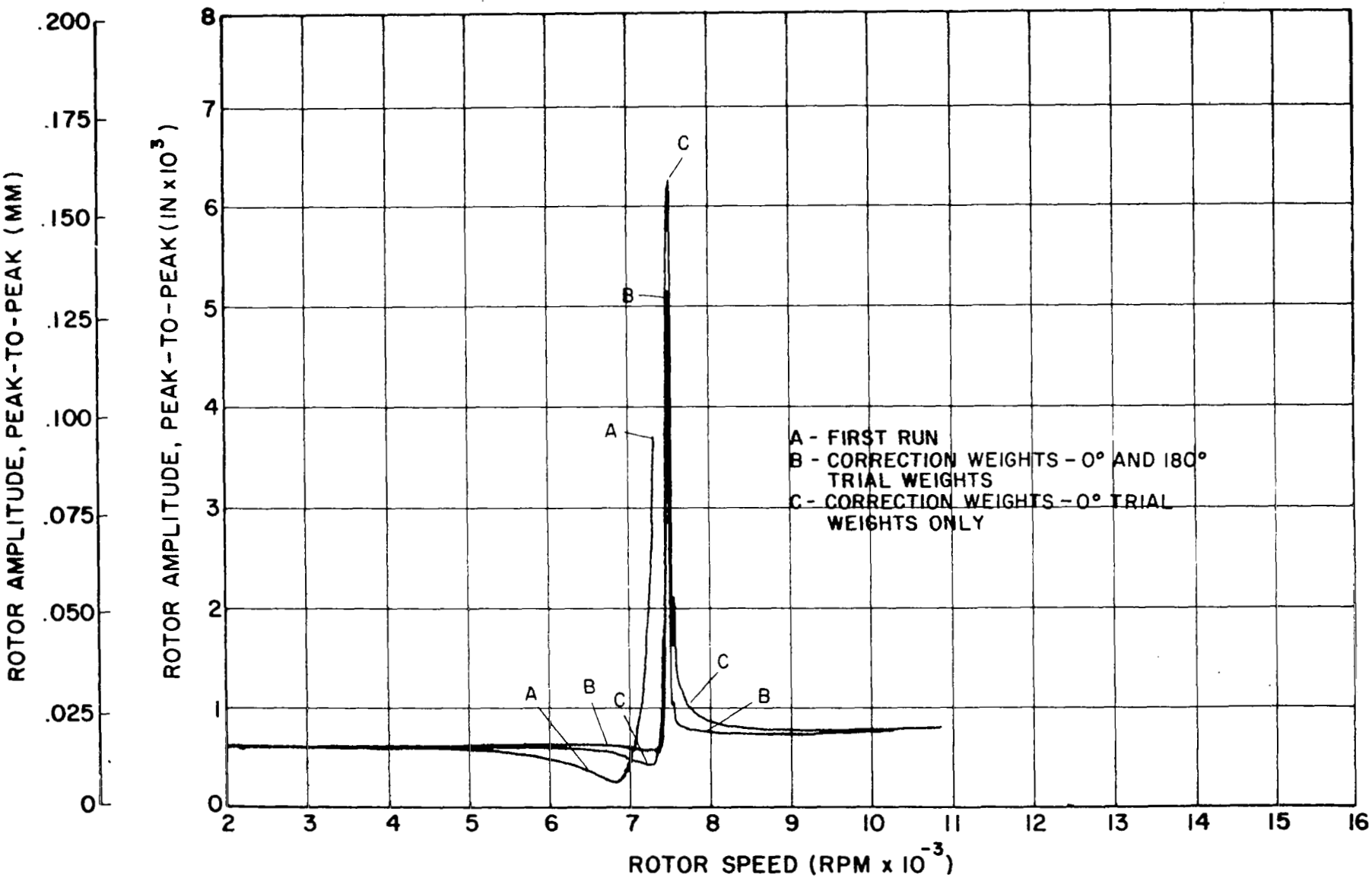

Fig. 27 Vertical Response at the Motor End Disk

Since the influence coefficients from the zero degree trial weight placements seemed to be less accurate in balancing the rotor, the question arises as to whether they could be used for a trim balancing operation. Vibration data was recorded at 7400 rpm and new additional correction trim weights were determined based on the previously determined single trial weight placement influence coefficients. The typical results from this test are shown in Figure 28. The resultant trim balanced vibration amplitude was extremely low, showing the capability for trim balancing even if the first balance attempt was not as accurate as could be obtained with 0 and 180 degree trial weight placements.

The rotor unbalance distribution was changed slightly and the test was repeated to verify the initial findings. For both the single and dual trial weight placement balancing attempts, the rotor was able to traverse the critical speed, but, again, results from the single trial weight placement showed higher vibration. The rotor-bearing system is probably nonlinear because of the effects of journal bearing damping as a function of rotor vibration displacement. This nonlinear effect is handled better by two trial weight placements, since the influence coefficients from both increases and decreases in vibration (normal result from 0 and 180 degree trial weights) are averaged for use in determining correction weights.

This means that, in general, averaged influence coefficients will yield more consistently accurate correction weights because they average any potential error created by nonlinear effects. However, this does not mean that the single trial weight placement is not satisfactory or even that, at times, it will not give a better result. If the single trial weight placement happens to be 180 degrees opposite the unbalance producing the vibration level, then these influence coefficients will, in fact, probably be more accurate than for the two trial weight method. In the final tests, the rotor response characteristics were modified again and results with the single trial weight placement were actually better than with the two weights. Figure 29 shows the typical rotor response for this test.

Filter Bandwidth Variations

The final balancing experiments were conducted with various tracking filter bandwidths. In separate tests, 10 Hz, 25 Hz, and 50 Hz bandwidth filters were

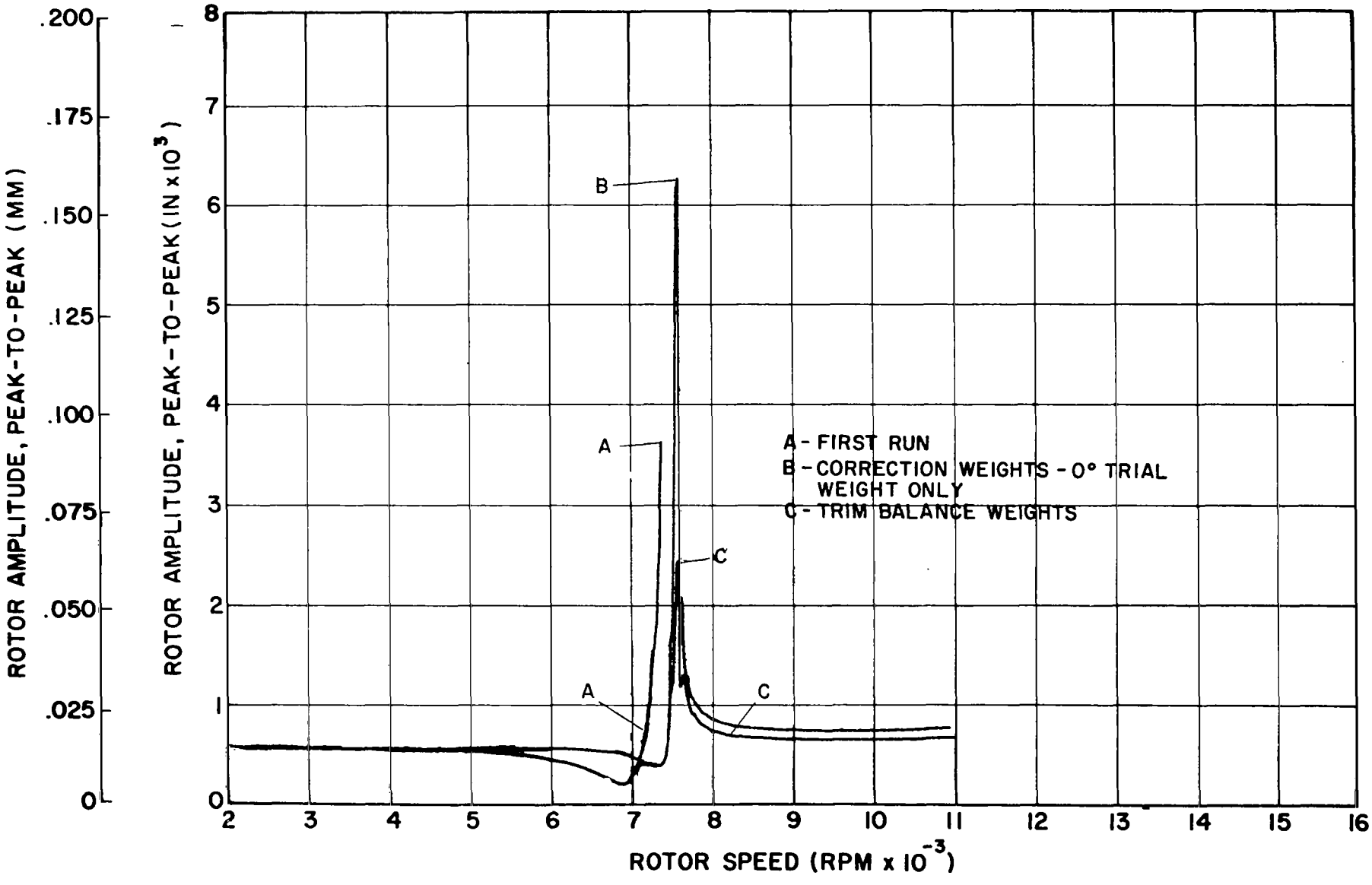

Fig. 28 Vertical Response at the Motor End Disk

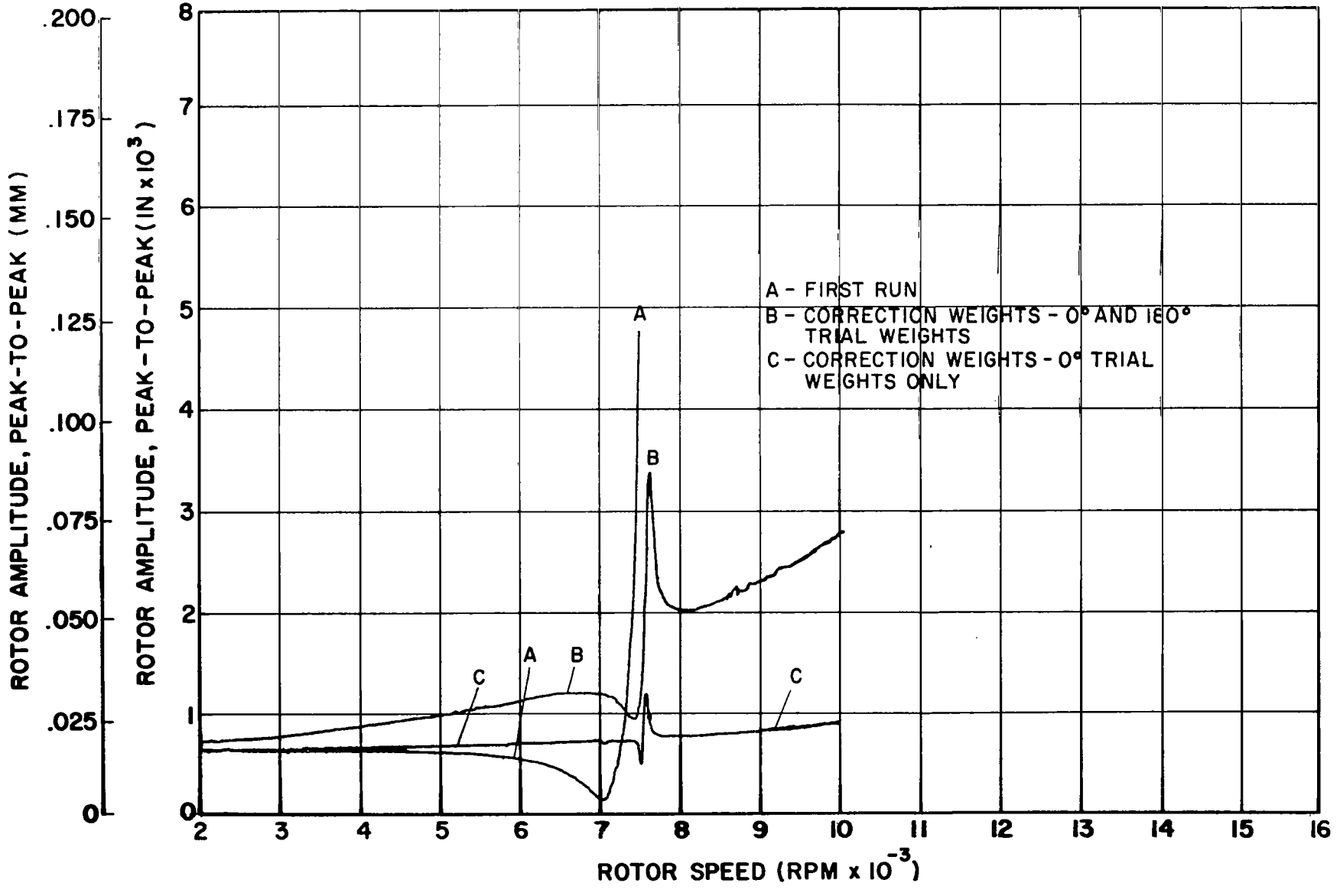

Fig. 29 Vertical Response at the Motor End Disk

used to eliminate vibration data whose frequency was somewhat different than the discrete rotational speed. When the bandwidth becomes large, more non-synchronous vibration remains within the filtered signal and the total signal amplitude increases. Two trial weight placements at 0 and 180 degree on each of the three balancing planes were used for each filter width. The resultant correction weights were applied to the rotor, and the typical response (center disk) is shown for each filter width in Figure 30. The raw data would indicate that the 50 Hz filter, which allows the most amount of nonsynchronous vibration to be used as data, gave the best results. It should be noted though that, since the rotor is highly undamped, small changes in acceleration rate could have produced these variations in amplitude. The important fact is that we could successfully traverse the critical speed for all three bandwidth filters.

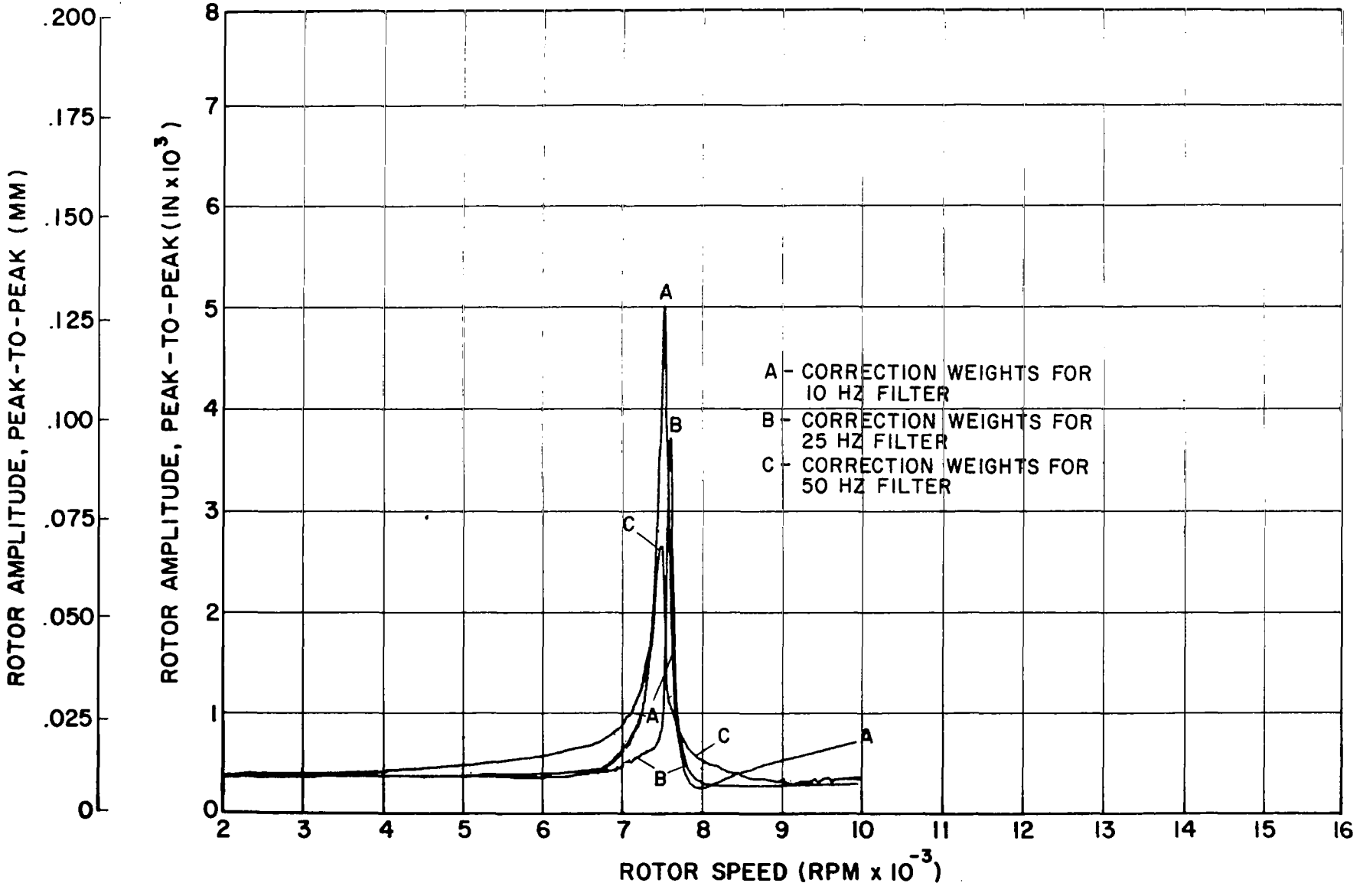

Fig. 30 Vertical Response at the Center Disk

GUIDELINES AND CRITERIA FOR LOCATION OF PLANES AND SENSORS

Engineering for the use of multiplane balancing requires that locations be selected for balance planes and sensors (probes). Arbitrary selection of balancing plane or probe locations cannot be expected to yield optimum balancing efficiency. As a formalized aid in selecting optimum balancing planes and sensitive probe locations, an analysis has been developed and is shown in Appendix A. In this analysis, the effectiveness of a particular balance plane configuration is quantified in terms of a penalty which may be calculated from a particular rotor as a function of the plane locations. In addition, a function which can be used to measure the sensitivity of a particular arrangement of displacement sensors is suggested in Appendix A.

The penalty function (which should be minimized) is based on the amount of weight which would have to be added or removed to balance out a unit unbalance distribution for each mode of vibration which is of concern. Two examples of the use of this penalty function for a uniform rotor are provided in a later section of this report.

The derivation of the probe location sensitivity function is more intuitive than the function developed for balance plane locations; but, recognizing this shortcoming, it can be effectively applied.

Both functions provide guidance to the designer who is faced with the problem of selecting locations for planes and sensors for multiplane balancing. They formalize a process which must otherwise be based on intuition. In this section of the report, the use of these functions to measure the "quality" of plane and probe locations is described and related to the overall process of designing for multiplane balancing.

Figure 31 is a flow chart illustrating an ideal sequence to follow in the selection of locations for balance planes and probes.

The starting point for this sequence is the set of drawings of the rotor, its bearings, and the bearing support structure. Based on these drawings, several actions are taken: a dynamic model of the rotor is prepared which can be

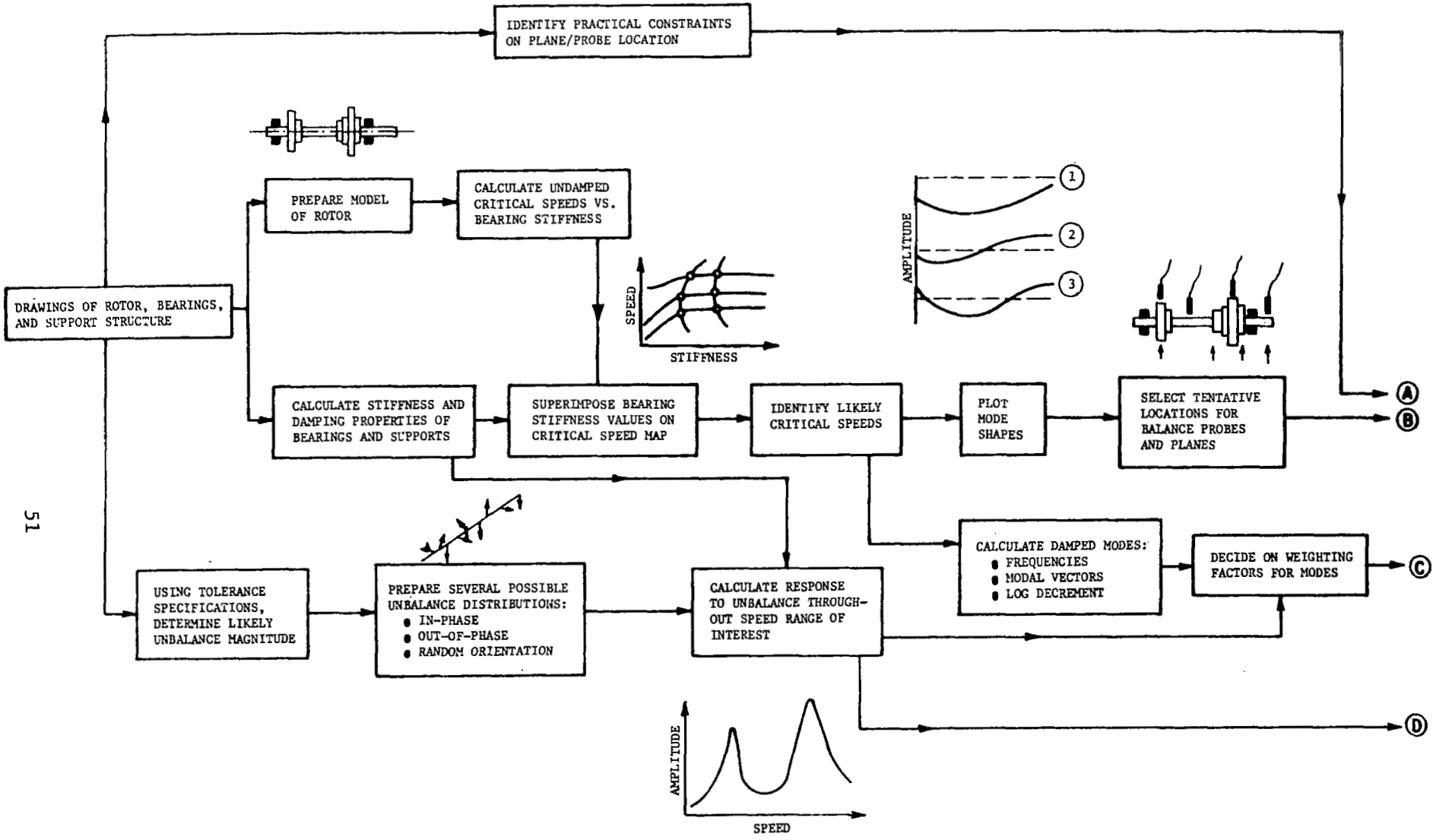

Fig. 31 Multiplane Balancing Procedure for Selection of Planes and Probes

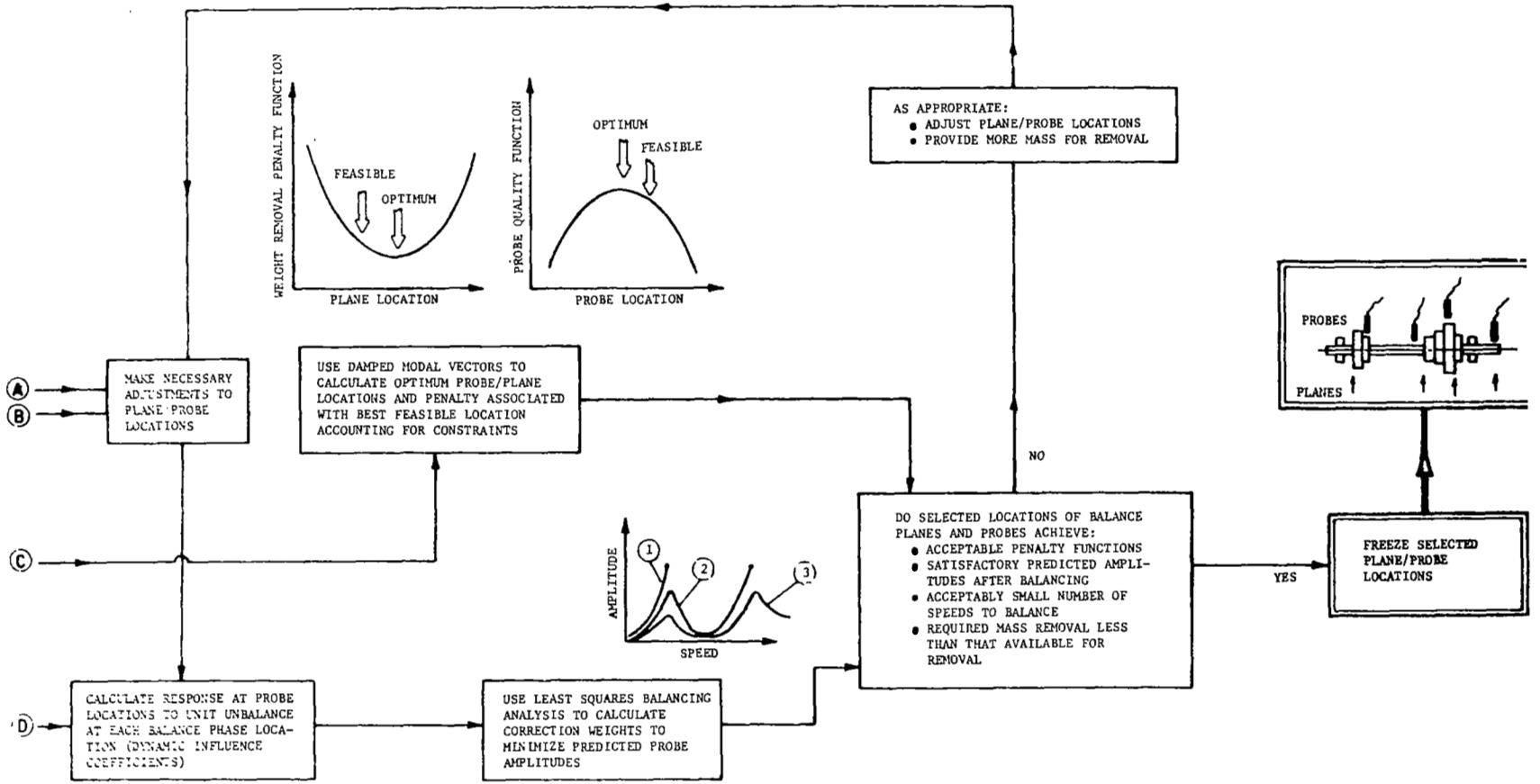

Fig. 31 (Sheet 2)

analyzed by available tools for critical speed, damped natural frequency, and unbalance response prediction; the bearings and their support structure are analyzed to determine the stiffness and damping associated with the rotor suspension and the variation of stiffness and damping with speed; the manufacturing and assembly tolerances are analyzed to determine the amount by which the rotor center of gravity may be offset from the center of rotation at various points along the rotor; the associated unbalance magnitude is calculated; and the constraints which may impose themselves upon selection of balance plane and probe locations are identified.

Once a good theoretical model of the rotor is established, it is first used to make undamped critical speed predictions. Critical speeds should be calculated over a wide range of bearing stiffnesses, including the likely range of stiffness values. As a minimum, the speed range investigated for critical speeds should go beyond the likely operating speed ranges. The critical speed information is conveniently presented as a map on which variation of critical speed with stiffness is plotted. The variation of bearing stiffnesses with speed is superimposed on this map and the points of intersection of bearing stiffness lines with critical speed lines indicate the likely resonant speeds. One complication is that, with unequal stiffnesses in the vertical and horizontal directions, there are two distinct intersections between the bearing stiffness lines and each critical speed line. In this way, two first critical speeds, two second critical speeds, etc., can be identified.

The mode shapes of the rotor for the support stiffness values at the likely resonant speeds should then be plotted. These mode shapes provide the most important single piece of information in guiding the selection of balancing planes and probes. If one balancing plane is provided for each mode that the rotor must pass through, and if the plane associated with each mode is located at, or very close to, the point of maximum amplitude for the mode, then a reasonable set of plane locations is assured. For rotor bearing systems with unequal bearing support stiffnesses, it may be worthwhile at this stage in the design to use the mode shape corresponding to the average stiffness; this shape is unlikely to differ appreciably from the shape at either precise stiffness value.

In this way, tentative or preliminary locations for balance planes can be selected and the preliminary probe location should correspond closely to the selected plane locations. These selections are termed preliminary or tentative, since they must now be adjusted to account for practical consideration of such factors as where probes can be mounted; where there is an uninterrupted probe target of sufficient width; where trial weights can be attached; and where metal can be removed or added to implement the required balancing corrections. It is likely that these constraints will cause some adjustment in the selected locations; the designers should be interested in the influence of these adjustments on the effectiveness of the balancing process.

Evaluation of Plane-Probe Locations Using Modal Analysis

The first evaluation employs modal analysis methods to determine a penalty function (which should be minimized) to be associated with the set of balance planes; Appendix A describes the analysis. In summary, for each major mode of concern a normalized sum of the weights, S_n, to correct a unit modal unbalance is calculated:

$$S_n = \left| \frac{\xi_n^* (Z_p)}{\sqrt{N_n}} \right|_{max} \quad \angle_p \frac{W_{pn}}{U_n} \qquad (2)$$

where $\left| \frac{\xi_n^* (Z_p)}{\sqrt{N_n}} \right|_{max}$ is the maximum normalized amplitude at any plane location of the n^{th} mode's forward whirl vector.

$\frac{W_{pn}}{U_n}$ is the contribution in the p^{th} balance plane to the correction weight distribution required to balance out a unit modal component of unbalance for the n^{th} mode.

Since, to achieve the same state of balance, a poor selection of balance planes will require more weight to be added than a good selection, the objective is to minimize S_n for each mode of concern.

The analysis of Appendix A requires that the number of planes, m, be equal to the number of modes, n. Usually it is convenient to meet this constraint. The conditions under which it may be possible to balance effectively without meeting this constraint and the way the analyses can be used in this case will shortly be discussed. First, however, it is worth discussing the additional steps necessary to implement this analysis.

Essential to the analysis is the determination of the damped modes of vibration of the rotor-bearing system. The required inputs to the calculation are the dynamic rotor model and the stiffness and damping characteristics of the bearings and bearing supports. Given these inputs, the complex eigenvalues of the system are determined, up to and beyond frequencies in the range of interest. A method of determining complex eigenvalues is described in [4]. The complex eigenvalue consists of two quantities, λ_n and ω_n (its real and imaginary parts). ω_n is the damped natural frequency, and λ_n is the growth exponent, from which the log decrement δ_n ($= -2\pi \lambda_n/\omega_n$) can be calculated. δ_n measures the effective system damping for the n^{th} mode and, with δ_n of order 1.5 or above, a negligible contribution to the response is to be expected from that mode.

Associated with each complex eigenvalue is an eigenvector which defines the mode of vibration in terms of four quantities at each station of the rotor. These quantities are the horizontal and vertical in-phase components of displacement and the horizontal and vertical out-of-phase components of displacement. For the present analysis, each eigenvector is broken into a forward circular whirl vector and a backward circular whirl vector, such that the elliptical orbit at any station is the sum of the forward and backward circular whirl components. In addition, the adjoint vector (ξ_n) to the forward whirl vector (ξ_n) is determined. Given these quantities, the calculation of S_n can proceed, with the following qualifications.

If the bearings are not isotropic, there will be two damped natural frequencies associated with each basic vibration mode of the rotor (slight differences will exist between this pair of modes, but the two should not be regarded as distinct modes for balancing purposes — the distribution of planes which is good for one mode of the pair will be good for the other). A choice must be made to select only one of each pair and the best choice is the mode with the

smaller log decrement, since this is likely to contribute more strongly to the rotor response.

Desirably, there should be a balance plane for each distinct mode through and up to which the rotor is required to run smoothly. This situation will normally be the result of the tentative plane selections already made on the basis of the undamped mode slopes. Some possible exceptions are considered as follows:

(a) Number of planes less than the order of the highest mode to be balanced through.

In general, a rotor can be balanced through the highest order critical speed with fewer planes than the highest order only if some of the intermediate modes are well-damped and, thereby, show acceptable resonant amplitudes without balancing. The degree of damping of each mode can be judged from its log decrement, δ_n, and, as a rule of thumb, the plane associated with a particular mode may be dropped only if the log decrement for that mode exceeds 1.5.

To implement the analysis in this case the heavily damped modes whose influence is being neglected must be dropped entirely from the analysis so that the number of modes actually considered still matches the number of planes.

(b) Number of planes greater than the order of the highest mode whose influence is to be balanced.

In this case, there are planes which are redundant. However, the mechanics of the analysis can be implemented, provided that the number and order of modes considered in the analysis are increased to match the number of planes. In this case, the penalty functions associated with the higher modes, which are introduced to make the analysis work, need not influence the plane selection.

(c) Number of planes equals the number of modes whose influence is to be balanced out but some of the modes are much less important (heavily damped) than others.

If this situation exists, the penalty functions associated with the well-damped modes should be given reduced weighting in selection of

the plane locations. As shown in the Appendix, a magnification factor can be identified as a function of the log decrement.

$$Q_n = \frac{\pi}{\delta}\left[1 + \left(\frac{\delta}{2\pi}\right)^2\right] \tag{3}$$

This factor may be conveniently used as the weighting factor. One way of using this function is to generate an average weighted sum, $\overline{S}$, of the normalized correction weights for a plane configuration:

$$\overline{S} = \frac{\sum_n Q_n S_n}{\sum_n Q_n} \tag{4}$$

The quantity, $\overline{S}$, represents a single theoretical measure of the balance plane location quality. $\overline{S}$ has a minimum possible value of 1 although, for a particular probe and number of modes of concern, the minimum value may be greater than 1. The combination of balance plane locations which minimizes $\overline{S}$ may be considered as the optimum. The use of $\overline{S}$ offers convenience as a single measure of plane location quality but must be used with great care and never without considering the individual functions S_n for each individual mode of importance.

Experience must be established before firm rules for acceptable values of S_n and $\overline{S}$ are established. In Reference 3, extensive demonstrations of successful balancing of a flexible rotor through four critical speeds were presented. Application of these balance plane location criteria for this rotor showed that S_1, S_2, S_3, and S_4 were 17, 11, 2, and 26 percent higher than the minimum, respectively. The success of this configuration suggests that such deviations are acceptable.

An evaluation of the probe locations is possible in terms of P_n (a quantity to be maximized) where:

$$P_n = \sum_m \left| \frac{\xi_n(Z_m)}{\sqrt{N_n}} \right| \tag{5}$$

n is the mode number, and

$\frac{\xi_n (Z_m)}{\sqrt{N_n}}$ is the normalized amplitude, at the m^{th} probe, of the forward circular whirl modal vector for the n^{th} mode. In words, P_n measures the average sensitivity of the measurement system to amplitudes of the n^{th} mode. Note that its use does not impose a requirement that the number of probes match the number of modes considered.

Evaluation of Plane-Probe Locations Using Balancing Simulation

A complementary evaluation of the complete plane-probe combination can be performed by means of a simulated balancing sequence. As a starting point, one or more unbalance distributions should be selected on the basis of the likely unbalance magnitudes previously determined from manufacturing and assembly tolerances. Using values of bearing stiffness and damping which vary appropriately with speed, the response of the rotor-bearing system to the selected unbalance at a range of speeds of interest is calculated using a flexible rotor unbalance response analysis. Unless a very low level of unbalance has been selected, the rotor will be unable to pass through the first significant critical speed without exceeding limits imposed by one or more of bearings, seals, dampers, wheel tip clearances, probe clearances and, at high order critical speeds, shaft stresses.

At a speed where the first criterion starts to approach its limit (say within 25 percent), the influence on amplitude and phase angle, at each probe, of a unit unbalance at each balance plane, should be calculated (using the rotor unbalance response analysis). This set of calculations provides influence coefficients for that speed. Using the least squares balancing method, the required correction weights in the balance planes to minimize amplitudes at the probes are calculated. These correction weights are applied and the response to the resultant unbalance distribution as a function of speed is recalculated. The rotor is now likely to traverse the first critical speed without exceeding any of the limits. If not, the procedure must be repeated at a speed closer to the first critical speed while still satisfying these limits. When the rotor can traverse the first critical speed, the procedure is again repeated at the next critical speed of significance. In this way, if an adequate array

of balance planes has been provided, the rotor can be balanced through all critical speeds in the operating range.

This analytical sequence provides a check on the selection of balance planes. However, without modification, it does not truly provide a check on the selection of probe locations. The influence coefficients and response amplitudes can be calculated to high accuracy whereas the required measurements are limited, in practice, by the probe sensitivity. For a given electronic probe resolution, effective probe sensitivity can be influenced by probe location relative to the node and antinode locations on the rotor. Near antinodes, where amplitude changes are larger, better probe sensitivity can be obtained. To provide a check on probe locations, it would be necessary to simulate a given probe sensitivity by limiting the precision within which the response amplitudes are calculated so that errors in the influence coefficients and level of unbalance response amplitude are induced. If the calculation precision is made to correspond to the probe resolution, the error will be consistent in magnitude with the errors introduced in taking actual measurements in a balancing sequence.

Since this balancing simulation procedure is more unwieldy than the optimization using the criteria S_n, $\overline{S}$, and P_n, it should be used as a check rather than as part of the optimization loop.

Table 3 summarizes the information provided by the evaluations described above.

Table 3

SUMMARY OF INFORMATION OBTAINED DURING SELECTION OF BALANCE PLANES AND PROBES

Analysis Used	Information Provided
Undamped Critical Speeds	• Reasonable Selection of Planes and Probes based on Mode Shapes
Damped Natural Frequencies	• Identification of Unimportant Modes • Quantified Optimization Criteria for Probe and Plane Selection
Unbalance Response and Least Squares Balancing	• Checks on Plane Selection

As shown, the undamped critical mode shapes and the practical constraints imposed by the rotor configuration can be used to make a reasonable selection of balance plane and probe locations, if it is ensured that the maximum amplitude for each mode is closely covered by a probe; that a distinct balance plane exists for each mode; and that the location of the plane associated with each mode is near the location of maximum amplitude for that mode. The criteria based on damped modes provide two valuable extensions to the undamped analysis: first, the unimportant modes are identified by the existence of a large log decrement (above 1.5); and second, these numerical criteria allow a value to be placed on any set of probe or plane locations and show the change in this value with varying locations.

Balancing simulation using unbalance response predictions and a least squares balancing procedure is a valuable check which adds credibility to the selection of balance plane and probe locations.

In the following report section, numerical examples are presented of the evaluation procedures which use damped modes. Examples of the balancing simulation procedure are not presented, but a full demonstration of the procedure may be found in Reference 12.

In this section, use of the criteria developed in Appendix A and discussed in the previous section is demonstrated. In the first example, the criteria are used to predict optimum balance plane and probe locations for a uniform flexible shaft on rigid supports; and in the second, a uniform flexible shaft on flexible damped bearings is considered.

Uniform Shaft on Rigid Supports

When the rotor system is free of damping and gyroscopic moments can be ignored, the analysis of Appendix A can be simplified considerably. The eigenvalues become purely imaginary (pure frequencies) and the mode shapes become planar (real). Also, the adjoint functions are identical to the modal functions, and Equation (A-47) reduces to:

$$\xi = \sum_n \frac{\Omega^2}{\omega_n^2 - \Omega^2} \frac{\xi_n}{\sqrt{N_n}} U_n \tag{6}$$

Furthermore, when the supports are isotropic, the whirl orbits are circular such that ξ becomes real.

To illustrate, a uniform shaft, supported in rigid bearings at the ends, is considered. This is equivalent to the classical simply supported beam for which the resonant frequencies and mode shapes are given by (Reference 1).

$$\omega_n = n^2 \pi^2 \sqrt{\frac{EI}{\ell^3 M}} \tag{7}$$

and,

$$\frac{\xi_n}{\sqrt{N_n}} = \sqrt{\frac{2}{M}} \cdot \sin\left(n\pi \frac{Z}{\ell}\right) \tag{8}$$

where $M = \mu\ell$ is the total mass of the shaft, and ℓ is the length.

Balance Plane Location - Three Mode Balancing

If the rotor is to be balanced for three critical speeds, it will be assumed that one correction plane, Plane No. 2, is in the middle ($\frac{Z_2}{\ell} = \frac{1}{2}$); while the other two planes, Plane Nos. 1 and 3, are symmetrically located around the middle:

$$\frac{Z_3}{\ell} = 1 - \frac{Z_1}{\ell} \tag{9}$$

Setting $\zeta_1 = \frac{Z_1}{\ell}$, Equation (A-54) yields:

$$\sqrt{\frac{2}{M}} \begin{Bmatrix} \sin(\pi\zeta_1) & 1 & \sin(\pi\zeta_1) \\ \sin(2\pi\zeta_1) & 0 & -\sin(2\pi\zeta_1) \\ \sin(3\pi\zeta_1) & -1 & \sin(3\pi\zeta_1) \end{Bmatrix} \begin{Bmatrix} \frac{w_{11}}{u_1} & \frac{w_{12}}{u_2} & \frac{w_{13}}{u_3} \\ \frac{w_{21}}{u_1} & \frac{w_{22}}{u_2} & \frac{w_{23}}{u_3} \\ \frac{w_{31}}{u_1} & \frac{w_{32}}{u_2} & \frac{w_{33}}{u_3} \end{Bmatrix} =$$

$$- \begin{Bmatrix} 1 & 0 & 0 \\ 0 & 1 & 0 \\ 0 & 0 & 1 \end{Bmatrix} \tag{10}$$

which is readily solved to give:

$$\begin{Bmatrix} \frac{w_{11}}{u_1} & \frac{w_{12}}{u_2} & \frac{w_{13}}{u_3} \\ \frac{w_{21}}{u_1} & \frac{w_{22}}{u_2} & \frac{w_{23}}{u_3} \\ \frac{w_{31}}{u_1} & \frac{w_{32}}{u_2} & \frac{w_{33}}{u_3} \end{Bmatrix} = \frac{\sqrt{\frac{1}{2}M}}{2\sin(2\pi\zeta_1)\left[\sin(\pi\zeta_1) + \sin(3\pi\zeta_1)\right]}$$

$$\begin{Bmatrix} \sin(2\pi\zeta_1) & (\sin(\pi\zeta_1) + \sin(3\pi\zeta_1)) & \sin(2\pi\zeta_1) \\ 2\sin(2\pi\zeta_1)\sin(3\pi\zeta_1) & 0 & -2\sin(2\pi\zeta_1)\sin(3\pi\zeta_1) \\ \sin(2\pi\zeta_1) & -(\sin(\pi\zeta_1) + \sin(3\pi\zeta_1)) & \sin(2\pi\zeta_1) \end{Bmatrix} \tag{11}$$

As ζ_1 is less than $\frac{1}{2}$, the normalized sum, S_n, of the modal correction weights becomes (Equation A-55):

$$S_1 = \frac{1 + |\sin(3\pi\ \zeta_1)|}{\sin(\pi\ \zeta_1) + \sin(3\pi\ \zeta_1)} \tag{12}$$

$$S_2 = \frac{1}{\sin(2\pi\ \zeta_1)} \tag{13}$$

$$S_3 = \frac{1 + \sin(\pi\ \zeta_1)}{\sin(\pi\ \zeta_1) + \sin(3\pi\ \zeta_1)} \tag{14}$$

The results are plotted in Figure 32 where the abcissa is ζ_1 and the ordinate gives S_1, S_2 and S_3. The optimum plane location is seen to be: $\zeta_1 = 0.25$ while the acceptable range is approximately between 0.1 and 0.3.

The slope discontinuity in the curve for mode 1 arises because of the requirement, in the analysis of Appendix A, that any combination of weights to balance out modal unbalance for the first mode makes no contribution to the second or third modal unbalances.

Reference to the mode shapes for the first three modes (Figure 33) shows, first, that weights added to change the unbalance of mode 1 will be most effective if, for all planes, they are all at the same angular location. Thus, if weights added in planes 1 and 3 were 180° opposed to the weight to be added in plane 2, the required magnitude of the plane 2 weight would be much higher than if all three were at the same angular location.

The second mode shape shows that, whenever the weights in planes 1 and 3 are equal, at the same angular location and equidistant from the shaft center, they will be self-cancelling for mode 2 whatever and wherever the plane 2 weight is.

For the third mode this is not the case; weights at the same angular location in planes 1 and 3 are additive and, if planes 1 and 3 are close to the middle, it is clear that the only way to avoid changing the excitation of the third mode when balancing the first mode is to put the plane 2 weight 180° removed from the 1-3 weight - the situation which was previously identified as calling for

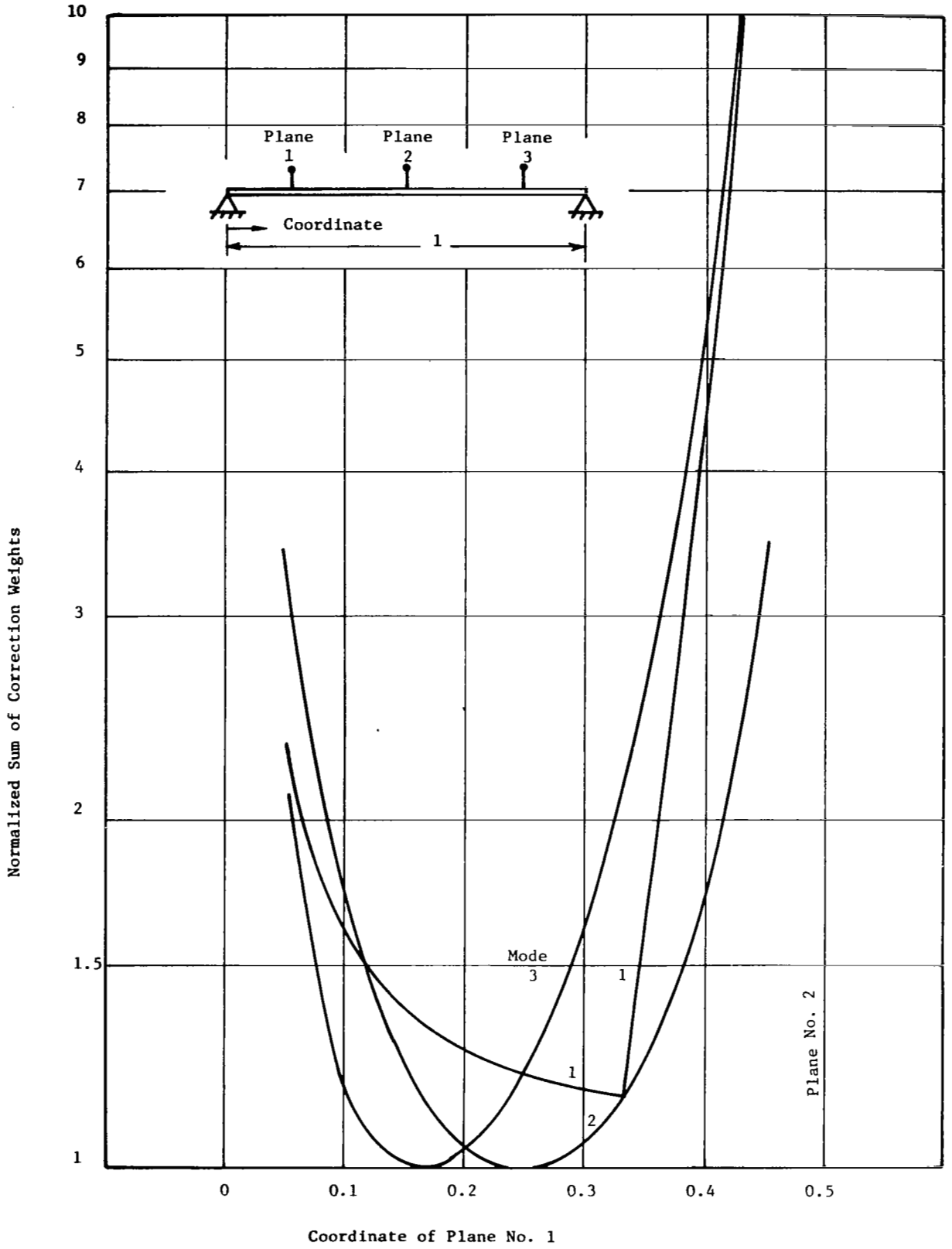

Fig. 32 Influence of Plane 1 on Normalized Sum of Correction Weights for Uniform Shaft on Rigid Bearings and Three Criticals.

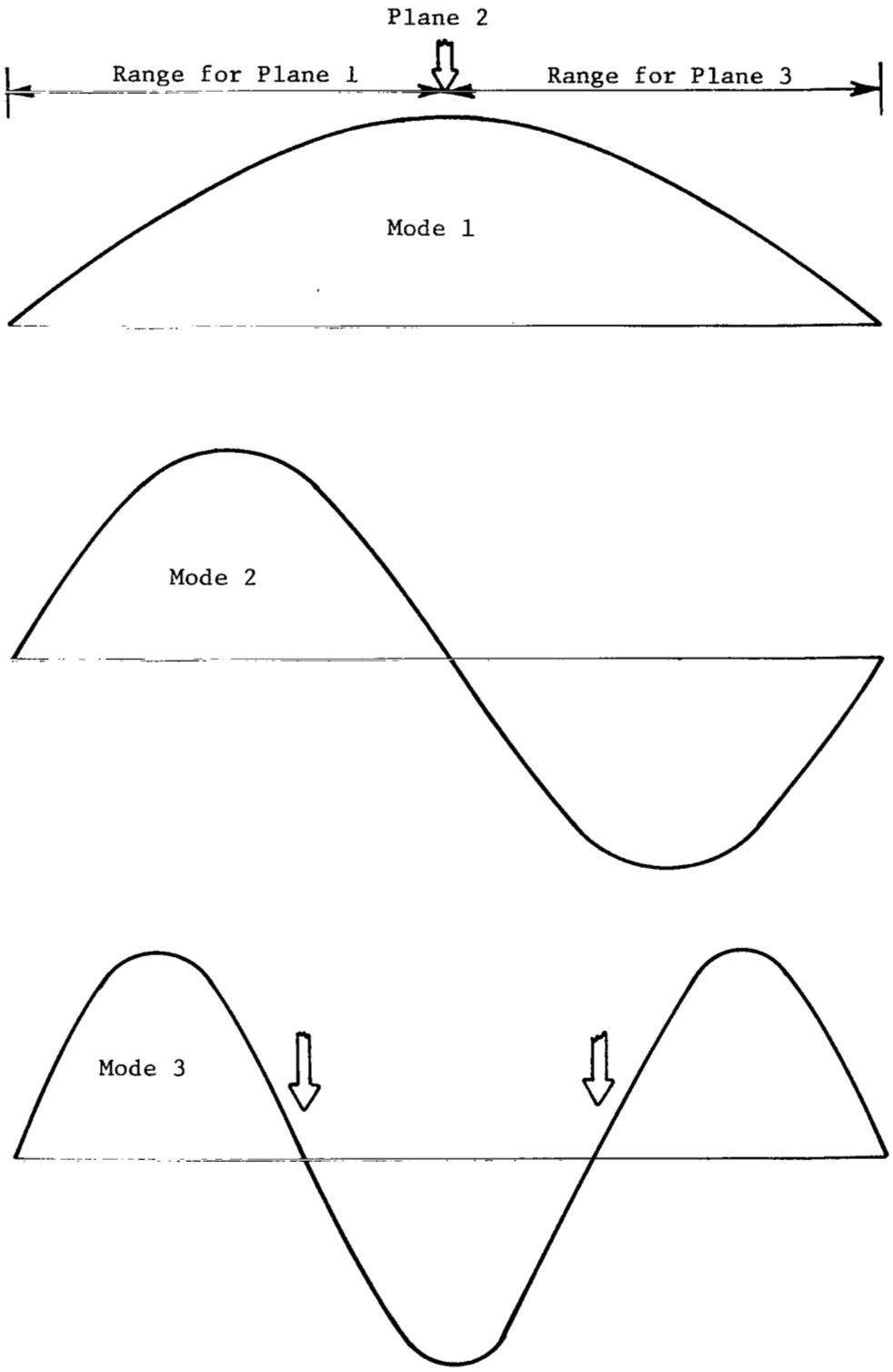

Fig. 33 Mode Shapes For Uniform Shaft In Rigid Supports

a large weight in plane 2. If, alternatively, planes 1 and 3 are close to the ends, the plane 2 correction can be at the same angular location and not excite the third: at the location of planes 1 and 3, one-third of the shaft length from either end (see arrows for mode 3, Figure 33) is the point where mode 3 changes sign and, therefore, where this situation reverses. This change of sign is reflected by the slope discontinuity in the mode 1 plot of Figure 32. This plot says, clearly, that planes 1 and 3 should not be too close to the center of the shaft.

Selection of Probe Locations - Three Mode Balancing

The criterion for evaluating the sensitivity of a particular probe configuration is:

$$P_n = \sum_m \left| \frac{\zeta_n(Z_n)}{\sqrt{N_n}} \right| \tag{15}$$

In applying this to balancing of the first three modes of the uniform shaft in rigid supports, it is assumed that one probe is located at the center of the shaft ($\frac{Z}{\ell} = 0.5$) and that the number of probes equals the number of modes. The two off-center probes are located symmetrically. Thus, P_n is evaluated as a function of the distance of probes 1 and 3 from the ends of the shaft.

Based on equation 15, the following expressions may be written:

$$P_1 \sqrt{\frac{M}{2}} = \left|\sin \frac{\pi}{2}\right| + 2 \left|\sin \frac{\pi Z_1}{\ell}\right| \tag{16}$$

$$P_2 \sqrt{\frac{M}{2}} = \left|\sin \pi\right| + 2 \left|\sin \frac{2\pi Z_1}{\ell}\right| \tag{17}$$

$$P_3 \sqrt{\frac{M}{2}} = \left|\sin \frac{3\pi}{2}\right| + 2 \left|\sin \frac{3\pi Z_1}{\ell}\right| \tag{18}$$

These values for the probe quality functions have been plotted in Figure 34 as a function of $\frac{Z_1}{\ell}$. It may be seen that, to maintain good sensitivity for all three modes, it is necessary to keep probes 1 and 3 in the region of 0.25 times the shaft length from each end. If it were not possible to place these probes exactly at the 0.25 location, it would be preferable to shift them towards the ends of the shaft than towards the center, since the mode 3 sensitivity function falls off sharply as the 1-3 probe location moves further from the end.

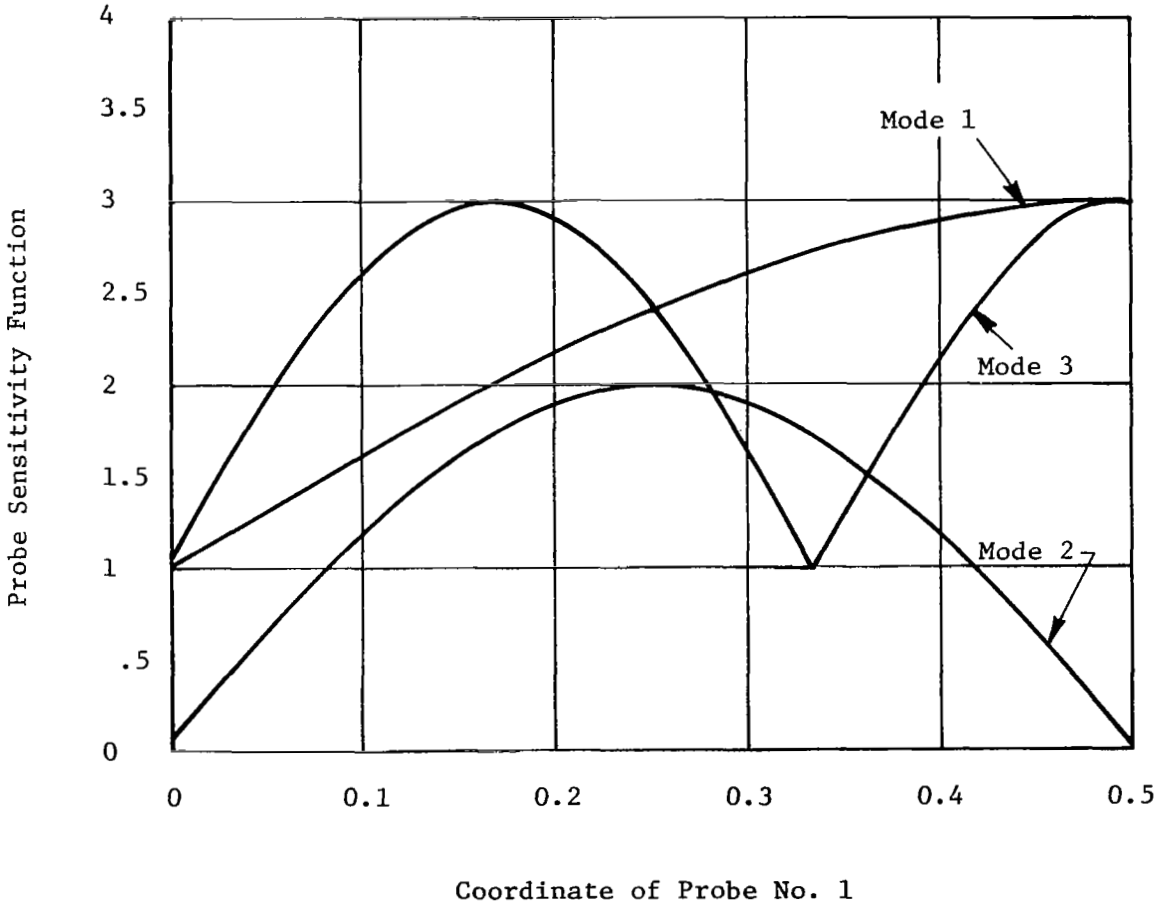

Fig. 34 Effect of Probe 1 and 3 Location on Probe Sensitivity Functions for Uniform Shaft on Rigid Bearings

An interesting result may be inferred from Figure 34 in that a single probe at the center of the shaft gives maximum sensitivity for both modes 1 and 3. Apparently, all three modes could be accurately sensed by a pair of probes, one at the center and one at .25 times the length from one end. As noted previously, it is not a requirement of the probe optimization procedure that the number of probes match the number of modes to be balanced and, in this case, the third probe could be regarded as redundant; its use simply ensures that the balancing procedure has more broadly based information to operate on.

Balance Plane Location - Four Mode Balancing

If the rotor is to be balanced through four critical speeds, it will be assumed that the correction planes are located symmetrically around the middle:

$$\frac{z_3}{\ell} = 1 - \frac{z_2}{\ell} \tag{19}$$

$$\frac{z_4}{\ell} = 1 - \frac{z_1}{\ell} \tag{20}$$

Setting $\zeta_1 = \frac{z_1}{\ell}$ and $\zeta_2 = \frac{z_2}{\ell}$, the resulting modal correction weights can be determined from Equation (A-54) as:

$$\sqrt{\frac{2}{M}} \cdot \frac{w_{11}}{u_1} = \sqrt{\frac{2}{M}} \frac{w_{41}}{u_1} = -\frac{1}{4} \cdot \frac{1 + 2 \cdot \cos(2\pi\,\zeta_2)}{\sin(\pi\,\zeta_1)\,[\cos(2\pi\,\zeta_1) - \cos(2\pi\,\zeta_2)]} \tag{21}$$

$$\sqrt{\frac{2}{M}} \frac{w_{21}}{u_1} = \sqrt{\frac{2}{M}} \frac{w_{31}}{u_1} = \frac{1}{4} \frac{1 + 2 \cdot \cos(2\pi\,\zeta_1)}{\sin(\pi\,\zeta_2)\,[\cos(2\pi\,\zeta_1) - \cos(2\pi\,\zeta_2)]} \tag{22}$$

$$\sqrt{\frac{2}{M}} \frac{w_{12}}{u_2} = -\sqrt{\frac{2}{M}} \frac{w_{42}}{u_2} = -\frac{1}{2} \frac{\cos(2\pi\,\zeta_2)}{\sin(2\pi\,\zeta_1)\,[\cos(2\pi\,\zeta_1) - \cos(2\pi\,\zeta_2)]} \tag{23}$$

$$\sqrt{\frac{2}{M}} \frac{w_{22}}{u_2} = -\sqrt{\frac{2}{M}} \frac{w_{32}}{u_2} = \frac{1}{2} \frac{\cos(2\pi\,\zeta_1)}{\sin(2\pi\,\zeta_2)\,[\cos(2\pi\,\zeta_1) - \cos(2\pi\,\zeta_2)]} \tag{24}$$

$$\sqrt{\frac{2}{M}}\ \frac{w_{13}}{u_3} = \sqrt{\frac{2}{M}}\ \frac{w_{43}}{u_3} = \frac{1}{4}\ \frac{1}{\sin(\pi\ \zeta_1)\ [\cos(2\pi\ \zeta_1) - \cos(2\pi\ \zeta_2)]} \tag{25}$$

$$\sqrt{\frac{2}{M}}\ \frac{w_{23}}{u_3} = \sqrt{\frac{2}{M}}\ \frac{w_{33}}{u_3} = -\frac{1}{4}\ \frac{1}{\sin(\pi\ \zeta_2)\ [\cos(2\pi\ \zeta_1) - \cos(2\pi\ \zeta_2)]} \tag{26}$$

$$\sqrt{\frac{2}{M}}\ \frac{w_{14}}{u_4} = -\sqrt{\frac{2}{M}}\ \frac{w_{44}}{u_4} = \frac{1}{4}\ \frac{1}{\sin(2\pi\ \zeta_1)\ [\cos(2\pi\ \zeta_1) - \cos(2\pi\ \zeta_2)]} \tag{27}$$

$$\sqrt{\frac{2}{M}}\ \frac{w_{24}}{u_4} = -\sqrt{\frac{2}{M}}\ \frac{w_{34}}{u_4} = -\frac{1}{4}\ \frac{1}{\sin(2\pi\ \zeta_2)\ [\cos(2\pi\ \zeta_1) - \cos(2\pi\ \zeta_2)]} \tag{28}$$

The normalized sums of the modal correction weights are computed from Equation (A-55), and the results are shown in Figures 35 through 39. Each graph applies to a fixed position of planes 1 and 4 ($\zeta_1 = \frac{z_1}{\ell} = 0.05$, 0.125, 0.167, 0.25, and 0.333), while the position of plane 2 (and, hence, of plane 3) varies as given by the abscissa. Each graph contains four curves, giving the normalized sums of the modal correction weights.

It is found that the optimum locations of planes 1 and 2 are 0.167 and 0.375, respectively, but considerable deviations are acceptable.

As with the three mode balancing results, there are slope discontinuities in Figure 35 through 39 — this time for the first two modes. Similar arguments to those developed for the three mode case can be used to explain these discontinuities.

Uniform Shaft in Flexible, Damped Bearings

As a second example, consider a uniform shaft with overhung ends, supported in two identical bearings. The bearing coefficients are:

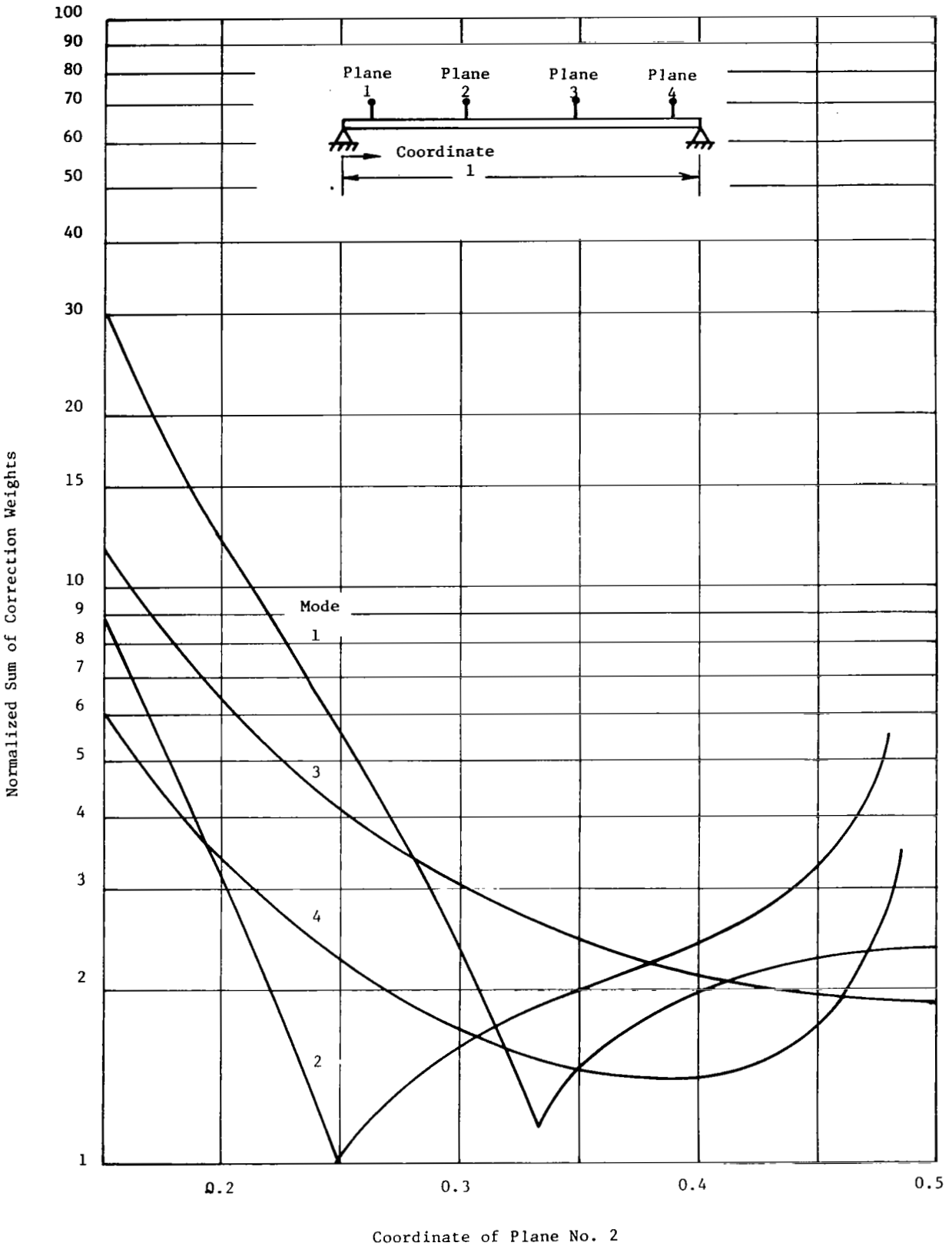

Fig. 35 Influence of Planes 2 and 3 on Normalized Sum of Correction Weights for Uniform Shaft on Rigid Bearing and Four Criticals (Coordinate of Plane No. 1 = 0.05)

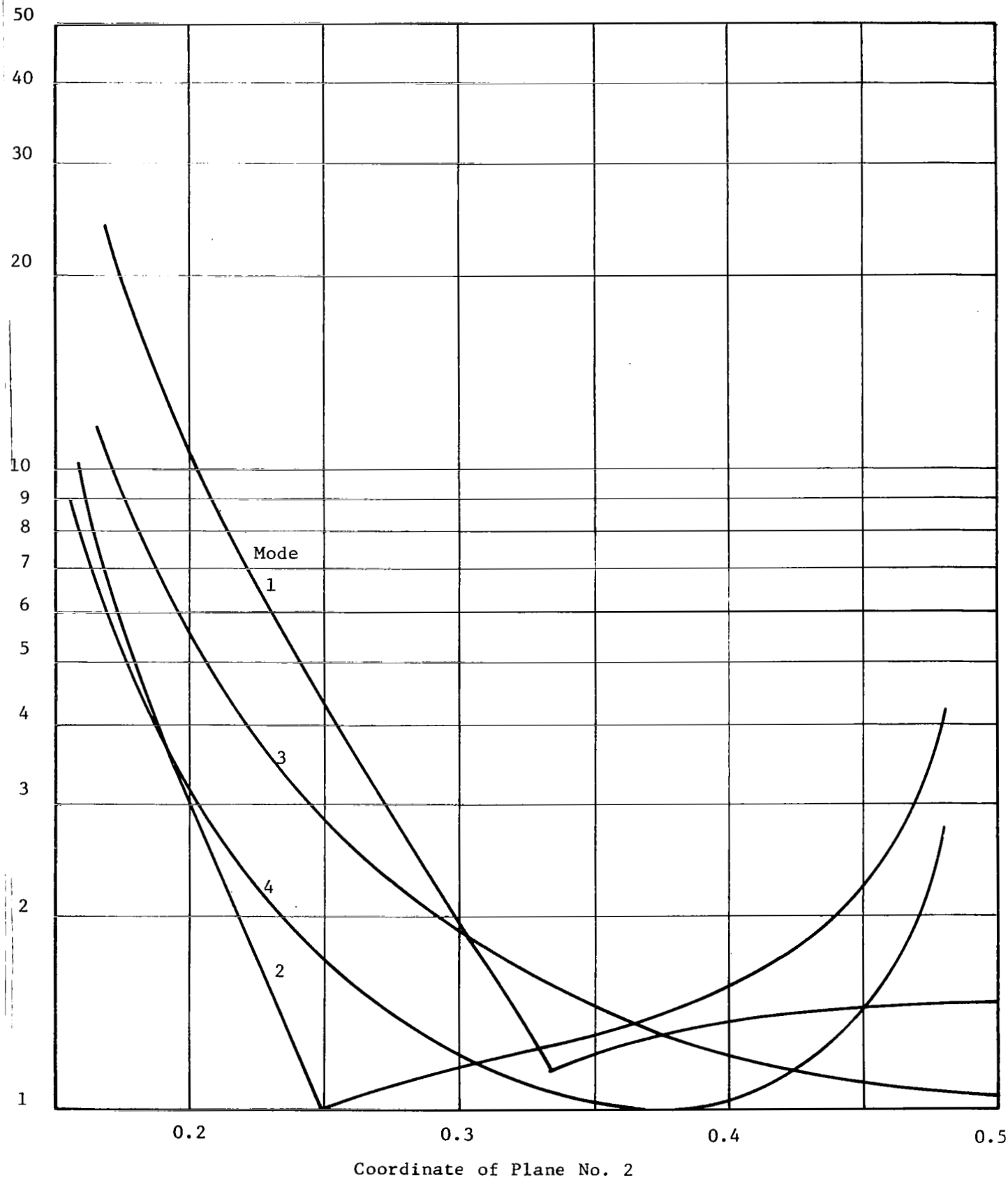

Fig. 36 Influence of Planes 2 and 3 on Normalized Sum of Correction Weights for Uniform Shaft on Rigid Bearings and Four Criticals (Coordinate of Plane No. 1 = 0.125)

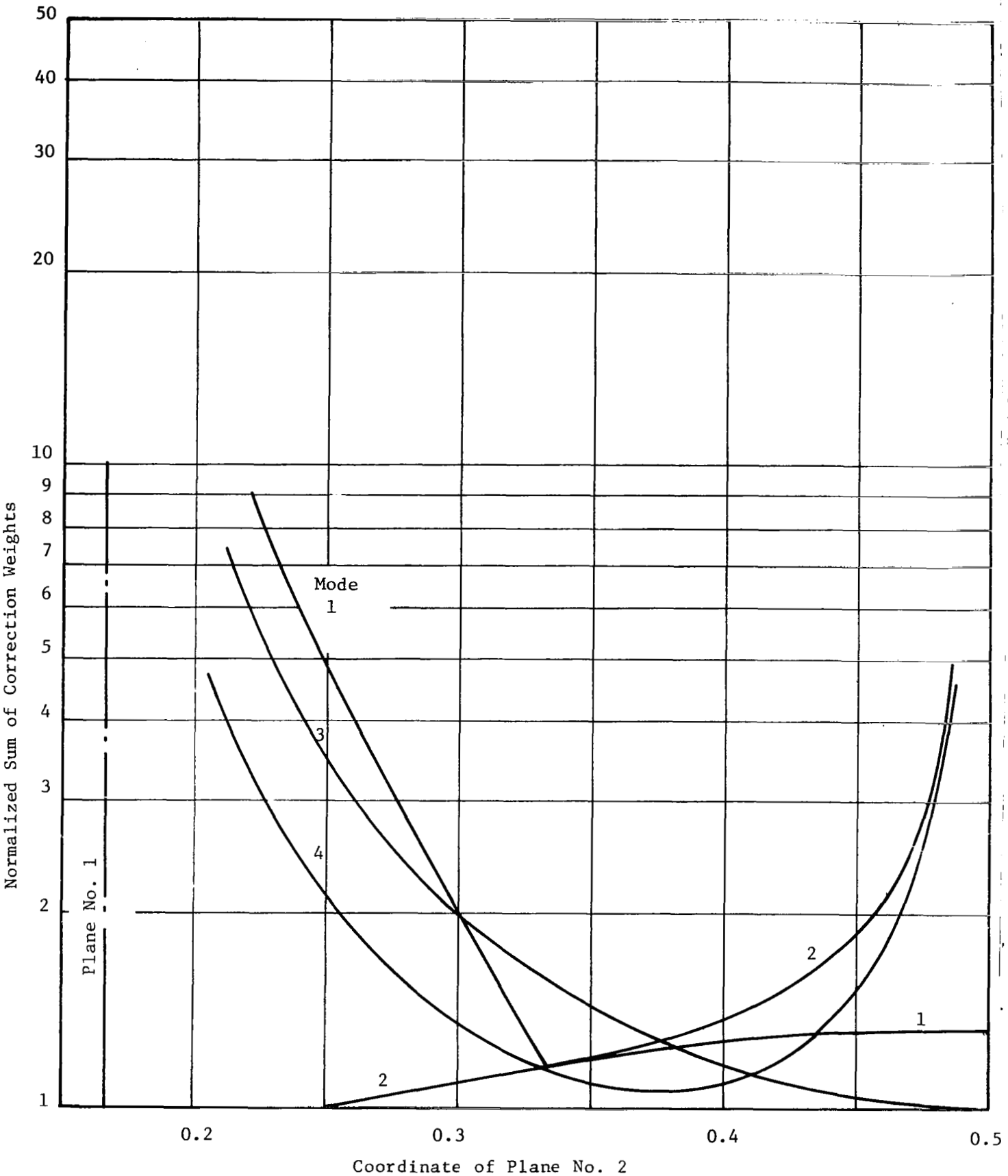

Fig. 37 Influence of Planes 2 and 3 on Normalized Sum of Correction Weights for Uniform Shaft on Rigid Bearings and Four Criticals (Coordinate of Plane No. 1 = 0.167)

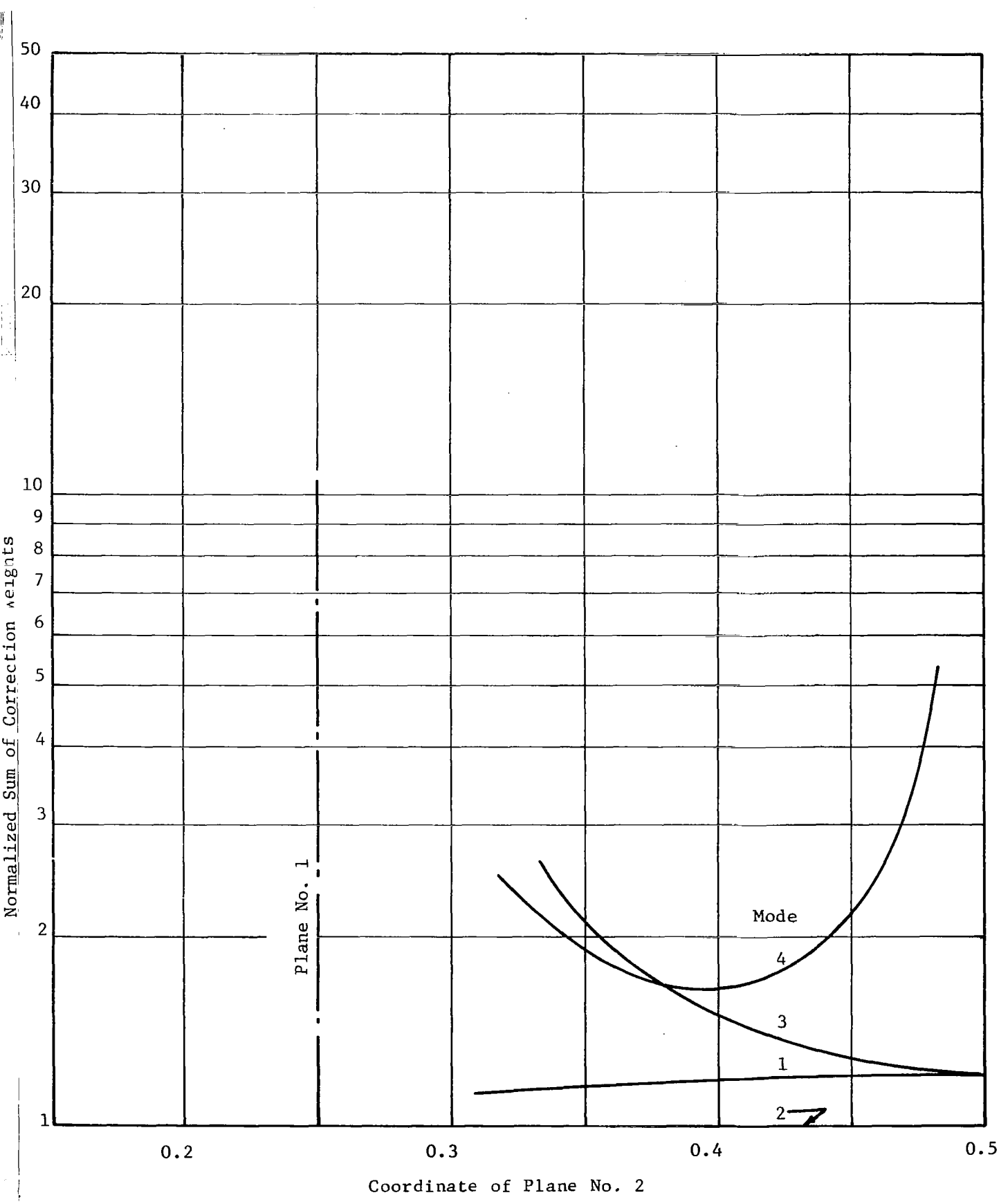

Fig. 38 Influence of Plane 1 Location on Normalized Sum of Correction Weights for Uniform Shaft on Rigid Bearings and Four Criticals (Coordinate of Plane No. 1 = 0.25)

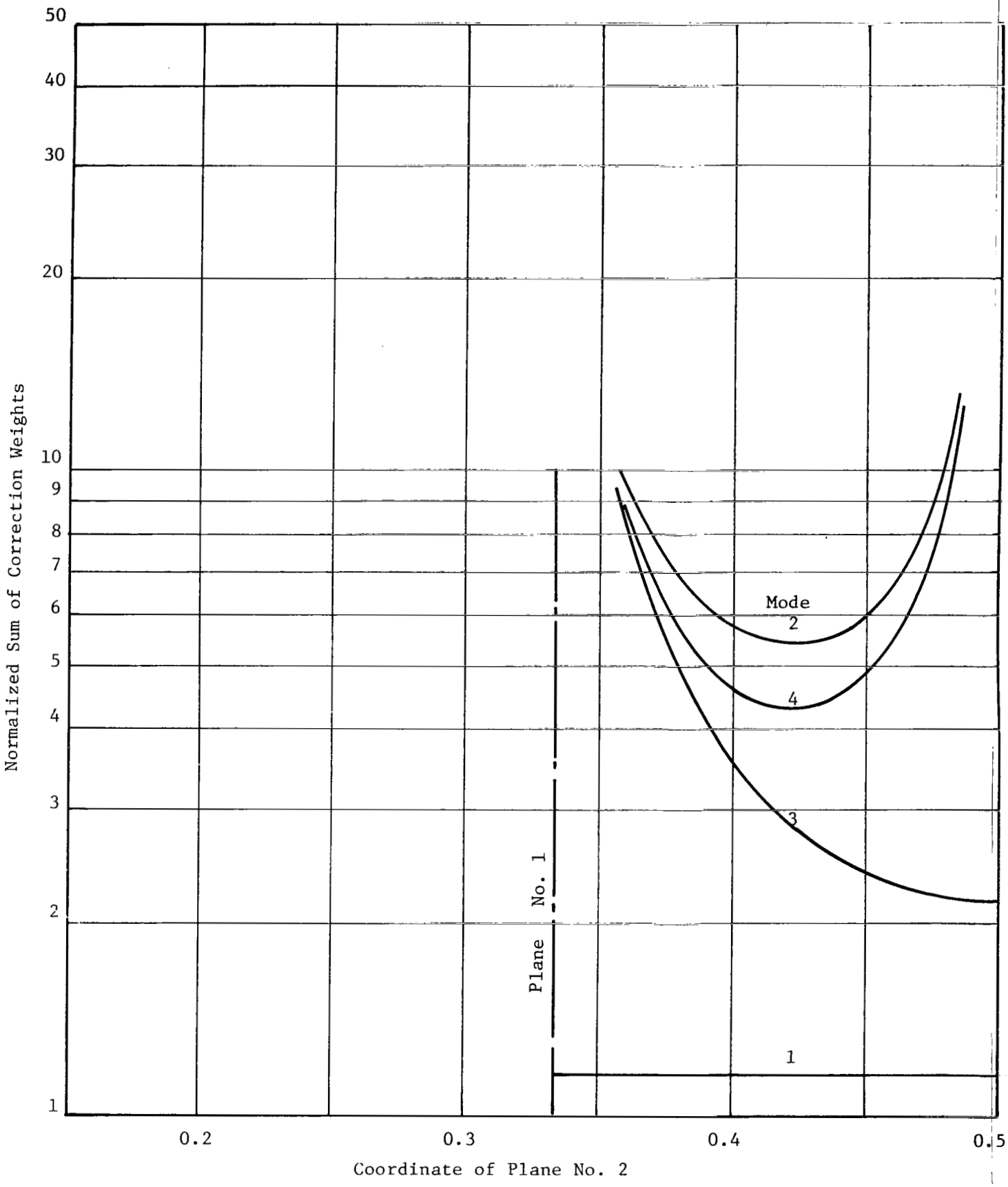

Fig. 39 Influence of Planes 2 and 3 on Normalized Sum of Correction Weights for Uniform Shaft on Rigid Bearings and Four Criticals (Coordinate of Plane No. 1 = 0.333)

$K_{xx} = 43.8 \times 10^5$ N/m $\qquad K_{yy} = 17.5 \times 10^5$ N/m

$B_{xx} = 17.5 \times 10^3$ NS/m $\qquad B_{yy} = 7 \times 10^3$ NS/m

$K_{xy} = K_{yx} = B_{xy} = B_{yx} = 0$

They are assumed to be independent of speed.

The shaft is 2.16 meters long with a uniform diameter of .09 meters and a weight of 155 kilograms. Young's modulus is 207×10^9 N/m^2. The bearing span is 1.44 meters and the system is symmetric around the center.

Ignoring gyroscopic moments, the eigenvalues become independent of speed. They are computed to be:

"Critical Speed" No.	Frequency, Hz	λ_n, sec^{-1}	ω_n, rad/sec	Log. δ_n Decrement
1	22.72	-43.20	142.74	1.901
1	34.07	-104.39	214.07	3.064
2	25.87	-59.65	162.53	2.306
2	36.71	-148.77	230.64	4.053
3	77.50	-32.42	486.95	0.418
3	78.28	-11.71	491.84	0.150
4	213.46	-23.71	1341.20	0.111
4	213.68	-9.36	1342.59	0.0438

The four modes selected for computing the modal correction weights are the first modes for the first and second critical speeds, and the second modes for the third and fourth critical speeds. In each case these are the modes with the lowest log decrements.

Because the bearings do not have cross-coupling coefficients, the adjoint functions are the same as the modal functions. They are plotted in normalized form ($\zeta_n/\sqrt{N_n}$) in Figure 40. Actually, the functions are not planar (they are complex); but, for visualization purposes, they are shown by their magnitude with the sign indicating in or out of phase.

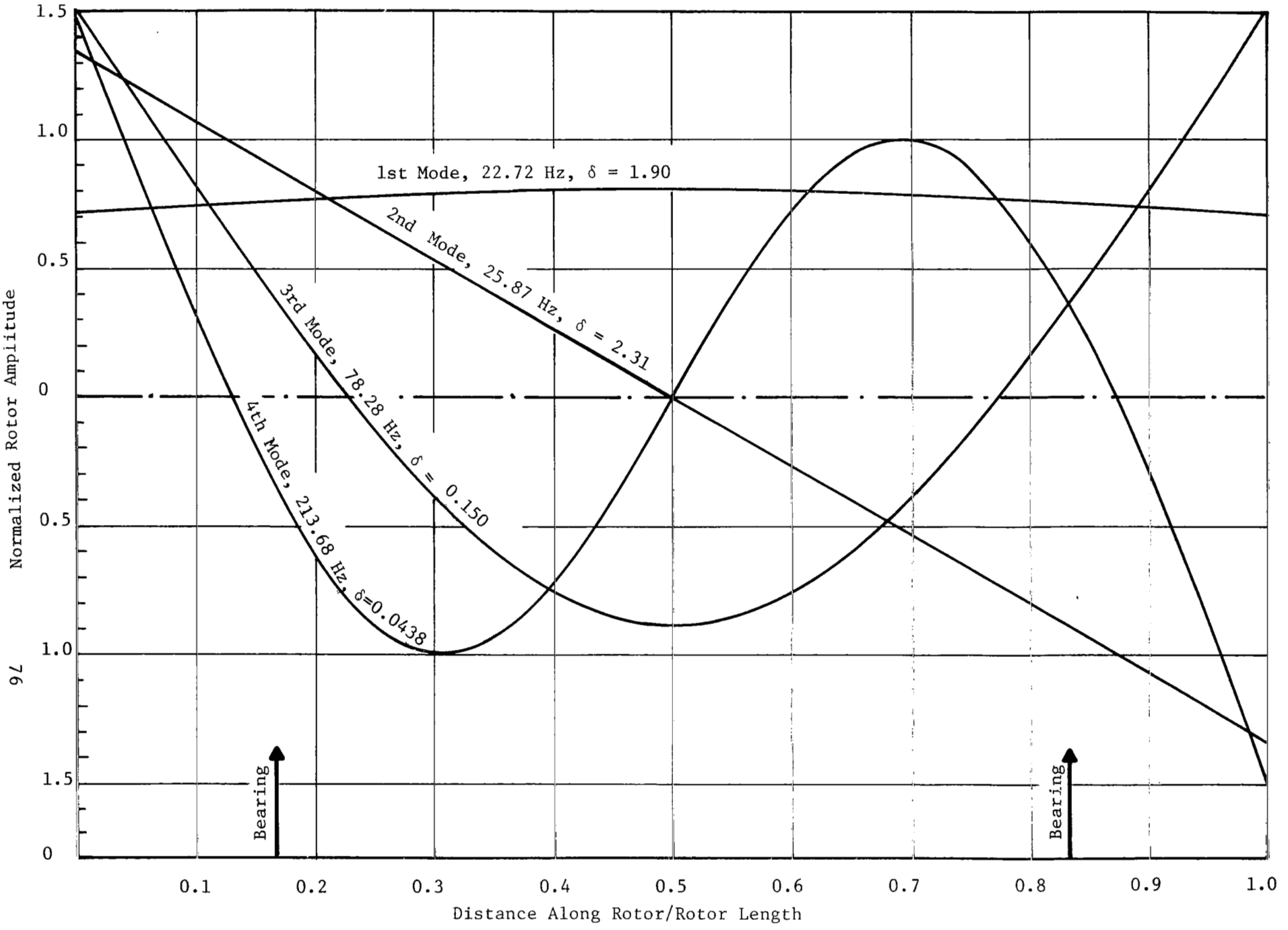

Fig. 40 Normalized Mode Shapes for First Four Critical Speeds for a Uniform Rotor on Flexible, Damped Supports

In computing the modal correction weights from Equation (A-54), the shaft is provided with four balancing planes, symmetrically arranged around the middle of the rotor such that:

$$\frac{z_4}{\ell} = 1 - \frac{z_1}{\ell} \tag{20}$$

$$\frac{z_3}{\ell} = 1 - \frac{z_2}{\ell} \tag{19}$$

Plane No. 1 (and, hence, plane No. 4) is outboard of the bearing while plane No. 2 (and, hence, plane No. 3) is between the bearing and the rotor center. Thus, the range of plane locations is:

$$0 \leq \frac{z_1}{\ell} \leq 0.167$$

$$0.167 \leq \frac{z_2}{\ell} < 0.5$$

The results are shown in Figures 41 through 44 for four fixed values of plane No. 1: $\frac{z_1}{\ell} = 0,\ 0.0417,\ 0.0833,$ and 0.125. Each graph has four curves, giving the normalized sums of the modal correction weights, Equation (A-55) as functions of the location of plane No. 2, $(\frac{z_2}{\ell})$.

As would be expected, the optimum arrangement is with plane No. 1 at the end $(\frac{z_1}{\ell} = 0)$ and plane No. 2 almost half way between the bearing and the middle of the rotor $(\frac{z_2}{\ell} \simeq 0.3)$. Considering, however, that mode Nos. 1 and 2 are very well-damped and hardly contribute to the unbalance response, the final selection of the plane locations should be based on minimizing the correction weights for the third and fourth modes.

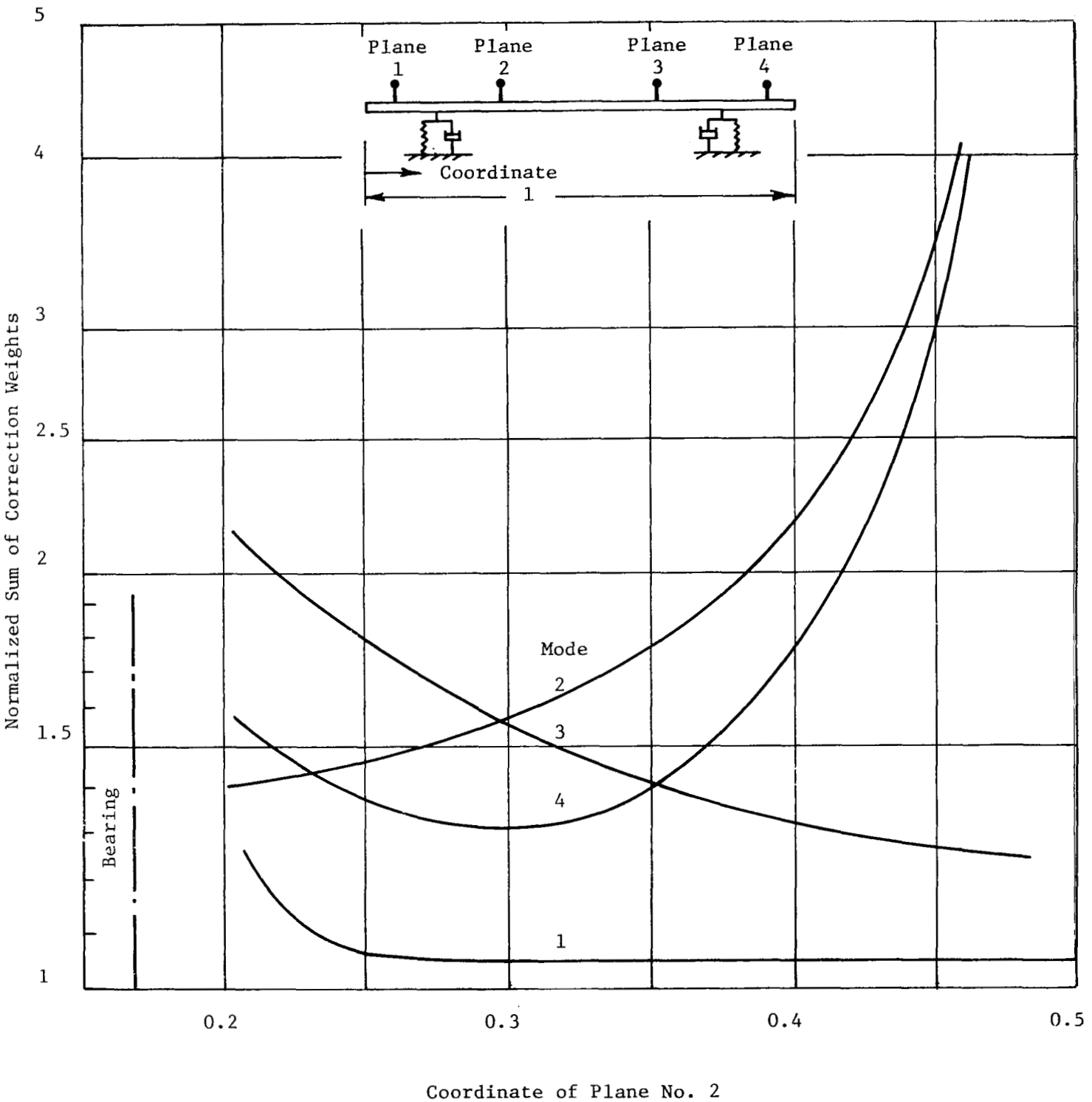

Fig. 41 Influence of Plane 2 Location on the Normalized Sum of Correction Weights for Uniform Shaft on Flexible Damped Supports (Coordinate of Plane No. 1 = 0.0)

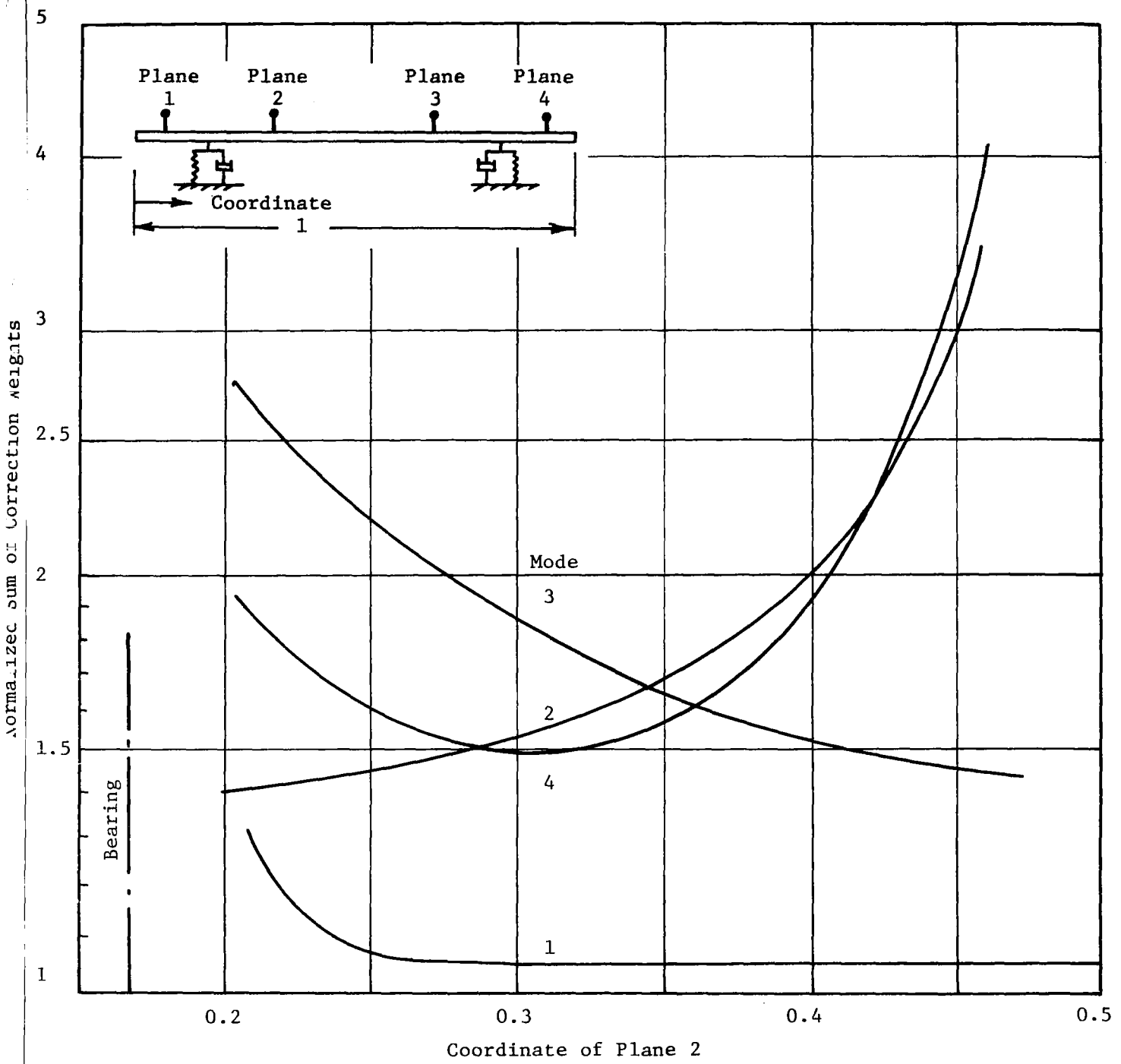

Fig. 42 Influence of Plane 2 Location on Normalized Sum of Correction Weights for Uniform Shaft on Flexible, Damped Supports (Coordinate of Plane No. 1 = 0.0417)

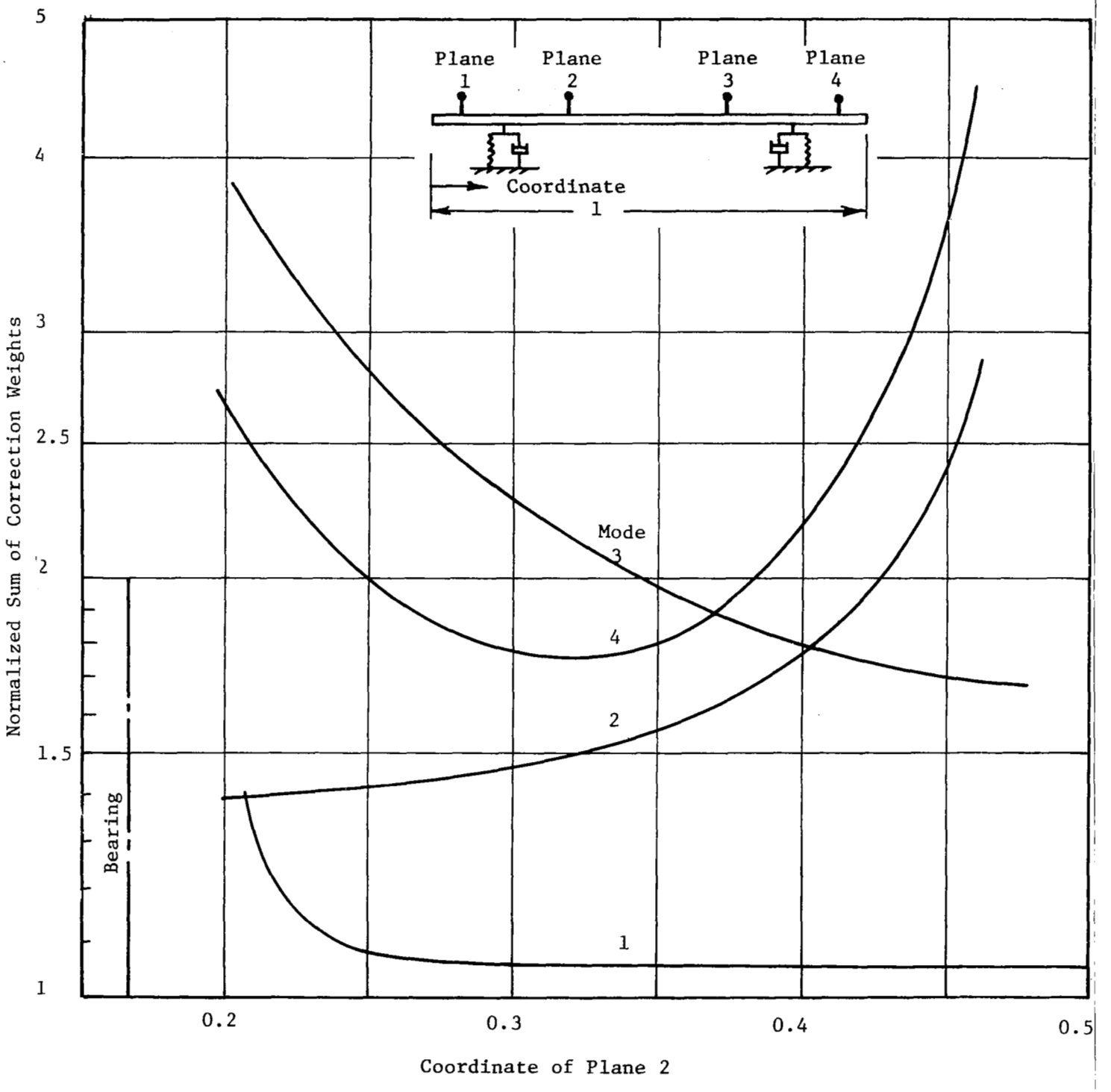

Fig. 43 Influence of Plane 2 Location on Normalized Sum of Correction Weights for Uniform Shaft on Flexible, Damped Supports (Coordinate of Plane No. 1 = 0.0833)

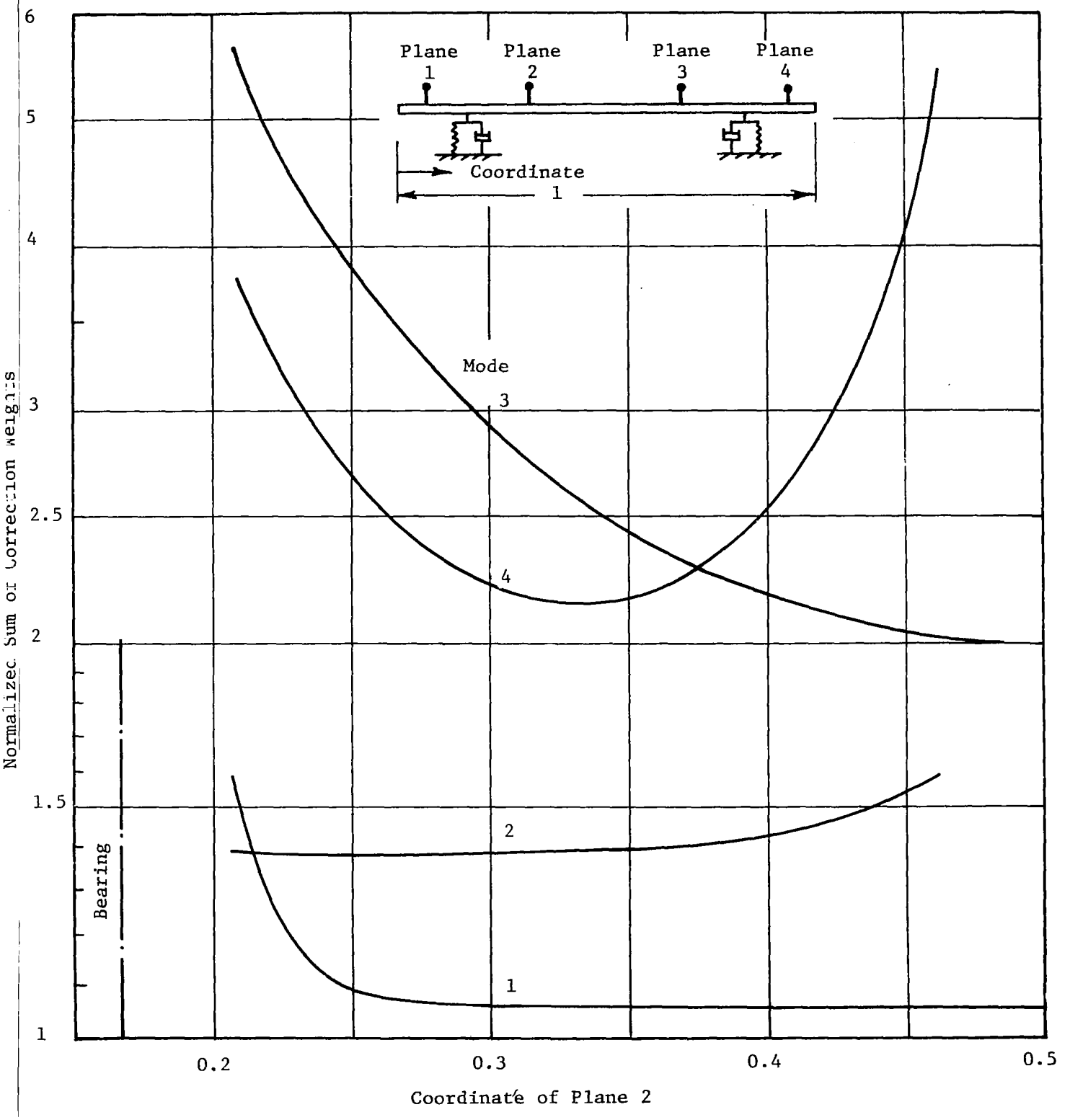

Fig. 44 Influence of Plane 2 Location on Normalized Sum of Correction Weights for Uniform Shaft on Flexible, Damped Supports (Coordinate of Plane No. 1 = 0.125)

REFERENCES

1. Tessarzik, J.M., "Flexible Rotor Balancing by the Exact Point — Speed Influence Coefficient Method", MTI Technical Report No. MTI-70TR59, NASA Contractor Report No. CR-72774, prepared for NASA - Lewis Research Center under Contract No. NAS3-13473, October 1970.

2. Tessarzik, J.M., "Flexible Rotor Balancing by the Influence Coefficient Method: Part 1 — Evaluation of the Exact Point — Speed and Least Squares Procedures", MTI Technical Report No. MTI-72TR32, NASA Contractor Report No. CR-121107, prepared for NASA - Lewis Research Center under Contract No. NAS3-14420, July 1972.

3. Tessarzik, J.M., "Flexible Rotor Balancing by the Influence Coefficient Method — Multiple Critical Speeds with Rigid or Flexible Supports", MTI Technical Report No. MTI-75TR3, NASA Contractor Report CR-2553, prepared for NASA - Lewis Research Center under Contract No. NAS3-14420, February 1975.

4. Lund, J.W., "Stability and Damped Critical Speeds of a Flexible Rotor in Fluid Film Bearings", J. Engineering for Industry, Trans., ASME Vol. 96, No. 2, 1974, pp. 509-517.

5. Lund, J.W., and Tonnesen, J., "Analysis and Experiments on Multiplane Balancing of a Flexible Rotor", Journal of Engineering for Industry, Transactions of the ASME, Series B, Volume 94, Number 1, 1972, pp. 233-242.

6. Dimentberg, F. M., FLEXURAL VIBRATIONS OF ROTATING SHAFTS, Butterworths, London, 1961.

7. Bishop, R.E.D., "Vibration of Rotating Shafts", Journal of Mechanical Engineering Science, Volume 1, Number 1, 1959, pp. 50-65.

8. Parkinson, A.G., and Bishop, R.E.D., "Vibration and Balancing of Rotating Continuous Shafts", Journal of Mechanical Engineering Science, Volume 3, Number 3, 1961, pp. 200-213.

9. Kellenberger, W., "Should a Flexible Rotor be Balanced in N or (N + 2) Planes?", Journal of Engineering for Industry, Transactions of the ASME, Series B, Volume 94, Number 2, 1972, pp 548-560.

10. Bones, J.A., and Hannam, R.G., "Whirling of Shafts with Asymmetric Stiffness", Journal of Engineering Science, Volume 8, Number 4, 1966, pg. 437.

11. Timoshenko, S., "Vibration Problems in Engineering", 3rd ed., D. Van Nostrand Co., Princeton, New Jersey, 1955.

12. Tessarzik, J.; Gillham, F.; and Badgley, R., "Multiplane Balancing Criteria for the General Electric T700 Engine Power Turbine Rotor", MTI 75TR36, April 1975.

13. Badgley, R.H., "Implications of Multiplane - Multispeed Balancing for Future Turbine Engine Design and Cost", Society of Automotive Engineers, Paper No. 740865, presented at the National Aerospace Engineering and Manufacturing Meeting, San Diego, California, October 1974.

14. Badgley, R.H., "The Potential Impact of Multiplane - Multispeed Balancing on Gas Turbine Production and Overhaul Costs", Journal of Engineering for Power, Trans. ASME, vol. 97, 1975, pp. 347-354.

APPENDIX A

ANALYTICAL DEVELOPMENT OF CRITERIA FOR BALANCE PLANE AND SENSOR LOCATION

by Dr. J. W. Lund

DEFINITION OF THE PROBLEM

The vibrations of an unbalanced rotor are recorded by measurements of amplitude and phase angle at selected locations and speeds. With x representing the synchronous vibration, it may be expressed as:

$$x = |x| \cdot \cos(\Omega t + \varphi) = |x| \cdot \cos\varphi \cdot \cos\Omega t - |x| \cdot \sin\varphi \cdot \sin\Omega t \quad (1)$$

where

$|x|$ = Vibration amplitude
φ = Phase angle
Ω = Angular speed of rotation

Equation (1) can also be written as:

$$x = \mathrm{Re}\left\{(x_c + i\,x_s)\, e^{i\Omega t}\right\} \quad (2)$$

where

$$x_c = |x| \cdot \cos\varphi \qquad x_s = |x| \cdot \sin\varphi$$

By convention it is customary to adopt the abbreviated form:

$$x = x_c + ix_s \quad (3)$$

which, then, implies Equation (2) in the final evaluation.

The vibration can be considered as caused by discrete mass unbalances, U_k, in the rotor. With index j defining the location and speed at which the amplitude is measured, x_j is given by

$$(x_j)_o = \sum_k H_{jk}\, U_k \quad (4)$$

when H_{jk} are the dynamic influence coefficients (they are complex). The equation may also be written in matrix form as:

$$\underline{X}_o = \underline{\underline{A}} \cdot \underline{U} \tag{5}$$

where $\underline{X}_o$ and $\underline{U}$ are column vectors with elements $(x_j)_o$ and U_k, respectively, and $\underline{\underline{A}}$ is a matrix with elements H_{jk}.

To balance the rotor, correction weights w_p are inserted in a number of planes. The resulting residual amplitudes become:

$$x_j = (x_j)_o + \sum_p H_{jp} w_p = \sum_k H_{jk} U_k + \sum_p H_{jp} w_p \tag{6}$$

or, in matrix form:

$$\underline{X} = \underline{X}_o + \underline{\underline{H}} \cdot \underline{W} = \underline{\underline{A}} \cdot \underline{U} + \underline{\underline{H}} \cdot \underline{W} \tag{7}$$

where $\underline{X}$ and $\underline{W}$ are column vectors with elements x_j and w_p, respectively, and $\underline{\underline{H}}$ is the influence coefficient matrix with elements H_{jp}.

As shown in Reference 5, the correction weights are determined by a least squares minimization of the residual amplitudes $\underline{X}$:

$$\underline{W} = - (\overline{\underline{\underline{H}}}^T \underline{\underline{H}})^{-1} \overline{\underline{\underline{H}}}^T \underline{X}_o = - (\overline{\underline{\underline{H}}}^T \underline{\underline{H}})^{-1} \overline{\underline{\underline{H}}}^T \underline{\underline{A}} \cdot \underline{U} \tag{8}$$

Where $\overline{\underline{\underline{H}}}^T$ is the transposed, complex conjugate matrix of $\underline{\underline{H}}$.

From the equation, it is seen that the required balance correction weights depend on three factors:

a the location of the balance correction planes (through $\underline{\underline{H}}$)
b the location of the measurement probes (through $\underline{\underline{H}}$ and $\underline{\underline{A}}$)
c the mass unbalance distribution (through $\underline{\underline{A}}$).

Thus, to achieve an acceptable balance correction of a given rotor, consideration must be given to the selection of the number and locations of the correction

planes and the measurement probes and, therefore, it becomes of interest to investigate whether some form of a general selection procedure can be established. This is the purpose of the present analysis.

To be useful, such a procedure must be applicable at the design stage. Hence, it must be independent of how the residual mass unbalance actually happens to be distributed in the manufactured rotor. Secondly, the procedure should allow for some freedom of choice among a suitable range of alternatives to accommodate the practical restrictions imposed by the particular rotor design. For these reasons and, also, because of the many parameters involved, a direct optimization of Equation (8) does not appear suitable.

Instead, a generalized modal approach is employed where both the residual unbalance and the rotor amplitudes are expressed in terms of their modal components. By requiring each mode to be balance-corrected by itself without interferring with the correction of other modes, a unique set of correction weights can be found, one set for each mode. The optimum arrangement of balancing planes is, then, that combination which minimizes the total amount of correction weights.

In principle, the outlined method employs the general techniques used in modal balancing procedures (References 6 to 9). However, whereas conventional modal balancing only applies to ideal rotors without damping in the bearings, the present analysis considers the more common practical rotor-bearing system, allowing for bearing damping and anisotropic stiffness properties. As such, the analysis is not exact in terms of the classical modal representation but, for the present purposes of investigating the location of balancing planes, it should have adequate accuracy.

ANALYSIS

Governing Equations

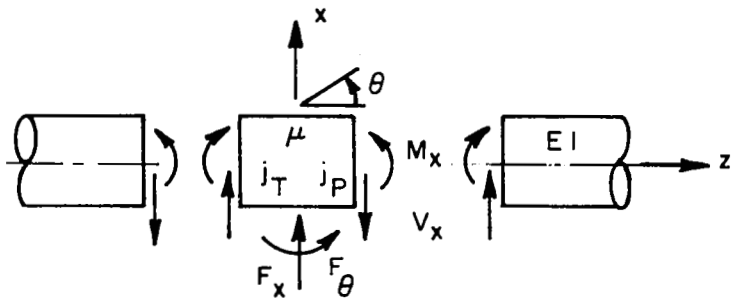

The lateral shaft amplitudes are x and y with corresponding angular deflections of θ and φ, respectively. The bending moments and shear forces are M_x, M_y, V_x, and V_y. With z being the coordinate along the shaft, the conventional beam deformation equations are:

$$\frac{\partial \theta}{\partial z} = \frac{1}{EI} M_x \qquad \frac{\partial \varphi}{\partial z} = \frac{1}{EI} M_y \tag{9}$$

$$\frac{\partial x}{\partial z} = \theta \qquad \frac{\partial y}{\partial z} = \varphi \tag{10}$$

where E is Young's modulus and I is the transverse cross sectional area moment of inertia.

Per unit length the shaft has the mass μ, the polar mass moment of inertia j_p, and the transverse mass moment of inertia j_T. Hence, a force balance and a moment balance for a differential element yield the following equations:

$$\mu \frac{\partial^2 x}{\partial t^2} + \frac{\partial V_x}{\partial z} + \sum_k \delta(z-z_k) \left[K_{xx}\, x + K_{xy}\, y + B_{xx} \frac{\partial x}{\partial t} + B_{xy} \frac{\partial y}{dt} \right]_k = F_x \tag{11}$$

$$\mu \frac{\partial^2 y}{\partial t^2} + \frac{\partial V_y}{\partial z} + \sum_k \delta(z-z_k) \left[K_{yx}\, x + K_{yy}\, y + B_{yx} \frac{\partial x}{\partial t} + B_{yy} \frac{\partial y}{\partial t} \right]_k = F_y \tag{12}$$

$$j_T \frac{\partial^2 \theta}{\partial t^2} + \Omega\, j_p \frac{\partial \varphi}{\partial t} + V_x - \frac{\partial M_x}{\partial z} = F_\theta \tag{13}$$

$$j_T \frac{\partial^2 \varphi}{\partial t^2} - \Omega j_p \frac{\partial \theta}{\partial t} + V_y - \frac{\partial M_y}{\partial z} = F_\varphi \tag{14}$$

where

F_x, F_y	=	External forces per unit length
F_θ, F_φ	=	External moments per unit length
$K_{xx}, K_{xy}, K_{yx}, K_{yy}$	=	Bearing stiffness coefficients
$B_{xx}, B_{xy}, B_{yx}, B_{yy}$	=	Bearing damping coefficients
Ω	=	Angular speed of rotation
k	=	Bearing index
$\delta(z-z_k)$	=	Unit delta function

For the purpose of computing unbalance vibrations, it proves convenient to introduce the forward and backward precessional components:

Forward precessional component:

$$\xi = \frac{1}{2}(x + iy)$$

$$\alpha = \frac{1}{2}(\theta + i\varphi) \tag{15}$$

Backward precessional component:

$$\eta = \frac{1}{2}(x - iy)$$

$$\beta = \frac{1}{2}(\theta - i\varphi) \tag{16}$$

and similarly for the bending moments and shear forces ($i = \sqrt{-1}$).

By these substitutions, Equations (9) to (14) are transformed into:

$$\frac{\partial \alpha}{\partial z} = \frac{1}{EI} M_\xi \qquad \frac{\partial \beta}{\partial z} = \frac{1}{EI} M_\eta \tag{17}$$

$$\frac{\partial \xi}{\partial z} = \alpha \qquad \frac{\partial \eta}{\partial z} = \beta \tag{18}$$

$$\mu \frac{\partial^2 \xi}{\partial t^2} + \frac{\partial V_\xi}{\partial z} + \sum_k \delta(z-z_k) \left[K_{\xi\xi}\, \xi + K_{\xi\eta}\, \eta + B_{\xi\xi} \frac{\partial \xi}{\partial t} + B_{\xi\eta} \frac{\partial \eta}{\partial t} \right]_k = \frac{1}{2} (F_x + i\, F_y) = F_\xi \quad (19)$$

$$\mu \frac{\partial^2 \eta}{\partial t^2} + \frac{\partial V_\eta}{\partial z} + \sum_k \delta(z-z_k) \left[K_{\eta\xi}\, \xi + K_{\eta\eta}\, \eta + B_{\eta\xi} \frac{\partial \xi}{\partial t} + B_{\eta\eta} \frac{\partial \eta}{\partial t} \right]_k = \frac{1}{2} (F_x - i\, F_y) = F_\eta \quad (20)$$

$$j_T \frac{\partial^2 \alpha}{\partial t^2} - i\Omega j_p \frac{\partial \alpha}{\partial t} + V_\xi - \frac{\partial M_\xi}{\partial z} = \frac{1}{2} (F_\theta + i\, F_\varphi) = F_\alpha \quad (21)$$

$$j_T \frac{\partial^2 \beta}{\partial t^2} + i\Omega j_p \frac{\partial \beta}{\partial t} + V_\eta - \frac{\partial M_\eta}{\partial z} = \frac{1}{2} (F_\theta - i\, F_\varphi) = F_\beta \quad (22)$$

where

$$\begin{aligned} K_{\xi\xi} &= \frac{1}{2} \left[K_{xx} + K_{yy} - i\, (K_{xy} - K_{yx}) \right] \\ K_{\xi\eta} &= \frac{1}{2} \left[K_{xx} - K_{yy} + i\, (K_{xy} + K_{yx}) \right] \\ K_{\eta\xi} &= \frac{1}{2} \left[K_{xx} - K_{yy} - i\, (K_{xy} + K_{yx}) \right] \\ K_{\eta\eta} &= \frac{1}{2} \left[K_{xx} + K_{yy} + i\, (K_{xy} - K_{yx}) \right] \end{aligned} \quad (23)$$

and analogously for the four damping coefficients.

Modal Functions

In the absence of external forces ($F_\xi = F_\eta = F_\alpha = F_\beta = 0$), the solution to the homogeneous equations is of the form:

$$\xi = \xi_n e^{s_n t} \qquad \eta = \eta_n e^{s_n t} \quad (24)$$

and similarly for the other variables. ξ_n and η_n are the modal functions for mode number n, and s_n is the eigenvalue:

$$s_n = \lambda_n + i\omega_n \quad (25)$$

where ω_n is the frequency (radians/sec) and λ_n is the corresponding damping exponent (sec^{-1}). A numerical procedure for calculating the eigenvalues and the modal functions for a general rotor-bearing system is given in References 5 and 6.

Substitution of Equation (24) into Equations (19) to (22) gives the following equations:

$$s_n^2 \mu \xi_n + \frac{dV_{\xi n}}{dz} + \sum_k \delta(z-z_k) \left[(K_{\xi\xi} + s_n B_{\xi\xi}) \xi_n + (K_{\xi\eta} + s_n B_{\xi n}) \eta_n \right]_k = 0 \quad (2$$

$$s_n^2 \mu \eta_n + \frac{dV_{\eta n}}{dz} + \sum_k \delta(z-z_k) \left[(K_{\eta\xi} + s_n B_{\eta\xi}) \xi_n + (K_{\eta\eta} + s_n B_{\eta\eta}) \eta_n \right]_k = 0 \quad (2$$

$$(s_n^2 j_T - i s_n \Omega j_p) \alpha_n + V_{\xi n} - \frac{dM_{\xi n}}{dz} = 0 \quad (2$$

$$(s_n^2 j_T + i s_n \Omega j_p) \beta_n + V_{\eta n} - \frac{dM_{\eta n}}{dz} = 0 \quad (2$$

From Equations (17) and (18):

$$\frac{d\alpha_n}{dz} = \frac{1}{EI} M_{\xi\eta} \qquad \frac{d\beta_n}{dz} = \frac{1}{EI} M_{\eta n} \quad (3$$

$$\frac{d\xi_n}{dz} = \alpha_n \qquad \frac{d\eta_n}{dz} = \beta_n \quad (3$$

If, in Equations (26) and (27), $K_{\xi\eta}$ and $K_{\eta\xi}$ are interchanged and, also, $B_{\xi\eta}$ and $B_{\eta\xi}$, the equations still possess the same eigenvalues but yield a new set of modal functions: ξ_n^*, η_n^*, etc., which are called the adjoint functions. They obey certain orthogonality conditions which can be derived as follows: multiply Equations (26), (27), (28), and (29) by ξ_m^*, η_m^*, α_m^* and β_m^*, respectively, add the equations and integrate over the rotor length ℓ. The final expression becomes:

$$\int_0^\ell \left\{ s_n^2 \left[\mu(\xi_m^* \xi_n + \eta_m^* \eta_n) + j_T (\alpha_m^* \alpha_n + \beta_m^* \beta_n) \right] - s_n i\Omega j_p (\alpha_m^* \alpha_n - \beta_m^* \beta_n) \right\} dz$$

$$+ s_n \sum_k \left\{ \xi_m^*, \eta_m^* \right\} \begin{Bmatrix} B_{\xi\xi} & B_{\xi\eta} \\ B_{\eta\xi} & B_{\eta\eta} \end{Bmatrix}_k \begin{Bmatrix} \xi_n \\ \eta_n \end{Bmatrix} =$$

$$= - \int_0^{\ell} \left\{ \xi_m^* \frac{dV_{\xi n}}{dz} + \eta_m^* \frac{dV_{\eta n}}{dz} + \alpha_m^* \left(V_{\xi n} - \frac{dM_{\xi n}}{dz} \right) + \beta_m^* \left(V_{\eta n} - \frac{dM_{\eta n}}{dz} \right) \right\} dz$$

$$- \sum_k \left\{ \xi_m^*, \eta_m^* \right\} \begin{Bmatrix} K_{\xi\xi} & K_{\xi\eta} \\ K_{\eta\xi} & K_{nn} \end{Bmatrix}_k \begin{Bmatrix} \xi_n \\ \eta_n \end{Bmatrix} \qquad (32)$$

By partial integration and making use of Equations (30) and (31), the integral on the right-hand side of Equation (32) reduces to:

$$- \left[\xi_m^* V_{\xi n} + \eta_m^* V_{\eta n} - \alpha_m^* M_{\xi n} - \beta_m^* M_{\eta n} \right]_{z=0}^{z=\ell} - \int_0^{\ell} \frac{1}{EI} \left(M_{\xi m}^* M_{\xi n} + M_{\eta m}^* M_{\eta n} \right) dz \qquad (33)$$

As the ends of the rotor are free ($M_{\xi n} = M_{\eta n} = V_{\xi n} = V_{\eta n} = 0$ at $z = 0$ and $z = \ell$), the square bracket is zero.

An analogous expression can be derived by letting Equations (26) to (31) apply to the eigenvalues s_m and the adjoint modal functions. Multiplying by ξ_n, η_n, α_n and β_n, respectively, adding, and integrating over the rotor length yields the same result as Equations (32) and (33) with s_n replaced by s_m. As the right-hand side is independent of the eigenvalue, the two results can be subtracted to give an orthogonality condition:

$$\int_0^{\ell} \left\{ (s_n + s_m) \left[\mu (\xi_m^* \xi_n + \eta_m^* \eta_n) + j_T (\alpha_m^* \alpha_n + \beta_m^* \beta_n) \right] - i\Omega j_p (\alpha_m^* \alpha_n - \beta_m^* \beta_n) \right\} dz$$

$$+ \sum_k \left\{ \xi_m^*, \eta_m^* \right\} \underline{\underline{B}}_k \begin{Bmatrix} \xi_n \\ \eta_n \end{Bmatrix} = \begin{cases} 0 & \underline{n \neq m} \\ 2 s_n N_n & \underline{n = m} \end{cases} \qquad (34)$$

where $\underline{\underline{B}}$ is the matrix of bearing damping coefficients shown in Equation (32). N_n is the modal norm which, according to the derivation of Equation (34) from Equations (32) and (33), is evaluated as:

$$2s_n N_n = \lim_{s_m \to s_n} \left\{ \frac{1}{s_n - s_m} \left[\alpha_m^* M_{\xi n} - \alpha_n M_{\xi m}^* + \beta_m^* M_{\eta n} - \beta_n M_{\eta m}^* - \xi_m^* V_{\xi n} \right. \right.$$

$$\left. \left. + \xi_n V_{\xi m}^* - \eta_m^* V_{\eta n} + \eta_n V_{\eta m}^* \right]_0^{\ell} \right\}$$

$$= \left[\alpha_n^* \frac{dM_{\xi n}}{ds} + \beta_n^* \frac{dM_{\eta n}}{ds} - \xi_n^* \frac{dV_{\xi n}}{ds} - \eta_n^* \frac{dV_{\eta n}}{ds} \right]_0^{\ell} \tag{35}$$

under the assumption of free rotor ends ($M_{\xi n}^* = M_{\eta n}^* = V_{\xi n}^* = V_{\eta n}^* = 0$ at $z = 0$ and $z = \ell$).

Substitution of Equation (34) into Equation (32) yields an additional orthogonality condition:

$$\int_0^{\ell} \left\{ \xi_n^* \frac{dV_{\xi n}}{dz} + \eta_m^* \frac{dV_{\eta n}}{dz} + \alpha_m^* \left(V_{\xi n} - \frac{dM_{\xi n}}{dz} \right) + \beta_m^* \left(V_{\eta n} - \frac{dM_{\eta n}}{dz} \right) \right.$$

$$\left. - s_n s_m \left[\mu \left(\xi_m^* \xi_n + \eta_m^* \eta_n \right) + j_T \left(\alpha_m^* \alpha_n + \beta_m^* \beta_n \right) \right] \right\} dz$$

$$+ \sum_k \left\{ \xi_m^* , \eta_m^* \right\} \underline{\underline{K}}_k \begin{Bmatrix} \xi_n \\ \eta_n \end{Bmatrix} =$$

$$\int_0^{\ell} \left\{ \frac{1}{EI} \left(M_{\xi m}^* M_{\xi n} + M_{\eta m}^* M_{\eta n} \right) - s_n s_m \left[\mu \left(\xi_m^* \xi_n + \eta_m^* \eta_n \right) + j_T \left(\alpha_m^* \alpha_n + \beta_m^* \beta_n \right) \right] \right\} dz$$

$$+ \sum_k \left\{ \xi_m^* , \eta_m^* \right\} \underline{\underline{K}}_k \begin{Bmatrix} \xi_n \\ \eta_n \end{Bmatrix} = \begin{cases} 0 & n \neq m \\ -2 s_n^2 N_n & n = m \end{cases} \tag{36}$$

where $\underline{\underline{K}}$ is the matrix of bearing stiffness coefficients shown in Equation (32).

When s_n is an eigenvalue and complex, the conjugate value $\bar{s}_n$ is also an eigenvalue. Because the bearing coefficients: $K_{\xi\xi}$, $B_{\xi\xi}$, etc., are complex (see Equation (23)), the corresponding modal functions and adjoint functions are found from Equations (26) to (31) to become:

$$(\xi_m)_{s_m=\bar{s}_n} = \bar{\eta}_n \qquad (\eta_m)_{s_m=\bar{s}_n} = \bar{\xi}_n$$

$$(\xi_m^*)_{s_m=\bar{s}_n} = \bar{\eta}_n^* \qquad (\eta_m^*)_{s_m=\bar{s}_n} = \bar{\xi}_n^* \tag{37}$$

Unbalance Response

Returning to the original equations, Equations (17) to (22), they may be solved by setting:

$$\xi = \sum_n \xi_n q_n \tag{38}$$

$$\frac{\partial \xi}{\partial t} = \sum_n s_n \xi_n q_n = \sum_n \xi_n \frac{dq_n}{dt} \tag{39}$$

and similarly for the remaining variables: η, α, β, M_ξ, etc., and their time derivatives. This represents a series expansion of the amplitude into its modal components where q_n determines how much the particular mode contributes to the overall response. q_n is known as the normal coordinate.

Equations (38) and (39) are substituted into Equations (19) to (22) which, then, are multiplied by ξ_m^*, η_m^*, α_m^* and β_m^*, respectively. By adding, integrating over the rotor length, and making use of the orthogonality conditions, Equations (34) and (36), a first order, ordinary differential equation is obtained:

$$2s_m N_m \frac{dq_m}{dt} - 2s_m^2 N_m q_m = \int_0^\ell (\xi_m^* F_\xi + \eta_m^* F_\eta + \alpha_m^* F_\alpha + \beta_m^* F_\beta)\, dz \tag{40}$$

The mass unbalance in the rotor can be represented by the eccentricity of the local rotor mass center from the axis of rotation. By fixing orthogonal axes in the rotating shaft, the eccentricity is given the components ϵ_c and ϵ_s along these axes, and with μ as the rotor mass per unit length, the unbalance forces per unit length become:

$$F_x = \Omega^2 \mu (\epsilon_c \cdot \cos \Omega t - \epsilon_s \cdot \sin \Omega t)$$

$$F_y = \Omega^2 \mu (\epsilon_c \cdot \sin \Omega t + \epsilon_s \cdot \cos \Omega t) \qquad (41)$$

Similarly, the local mass axis may form an angle with the axis of rotation. Referred to the rotating coordinate system, the angle has the components ψ_c and ψ_s, respectively (for a continuous mass unbalance, $\psi_c = d\epsilon_c/dz$ and $\psi_s = d\epsilon_s/dz$.) Hence, the unbalanced moments per unit length become:

$$F_\theta = \Omega^2 (j_T - j_p) (\psi_c \cos \Omega t - \psi_s \sin \Omega t)$$
$$F_\varphi = \Omega^2 (j_T - j_p) (\psi_c \sin \Omega t + \psi_s \cos \Omega t) \qquad (42)$$

Adopting the complex notation of Equations (1) to (3), the unbalance forces and moments may also be expressed as:

$$F_x = \Omega^2 \mu (\epsilon_c + i\, \epsilon_s) = \Omega^2 \mu\, \epsilon$$

$$F_y = -i\, F_x$$

$$F_\theta = \Omega^2 (j_T - j_p) (\psi_c + i\, \psi_s) = \Omega^2 (j_T - j_p)\, \psi$$

$$F_\varphi = -i\, F_\theta \qquad (43)$$

where:

$$\epsilon = \epsilon_c + i\, \epsilon_s$$

$$\psi = \psi_c + i\, \psi_s \qquad (44)$$

Substituting Equation (43) into the right-hand sides of Equations (19) to (22), it is seen that:

$$F_\xi = \Omega^2 \mu\, \epsilon$$

$$F_\alpha = \Omega^2 (j_T - j_p)\, \psi$$

$$F_\eta = F_\beta = 0 \qquad (45)$$

which simply states that the unbalance forces only do work on the forward precessional motion.

Introducing Equation (45) into Equation (40), the normal coordinates can be determined. Changing the index from m to n and adopting the same complex notation for q_n as already done for the unbalance forces, the solution becomes:

$$q_n = \frac{\Omega^2}{2\, s_n\, (i\Omega - s_n)} \frac{1}{N_n} \int_0^{\ell} (\mu\, \xi_n^*\, \epsilon + (j_T - j_p)\, \alpha_n^*\, \psi)\, dz \tag{46}$$

Finally, the resulting forward precessional response is found from Equation (38) as:

$$\xi = \sum_n \frac{\Omega^2}{2\, s_n\, (i\Omega - s_n)} \cdot \frac{\xi_n}{\sqrt{N_n}} \cdot U_n \tag{47}$$

where:

$$U_n = \frac{1}{\sqrt{N_n}} \int_0^{\ell} (\mu\, \xi_n^*\, \epsilon + (j_T - j_p)\, \alpha_n^*\, \psi)\, dz \tag{48}$$

U_n is the modal unbalance component.

In the summation in Equation (47), the eigenvalues are considered as separate roots. Thus, when s_n is a complex eigenvalue, the conjugate value $\bar{s}_n$ is also an eigenvalue, and its contribution must be added separately. Substituting Equation (37) into Equations (47) and (48), the contribution becomes:

$$\left[\frac{\Omega^2}{2 s_n\, (i\Omega - s_n)} \frac{\xi_n}{\sqrt{N_n}} U_n \right]_{s_n = \bar{s}_n} = \frac{\Omega^2}{2 \bar{s}_n\, (i\Omega - \bar{s}_n)} \frac{\bar{\eta}_n}{\sqrt{\bar{N}_n}} U'_n \tag{49}$$

where:

$$U_n' = \frac{1}{\sqrt{\tilde{N}_n}} \int_0^{\ell} (\mu\, \bar{\eta}_n^*\, \epsilon + (j_T - j_p)\, \bar{\beta}_n^*\, \psi)\, dz \tag{50}$$

Hence, U_n' is only equal to $\tilde{U}_n$ (the conjugate value of U_n) when ϵ and ψ are real (planar unbalance distribution).

Modal Balancing Correction Weights

To balance the rotor, correction weights w_p (with units of mass and length) are inserted in a number of balancing planes. The resulting response is determined from Equations (47) and (48) as:

$$\xi = \sum_n \frac{\Omega^2}{2s_n\,(i\Omega - s_n)} \frac{\xi_n}{\sqrt{N_n}} \left[U_n + \frac{1}{\sqrt{N_n}} \int_0^{\ell} \delta(z-z_p)\, \xi_n^*\, w_p\, dz \right] \tag{51}$$

where $\delta(z-z_p)$ is the unit delta function. Thus, the contribution from the n'th mode can be eliminated by a set of correction weights, w_p, chosen such that:

$$U_n + \frac{1}{\sqrt{N_n}} \int_0^{\ell} \delta(z-z_p)\, \xi_n^*\, w_p\, dz = 0 \tag{52}$$

or:

$$\sum_p \frac{\xi_n^*(z_p)}{\sqrt{N_n}}\, w_p = -U_n \tag{53}$$

This corresponds to n equations with p unknowns and, therefore, there must be at least as many balancing planes as the number of modes for which correction is required.

Assuming that p equals n, Equation (53) may be solved directly to determine the correction weights w_p. In that case, an optimization of the locations, z_p, of the balancing planes could possibly be performed to find those coordinates for which the total sum of the correction weights would be a minimum. The answer, however, would depend on the assumed unbalance distribution (U_n), and as this must be considered unknown, an alternative approach is necessary.

For this purpose, instead of one set of correction weights, each mode is assigned its own set of correction weights: w_{pn}, and Equation (53) is written in matrix form as:

$$\begin{Bmatrix} \frac{\xi_1^*(z_1)}{\sqrt{N_1}} & \cdots & \frac{\xi_1^*(z_p)}{\sqrt{N_1}} \\ \vdots & & \vdots \\ \frac{\xi_n^*(z_1)}{\sqrt{N_n}} & \cdots & \frac{\xi_n^*(z_p)}{\sqrt{N_n}} \end{Bmatrix} \begin{Bmatrix} \frac{w_{11}}{U_1} & \cdots & \frac{w_{1n}}{U_n} \\ \vdots & & \vdots \\ \frac{w_{p1}}{U_1} & \cdots & \frac{w_{pn}}{U_n} \end{Bmatrix} = - \begin{Bmatrix} 1 & \cdots & 0 \\ \vdots & \ddots & \vdots \\ 0 & \cdots & 1 \end{Bmatrix} \tag{54}$$

where the matrix on the right-hand side is the unit matrix.

In this formulation, any set of modal correction weights will only contribute to the assigned mode. They are independent of how the rotor unbalance is distributed, but their value is directly proportional to the magnitude and phase of the modal component, U_n, of the unknown existing unbalance. Thus, an absolute optimization, as discussed in connection with Equation (53), is not possible and, instead, each mode is considered separately by computing the normalized sum of the modal correction weights:

$$S_n = \left| \frac{\xi_n^*(z_p)}{\sqrt{N_n}} \right|_{max} \cdot \sum_p \left| \frac{w_{pn}}{U_n} \right| \tag{55}$$

The minimum value of S_n is equal to 1. Thereby, the effectiveness of any correction plane combination can be tested directly, and that combination which results in the lowest sum for all modes, is the optimum combination.

From Equation (47) it is seen that the modal amplitude contribution is proportional to:

$$\frac{\Omega^2}{2s_n(i\Omega - s_n)} = \frac{\Omega^2\left(-\lambda_n + i(\omega_n - \Omega)\right)}{2s_n\left[(\omega_n - \Omega)^2 + \lambda_n^2\right]} \tag{56}$$

Disregarding s_n in the denominator which does not change with speed, the phase angle equals $\tan^{-1}\left(\frac{\omega_n - \Omega}{-\lambda_n}\right)$. Hence, the phase angle decreases with speed. It is 90 degrees less than the value at zero speed when:

$$\Omega = \omega_n \left[1 + \left(\frac{\lambda_n}{\omega_n}\right)^2\right] = \omega_n \left[1 + \left(\frac{\delta_n}{2\pi}\right)^2\right] \tag{57}$$

where:

$$\text{logarithmic decrement:} \quad \delta_n = -\frac{2\pi\,\lambda_n}{\omega_n} \tag{58}$$

This speed should be considered the "resonant speed", and upon substitution into Equation (56), the magnification factor becomes:

$$Q = \frac{\pi}{\delta}\left[1 + \left(\frac{\delta}{2\pi}\right)^2\right] \tag{59}$$

In practice, the magnification becomes insignificant when δ exceeds 1.5 to 2, and modes which are that well damped will make no significant contribution to the response. Hence, in selecting the balance plane locations from optimizing the sum of the modal correction weights, most importance should be assigned to the least damped modes.

For a general rotor-bearing system, the supports are usually anisotropic such that the horizontal stiffness, say, is smaller than the vertical stiffness. Thus, there will be two modes per "critical" speeds but the mode shapes will be quite similar. For this reason, only one of the modes may be used when computing the modal correction weights from Equation (54) to avoid redundancy and a numerically ill-behaved matrix. Basically, the modal correction weights form vectors which are orthogonal to the adjoint modal functions such that the latter functions in themselves must be chosen to yield a vector space of the same dimension as the number of planes.

For the same reason, all critical speeds must be represented, even though one or two of them may be over-damped. Only after computing the modal correction

weights may it be decided to assign less importance to certain well-damped modes.

Locating Measurement Probes

The amplitude response is given by Equation (42) from which it is immediately obvious that the maximum amplitudes at any "critical speed" occur where the corresponding modal functions ("mode shape") have their maxima. Thus, a displacement sensor located at one of these maxima will be most sensitive to the rotor's response to unbalance at this critical speed. As a means of quantifying the "composite" sensitivity of a number of displacement sensors located at a number of rotor locations, the following "sensitivity function" could be used.

$$P_n = \sum_m \left| \frac{\xi_n(Z_m)}{\sqrt{N_n}} \right|$$

where the summation is over all the probe locations Z_m, and such a function is evaluated for each of the modes to be balanced. This function does not have a rigorous basis, but offers a reasonable approach to expressing the likely effectiveness of a particular selection of sensor locations.

Consideration of Anisotropic Supports

A general rotor-bearing system with anisotropic supports will have elliptical unbalance response whirl orbits such that the amplitude in the x-direction will differ from the y-amplitude. Thus, to make use of both measurements, they should be combined into the forward precessional component, ξ, as given by Equation (15). The procedure is as follows: assume that x and y are measured as discussed in connection with Equations (1) to (3):

$$\begin{aligned} x &= x_c + ix_s \sim x_c \cdot \cos(\Omega t) - x_s \cdot \sin(\Omega t) = |x| \cdot \cos(\Omega t + \varphi_x) \\ y &= y_c + iy_c \sim y_c \cdot \cos(\Omega t) - y_s \cdot \sin(\Omega t) = |y| \cdot \cos(\Omega t + \varphi_y) \end{aligned} \qquad (60)$$

where:

$$\begin{aligned} |x| &= \sqrt{x_c^2 + x_s^2} \quad , \text{ the x-amplitude} \\ |y| &= \sqrt{y_c^2 + y_s^2} \quad , \text{ the y-amplitude} \end{aligned} \qquad (61)$$

$$\varphi_x = \tan^{-1}\left(\frac{x_s}{x_c}\right) \quad , \text{ the x-phase angle}$$

$$\varphi_y = \tan^{-1}\left(\frac{y_s}{y_c}\right) \quad , \text{ the y-phase angle} \tag{62}$$

$$x_c = |x| \cdot \cos \varphi_x \qquad x_s = |x| \cdot \sin \varphi_x \tag{63}$$

$$y_c = |y| \cdot \cos \varphi_y \qquad y_s = |y| \cdot \sin \varphi_y \tag{64}$$

From Equation (15):

$$\xi = \frac{1}{2}(x + iy) = \frac{1}{2}(x_c - y_s + i(x_s + y_c)) = |\xi| \cdot \cos(\Omega t + \varphi_\xi) \tag{65}$$

Hence, the amplitude, $|\xi|$, and the phase angle, φ_ξ, of the forward precessional component can be computed from:

$$|\xi| = \frac{1}{2}\sqrt{(x_c - y_s)^2 + (x_s + y_c)^2} \tag{66}$$

$$\varphi_\xi = \tan^{-1}\left(\frac{x_s + y_c}{x_c - y_s}\right) \tag{67}$$

Instead of computing it, the forward precessional component may also be obtained electronically by shifting the phase angle of the y-signal 90 degrees forward (R-C-circuit), adding it to the x-signal and dividing by 2.

The advantage of using the forward precessional component is that it basically represents a circular whirl orbit with the same whirl direction as the shaft rotation. Thus, its amplitude is independent of the angular position of the measurement probes.

APPENDIX B

STABILITY OF A SHAFT WITH FLEXURAL ASYMMETRY

In this appendix the equations of motion for free vibration of a flexibly supported rotor with flexural asymmetry are developed, and a method of solution is described which yields the complex eigenvalues and hence the state of stability of the rotor. The development is an extension of Lund's work (4) for symmetrical rotors.

Analysis

The rotor is described analytically as a series of stations, at which concentrated mass, and transverse and polar moments of inertia may be located. At any station a bearing, represented by radial stiffness and damping coefficients, may also be located. The rotor stations are considered to be connected by massless elastic beams (fields) capable of deformation in both bending and shear. Each field can have principal section moduli which differ from each other, with the stipulation that all fields have common principal axes (ξ and η), which form a rotating coordinate frame.

In the development which follows, the transfer equations for a typical station (transfer matrix) are written, first in fixed coordinates, then in rotating coordinates. The field transfer equations are written directly in rotating coordinates. A general expression for the motion of the rotor is written in the form:

$$\xi = \mathrm{Re}\ \{\xi^* e^{St}\} \qquad \text{B-1}$$

where $S = \lambda + i\,\omega'$ and $\omega' = \omega - \Omega$ B-2

and a similar equation may be written for the η direction.

Here ξ,S are complex and all phase information is contained in ξ^*. The development is actually performed for the more general case of

$$\xi = \xi^* e^{St} \qquad \text{B-3}$$

So we can write

$$\frac{d}{dt} = S \qquad \text{B-4}$$

$$\frac{d^2}{dt^2} = S^2 \qquad \text{B-5}$$

The equations are solved to yield those values of S at which the complex system determinent is zero - the only conditions under which a free vibration can take place. The rotor is stable if λ, the real part of S, is negative, and unstable if λ is positive.

Station Equations of Motion

Figure 45 illustrates the sign convention for shear force, bending moment, and translational and angular displacements in the x-z plane. θ is the rotation angle from z to x. In the y-z plane, a similar diagram would show ϕ as being the rotation angle from z to y.

If we consider that, in addition to inertia forces, any station may be acted upon by bearing forces, the forces acting at station n are related by:

$$\begin{Bmatrix} -V'_{xn} \\ -V'_{yn} \\ M'_{xn} \\ M'_{yn} \end{Bmatrix} = \begin{Bmatrix} -V_{xn} \\ -V_{yn} \\ M_{xn} \\ M_{yn} \end{Bmatrix} + \begin{Bmatrix} M_n \frac{d^2x_n}{dt^2} \\ M_n \frac{d^2y_n}{dt^2} \\ J_{tn} \frac{d^2\theta_n}{dt^2} + \Omega J_{pn} \frac{d\phi_n}{dt} \\ J_{tn} \frac{d^2\phi_n}{dt^2} - \Omega J_{pn} \frac{d\theta_n}{dt} \end{Bmatrix} + \underline{\underline{K}} \begin{Bmatrix} x_n \\ y_n \\ \theta_n \\ \phi_n \end{Bmatrix} + \underline{\underline{B}} \begin{Bmatrix} \frac{dx_n}{dt} \\ \frac{dy_n}{dt} \\ \frac{d\theta_n}{dt} \\ \frac{d\phi_n}{dt} \end{Bmatrix} \quad \text{B-6}$$

where $\underline{\underline{K}}$, $\underline{\underline{B}}$ are 4 x 4 isotropic bearing stiffness and damping matrices, with no coupling between translational and angular degrees of freedom.

Figure 46 defines the coordinate directions (ξ, η, z) to be employed in a rotating frame, and their relation to the fixed (x, y, z) frame. In addition the relationships between angles (θ, ϕ) in the fixed frame and (α, β) in the rotating frame are illustrated.

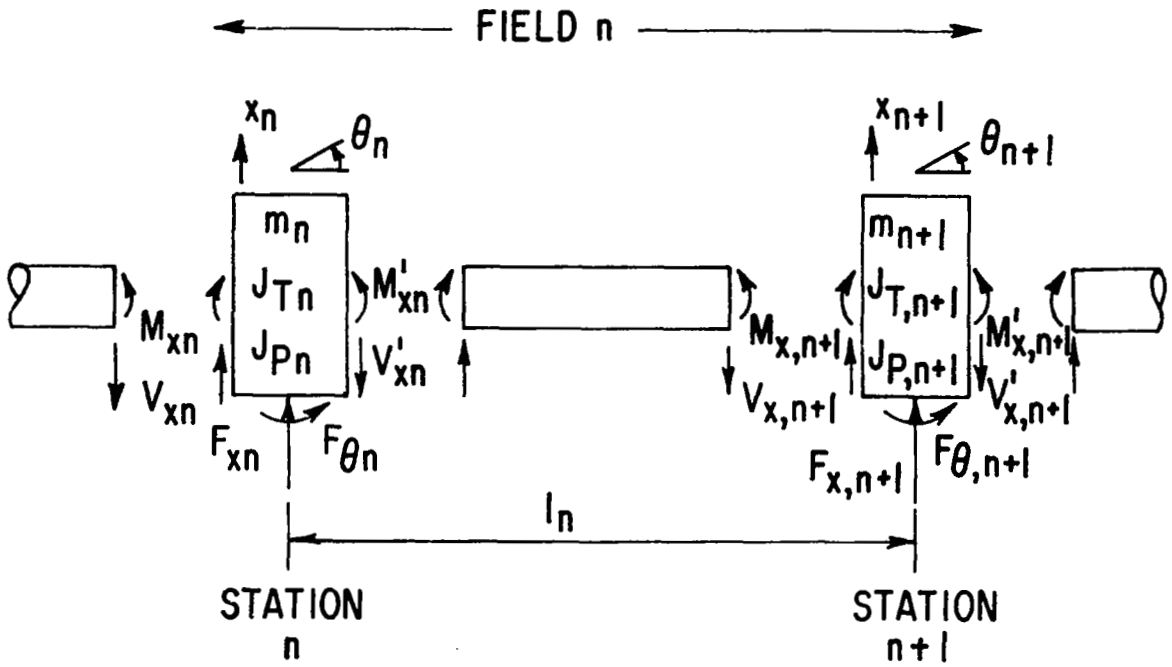

Fig. 45 Sign Convention for Radial Displacement, Angular Displacement, Bending Moment, and Shear Force

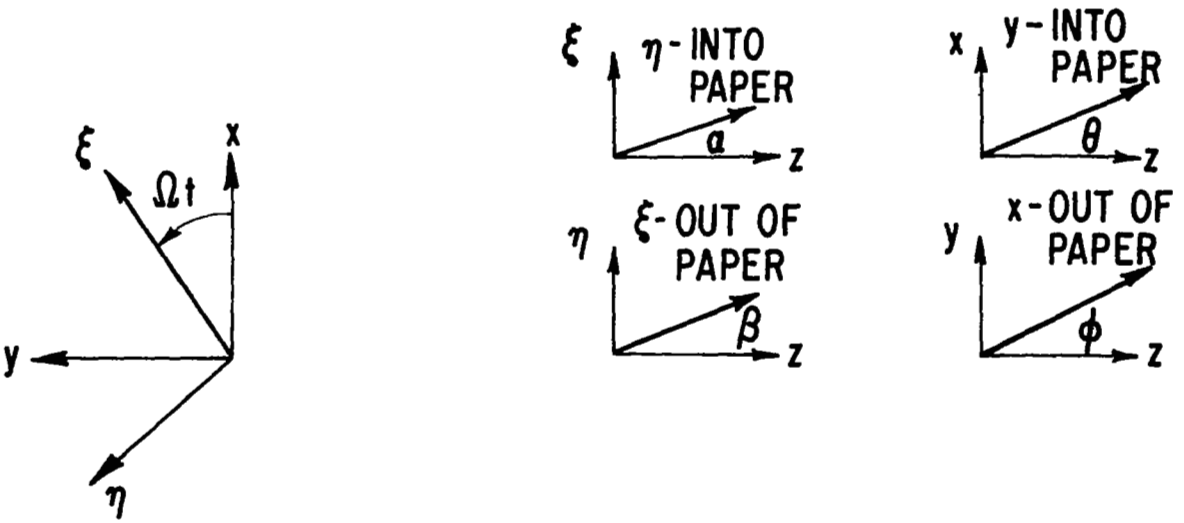

Fig. 46 Relationship Between Fixed and Rotating Coordinate Frames

To translate from the (x, y, z) system to the (ξ, η, z) system we must substitute into the station equations:

$$x = \xi \cos \Omega t - \eta \sin \Omega t$$

$$y = \xi \sin \Omega t + \eta \cos \Omega t$$

$$\theta = \alpha \cos \Omega t - \beta \sin \Omega t$$

$$\phi = \alpha \sin \Omega t + \beta \cos \Omega t$$

B-7

and the result is:

$$\begin{Bmatrix} -V'_{\xi n} \\ -V'_{\eta n} \\ M'_{\xi n} \\ M'_{\eta n} \end{Bmatrix} = \begin{Bmatrix} -V_{\xi n} \\ -V_{\eta n} \\ M_{\xi n} \\ M_{\eta n} \end{Bmatrix} + \begin{Bmatrix} M_n \dfrac{d^2\xi_n}{dt^2} \\ M_n \dfrac{d^2\eta_n}{dt^2} \\ J_{tn} \dfrac{d^2\alpha_n}{dt^2} + \Omega J_{pn} \dfrac{d\beta_n}{dt} \\ J_{tn} \dfrac{d^2\beta_n}{dt^2} - \Omega J_{pn} \dfrac{d\alpha_n}{dt} \end{Bmatrix} + \begin{Bmatrix} M_n(-\Omega^2 \xi_n - 2\Omega \dfrac{d\eta_n}{dt}) \\ M_n(\dfrac{2\Omega d\xi_n}{dt} - \Omega^2 \eta_n) \\ J_{tn}(-\Omega^2 \alpha_n - 2\Omega \dfrac{d\beta_n}{dt}) + \Omega^2 J_{pn} \alpha_n \\ J_{tn}(-\Omega^2 \beta_n + 2\Omega \dfrac{d\alpha_n}{dt}) + \Omega^2 J_{pn} \beta_n \end{Bmatrix}$$

$$+\underline{\underline{K}} \begin{Bmatrix} \xi_n \\ \eta_n \\ \alpha_n \\ \beta_n \end{Bmatrix} + \underline{\underline{B}} \begin{Bmatrix} \dfrac{d\xi_n}{dt} \\ \dfrac{d\eta_n}{dt} \\ \dfrac{d\alpha_n}{dt} \\ \dfrac{d\beta_n}{dt} \end{Bmatrix} + \Omega \underline{\underline{B}}'' \begin{Bmatrix} \xi_n \\ \eta_n \\ \alpha_n \\ \beta_n \end{Bmatrix}$$

B-8

where $\underline{\underline{B}}'' =$

$$\begin{bmatrix} B_{xy} & -B_{xx} & 0 & 0 \\ B_{xx} & B_{xy} & 0 & 0 \\ 0 & 0 & D_{xy} & -D_{xx} \\ 0 & 0 & D_{xx} & D_{xy} \end{bmatrix} \qquad \text{B-9}$$

and B_{xx}, B_{xy} are direct and cross-coupling translational damping coefficients, D_{xx}, D_{xy} are the direct and cross-coupling angular damping coefficients in the bearing.

Finally, substituting

$$S = \frac{d}{dt}; \qquad S^2 = \frac{d^2}{dt^2} \qquad \text{B-10}$$

we get:

$$\begin{Bmatrix} -V'_{\xi n} \\ -V'_{\eta n} \\ M'_{\xi n} \\ M'_{\eta n} \end{Bmatrix} = \begin{Bmatrix} -V_{\xi n} \\ -V_{\eta n} \\ M_{\xi n} \\ M_{\eta n} \end{Bmatrix} + \begin{Bmatrix} M_n S^2 \xi_n \\ M_n S^2 \eta_n \\ J_{tn} S^2 \alpha_n + \Omega J_{pn} S\beta_n \\ J_{tn} S^2 \beta_n - \Omega J_{pn} S\alpha_n \end{Bmatrix} + \begin{Bmatrix} M_n(-\Omega^2 \xi_n - 2\Omega S\eta_n) \\ M_n(2\Omega S\xi_n - \Omega^2 \eta_n) \\ J_{tn}(-\Omega^2 \alpha_n - 2\Omega S\beta_n) + \Omega^2 J_{pn}\alpha_n \\ J_{tn}(-\Omega^2 \beta_n + 2\Omega S\alpha_n) + \Omega^2 J_{pn}\beta_n \end{Bmatrix} + (\underline{\underline{K}} + S\underline{\underline{B}} + \Omega\underline{\underline{B}}'') \begin{Bmatrix} \xi_n \\ \eta_n \\ \alpha_n \\ \beta_n \end{Bmatrix} \qquad \text{B-11}$$

Field Equations

The elastic beams between stations are considered to have principal axes aligned with the ξ-η coordinates as shown in Figure 47.

Let $(I_\xi)_n$ be the second moment of area of the shaft between stations n and n+1, about an axis parallel to the ξ-axis. $(I_\eta)_n$ is the corresponding second moment of area about an axis parallel to the y-axis. The relationships between displacements, forces and moments at the ends of the shaft section between stations n and n+1 are:

$$\xi_{n+1} = \xi_n + \ell_n \alpha_n + \frac{1}{(EI_\eta)_n}\left[\frac{\ell_n^2}{2} M'_{\xi n} + \left(\frac{\ell_n^3}{6} - \frac{(\ell E\, I_\eta)_n}{(\alpha GA)_n}\right) V'_{\xi n}\right] \quad \text{B-12}$$

$$\eta_{n+1} = \eta_n + \ell_n \beta_n + \frac{1}{(EI_\xi)_n}\left[\frac{\ell_n^2}{2} M'_{\eta n} + \left(\frac{\ell_n^3}{6} - \frac{(\ell E\, I_\xi)_n}{(\alpha GA)_n}\right) V'_{\eta n}\right] \quad \text{B-13}$$

$$\alpha_{n+1} = \alpha_n + \frac{1}{(E\, I_\xi)_n}\left[\ell_n M'_{\xi n} + \frac{\ell_n^2}{2} V'_{\xi n}\right] \quad \text{B-14}$$

$$\beta_{n+1} = \beta_n + \frac{1}{(E\, I_\eta)_n}\left[\ell_n M'_{\eta n} + \frac{\ell_n^2}{2} V'_{\eta n}\right] \quad \text{B-15}$$

$$M_{\xi,n+1} = M'_{\xi n} + \ell_n V'_{\xi n} \quad \text{B-16}$$

$$M_{\eta,n+1} = M'_{\eta n} + \ell_n V'_{\eta n} \quad \text{B-17}$$

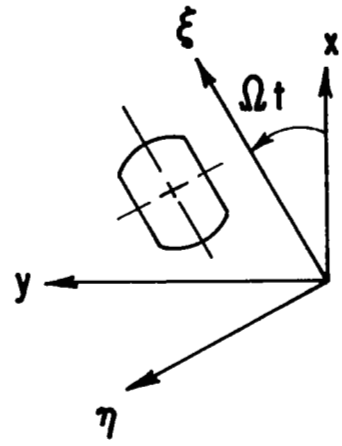

Fig. 47 Alignment of Principal Axes with Rotating Coordinates

$$V_{\xi,n+1} = V'_{\xi n} \qquad \text{B-18}$$

$$V_{\eta,n+1} = V'_{\eta n} \qquad \text{B-19}$$

Now, to implement the solution algorithm, a total of four calculations is performed, for an assumed value of S. Each of ξ_1, η_1, α_1, β_1 is, in turn, set to 1 while the others are maintained as zero. In addition, at the left-hand end (end 1) the free boundary conditions are imposed:

$$M_{\xi 1} = M_{\eta 1} = V_{\xi 1} = V_{\eta 1} = 0 \qquad \text{B-20}$$

The result of this calculation for the rotor may be expressed in matrix terms:

$$\begin{Bmatrix} M'_{\xi N} \\ M'_{\eta N} \\ V'_{\xi N} \\ V'_{\eta n} \end{Bmatrix} = \underline{\underline{T}} \begin{Bmatrix} \xi_1 \\ \eta_1 \\ \alpha_1 \\ \beta_1 \end{Bmatrix} \qquad \text{B-21}$$

where $\underline{\underline{T}}$ is a square matrix, and N is the number of stations. To satisfy the free boundary condition at the right-hand end (station N) requires that Δ, the determinant of $\underline{\underline{T}}$ be zero, and the values of S which satisfy this condition are the complex eigenvalues from which the stability of the system can be determined.

An iterative solution, based on the generalized Newton Raphson method, is used to find these values of S. To implement this solution method, the determinant Δp of the matrix $\underline{\underline{T}}_p$ is required, in which the elements of the p^{th} column of $\underline{\underline{T}}$ have been replaced by their derivatives with respect to S. These derivatives are determined in a parallel operation to the determination of the element values. The starting values for all derivatives are zero:

$$\frac{d_{\xi 1}}{dS} = \frac{d_{\eta 1}}{dS} = \frac{d_{\alpha 1}}{dS} = \frac{a_{\beta 1}}{dS} = \frac{dM_{\xi 1}}{dS} = \frac{dM_{\eta 1}}{dS} = \frac{dV_{\xi 1}}{dS} = \frac{dV_{\eta 1}}{dS} = 0 \qquad \text{B-22}$$

The field transfer relationships for the derivatives are exactly the same as the relationships for the corresponding values (since they do not contain S). The station transfer relationships for the derivatives are different, however, as follows:

$$
\begin{Bmatrix} -\frac{dV'_{\xi n}}{dS} \\ -\frac{dV'_{\eta n}}{dS} \\ \frac{dM'_{\xi n}}{dS} \\ \frac{dM'_{\eta n}}{dS} \end{Bmatrix} = \begin{Bmatrix} -\frac{dV_{\xi n}}{dS} \\ -\frac{dV_{\eta n}}{dS} \\ \frac{dM_{\xi n}}{dS} \\ \frac{dM_{\eta n}}{dS} \end{Bmatrix} + \begin{Bmatrix} S^2 M_n \frac{d\xi_n}{dS} - \Omega^2 M_n \frac{d\xi_n}{dS} - 2S\,\Omega M_n \frac{d\eta_n}{dS} \\ S^2 M_n \frac{d\eta_n}{dS} - \Omega^2 M_n \frac{d\eta_n}{dS} + 2S\,\Omega M_n \frac{d\xi_n}{dS} \\ S^2 J_{tn} \frac{d\alpha_n}{dS} - \Omega^2 J_{tn} \frac{d\alpha_n}{dS} - 2S\,\Omega J_{tn} \frac{d\beta_n}{dS} + S\Omega J_{pn} \frac{d\beta_n}{dS} + \Omega^2 J_{pn} \frac{d\alpha_n}{dS} \\ S^2 J_{tn} \frac{d\beta_n}{dS} - \Omega^2 J_{tn} \frac{d\beta_n}{dS} + 2S\Omega J_{tn} \frac{d\alpha_n}{dS} - S\Omega J_{pn} \frac{d\alpha_n}{dS} + \Omega^2 J_{pn} \frac{d\beta_n}{dS} \end{Bmatrix}
$$

$$
+ (\underline{\underline{K}} + S\underline{\underline{B}} + \Omega\underline{\underline{B}}'') \begin{Bmatrix} \frac{d\xi_n}{dS} \\ \frac{d\eta_n}{dS} \\ \frac{d\alpha_n}{dS} \\ \frac{d\beta_n}{dS} \end{Bmatrix} + \underline{\underline{B}} \begin{Bmatrix} \xi_n \\ \eta_n \\ \alpha_n \\ \beta_n \end{Bmatrix}
$$

$$
+ \begin{Bmatrix} 2SM_n \beta_n \\ 2SM_n \eta_n \\ 2SJ_{tn} \alpha_n + \Omega J_{pn} \beta_n \\ 2SJ_{tn} \beta_n - \Omega J_{pn} \alpha_n \end{Bmatrix} + \begin{Bmatrix} -2\Omega M_n \eta_n \\ +2\Omega M_n \beta_n \\ -2\Omega \beta_n J_{tn} \\ +2\Omega \alpha_n J_{tn} \end{Bmatrix}
$$

B-23

As shown by Reference [4], an iteration, which avoids convergence to roots already found is given by

$$S = S_o - \Delta_o / [(\frac{d\Delta}{dS})_o - \Delta_o \sum_{j=1}^{J} (1/(S_o - S_j))] \qquad \text{B-24}$$

where Δ_o, S_o are the current values of Δ and S in the iteration, J roots, S_j, have already been found, and $(\frac{d\Delta}{dS})_o$ is the derivative of Δ with respect to S as determined by summing:

$$\frac{d\Delta}{dS} = \sum_{p=1}^{4} \Delta p \qquad \text{B-25}$$

Check of Analytical Method

The asymmetric rotor model of Bones and Hannam [10] was used to check the analysis for a single mass supported on a massless, flexible shaft with external damping applied to the central mass. As shown in Figure 48, an exact check of the required damping value for the stability threshold was obtained.

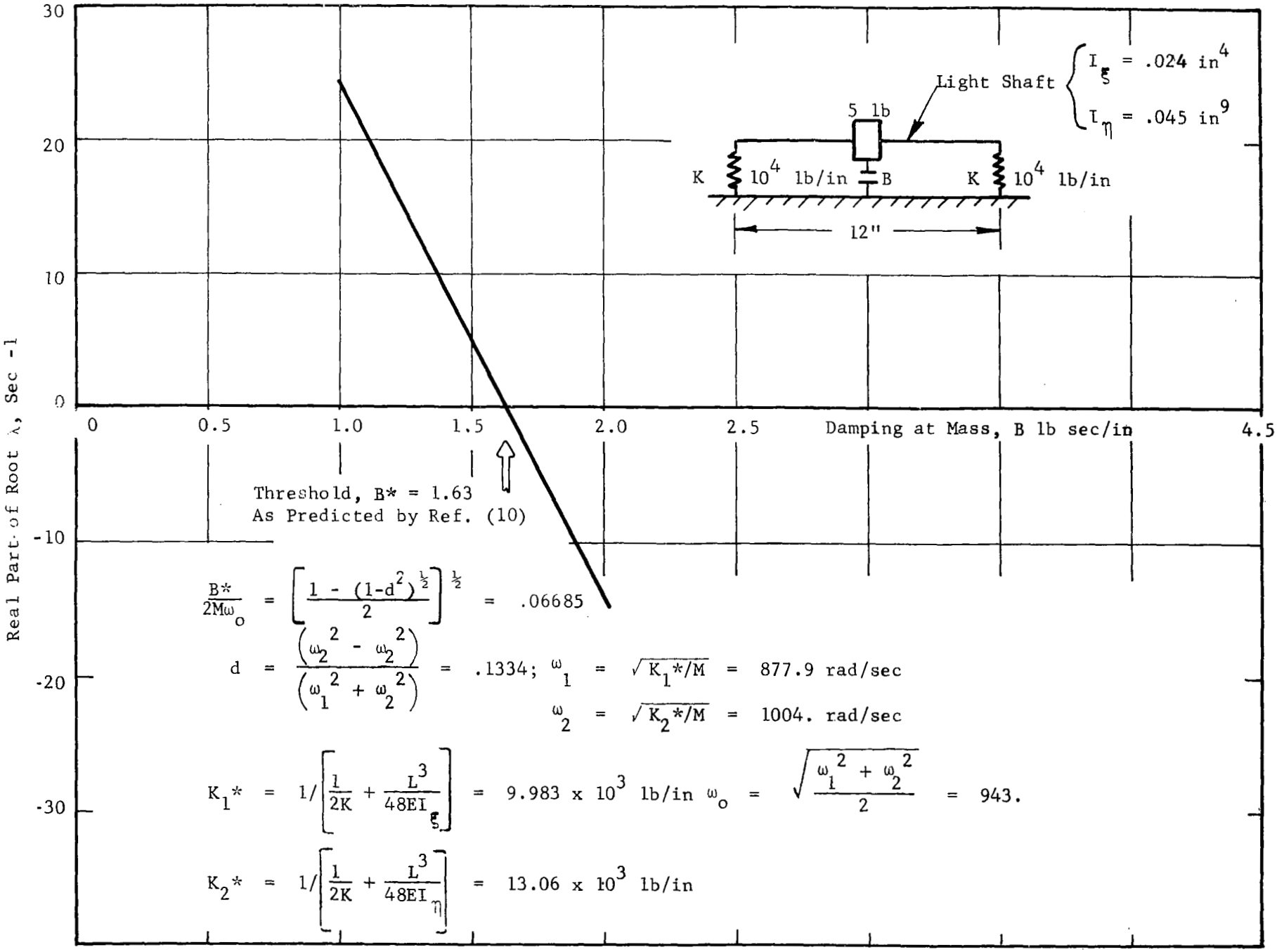

Fig. 48 Check of Stability Analysis for Asymmetric Shaft. Comparison with Bones and Hannam (Ref. 10)

APPENDIX C

MTI COMMAND™ MULTIPLANE, MULTISPEED BALANCING SYSTEM

The MTI multiplane, multispeed balancing system in its current form, as it was used for the balancing experiments described in this report, is a further development of the non-computerized data acquisition system previously described in Refs. 2 & 3. In this system electronic analog signal processing equipment has been combined with a self-contained data processing center to provide for automatic data acquisition, signal conditioning, and correction weight calculations. The role of the equipment operator during balancing operations has been reduced to speed control of the rotor to be balanced and trial and correction weight addition and removal as called for by the computer print-out. The minicomputer in the system can be programmed via punched paper tape, before each balancing operation, for the number of trial weight locations to be used on the rotor to be balanced, the number of sensors to be used, and the balancing speed at which balancing data is to be acquired. Once the number of balancing parameters has been decided upon and the balancing speed variation tolerances set at which balancing data may be acquired, the computer will automatically request the proper amount of data to satisfy the balancing requirements. The computer automatically examines the data from multiple data readings for consistency and rejects all data that is found to be outside acceptable distribution limits. Data originating outside the pre-set rotor speed window is rejected. The computer informs the machine operator of each successive step to be taken in rotor speed control and provides the operator with a number of options in procedure; for example, he can choose to impose an additional trim balance correction weight set after completion of the regular balancing operation, and he can control the extent of the printed record on the balancing operation for quality control or other record keeping purposes.

The data acquisition subsystem has to accomplish the following functions typical of any advanced balancing machine:

1. Filtering of the electronic amplitude signals which are proportionate to rotor unbalance.

2. Measurement of the filtered amplitude signal.

3. Phase angle determination between each filtered amplitude signal used for balancing and a fixed point on the rotor.

4. Automatic sequential switching among amplitude signals used for balancing.

The requirements of an automatic system add two more functions to the acquisition subsystem:

1. Controlling of the sequence and duration of measurement, and interfacing between analysis components and between the analog and digital systems.

2. A/D conversion of the analog signal for computer processing.

The data processing subsystem has three components:

1. Central processor
2. Magnetic memory
3. Keyboard terminal

The selection of system components, which generally by themselves are the most advanced systems of their kind, was based upon previous flexible rotor balancing experience. The capabilities incorporated into the system will generally meet the most advanced requirements in flexible rotor balancing. A summary of system capabilities is given below:

- Input channels: 20 analog signals
- Input signal voltage: 1.0 MV to 10 VRMS
- Input signal frequency: 2 Hz to 2 kHz
- Balancing planes: 20 *
- Balancing speeds: 5 *

*The last two parameters can be expanded with additional computer memory, if required.

The multiplane, multispeed balancing system processes electronic vibration signals in the specified voltage and frequency range, without regard to type of source. Inductive, capacitive, or optical displacement sensors, velocity sensors, accelerometers, strain gages, or other sensors providing signals proportional to rotor synchronous lateral vibration may be used. Sensor leads with BNC-type connections may be directly connected.

A photo of the complete MTI multiplane, multispeed balancing system is shown in Figure 49.

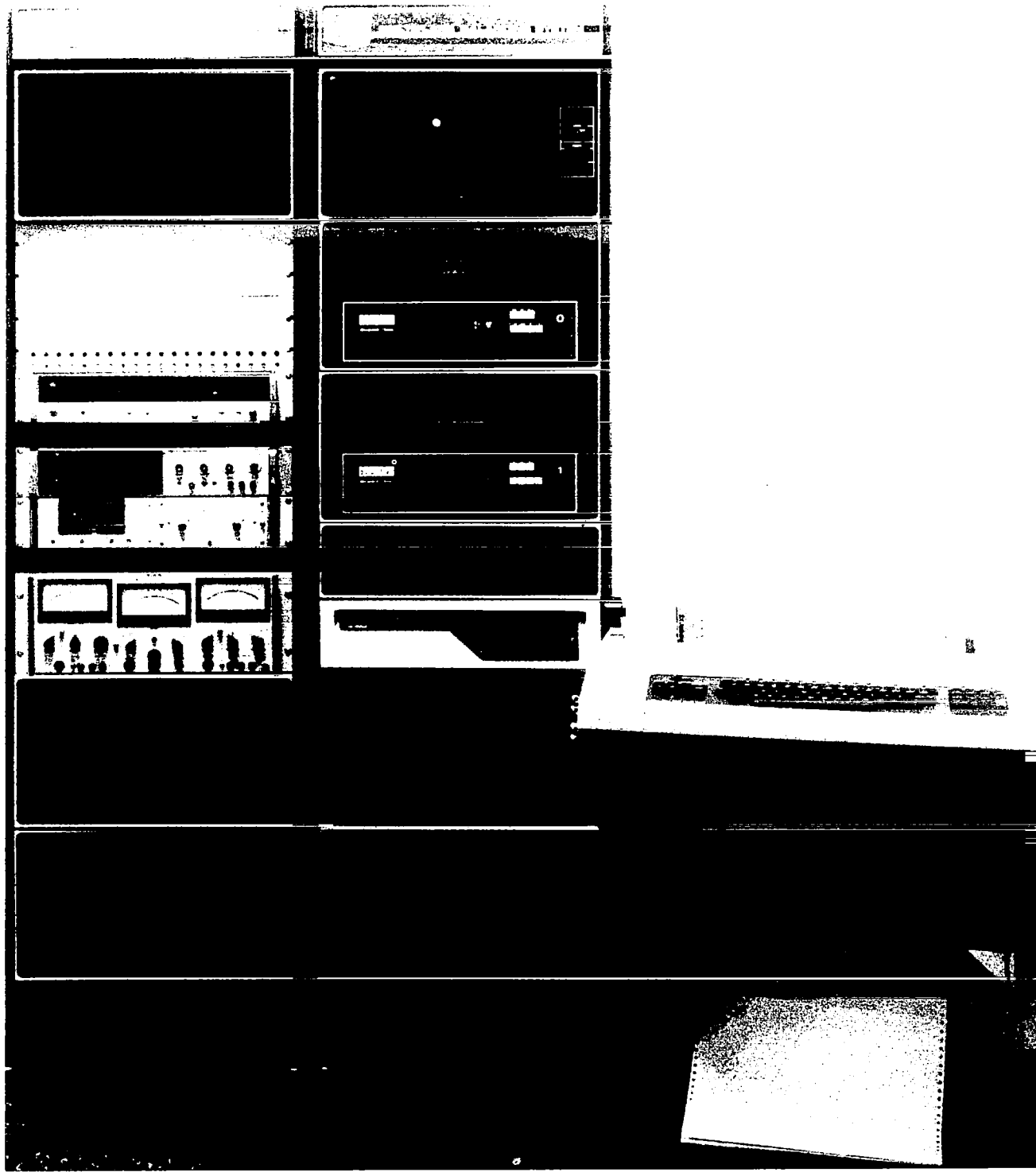

Fig. 49 MTI COMMAND™ Model 2005 Balancing System

1. Report No.	2. Government Accession No.	3. Recipient's Catalog No.
NASA CR-2975		

4. Title and Subtitle	5. Report Date
BALANCING TECHNIQUES FOR HIGH-SPEED FLEXIBLE ROTORS	April 1978
	6. Performing Organization Code
7. Author(s)	8. Performing Organization Report No.
A. J. Smalley, J. M. Tessarzik, and R. A. Rio	MTI 77TR2
	10. Work Unit No.
9. Performing Organization Name and Address	
Mechanical Technology Incorporated 968 Albany-Shaker Road Latham, New York 12110	11. Contract or Grant No. NAS3-18520
	13. Type of Report and Period Covered
12. Sponsoring Agency Name and Address	Contractor Report
National Aeronautics and Space Administration Washington, D.C. 20546	14. Sponsoring Agency Code

15. Supplementary Notes

Final report. Project Manager, David P. Fleming, Fluid System Components Division, NASA Lewis Research Center, Cleveland, Ohio 44135.

16. Abstract

In this report, the topics of ideal and non-ideal conditions for multiplane balancing are addressed. Methodology and procedures for identifying optimum balancing configurations and for assessing, quantitatively, the penalties associated with non-optimum configurations are developed and demonstrated. The problems introduced when vibration sensors are supported on flexible mounts are assessed experimentally, and the effects of flexural asymmetry in the rotor on balancing are investigated. A general-purpose method for predicting the threshold of instability of an asymmetric rotor is developed, and its predictions are compared with measurements under different degrees of asymmetry.

17. Key Words (Suggested by Author(s))	18. Distribution Statement
Multiplane balancing of rotor with flexural asymmetry Predicting instability threshold of asymmetric rotor	Unclassified - unlimited STAR Category 37

19. Security Classif. (of this report)	20. Security Classif. (of this page)	21. No. of Pages	22. Price*
Unclassified	Unclassified	128	A07

* For sale by the National Technical Information Service, Springfield, Virginia 22161

NASA-Langley, 1978